

FACULTY
OF MATHEMATICS
AND PHYSICS
Charles University

1

BACHELOR THESIS

2

Martin Vavřík

3

**Simulation and Reconstruction
of Charged Particle Trajectories
in an Atypic Time Projection Chamber**

4

5

Institute of Particle and Nuclear Physics

6

Supervisor of the bachelor thesis: Mgr. Tomáš Sýkora, Ph.D.

7

Study programme: Physics

8

Prague 2025

- ⁹ I declare that I carried out this bachelor thesis independently, and only with the
¹⁰ cited sources, literature and other professional sources. It has not been used to
¹¹ obtain another or the same degree.
- ¹² I understand that my work relates to the rights and obligations under the Act
¹³ No. 121/2000 Sb., the Copyright Act, as amended, in particular the fact that the
¹⁴ Charles University has the right to conclude a license agreement on the use of this
¹⁵ work as a school work pursuant to Section 60 subsection 1 of the Copyright Act.

In date
Author's signature

¹⁶ Dedication.

Title: Simulation and Reconstruction of Charged Particle Trajectories in an Atypical Time Projection Chamber **Added hyphen to avoid overfull hbox**

Author: Martin Vavřík

Institute: Institute of Particle and Nuclear Physics

Supervisor: Mgr. Tomáš Sýkora, Ph.D., Institute of Particle and Nuclear Physics

Abstract: Abstract.

Keywords: key words

¹⁷ Contents

¹⁸	Motivation	3
¹⁹	0.1 ATOMKI Anomaly	3
²⁰	0.1.1 ATOMKI Measurements	3
²¹	0.1.2 Other Experiments	4
²²	0.2 X17 Project at IEAP CTU	7
²³	1 Time Projection Chamber	9
²⁴	1.1 Charge transport in gases	9
²⁵	1.1.1 Drift	10
²⁶	1.1.2 Diffusion	11
²⁷	1.2 Examples of TPCs	12
²⁸	1.2.1 The original TPC at PEP-4 at SLAC	12
²⁹	1.2.2 ALICE TPC	12
³⁰	1.2.3 CERES/NA45 radial-drift TPC	13
³¹	1.2.4 Other interesting radial-drift TPCs	15
³²	1.3 Readout	16
³³	1.3.1 Multi-Wire Proportional Chamber	16
³⁴	1.3.2 Micro-Pattern Gaseous Detectors	17
³⁵	1.4 Orthogonal Fields TPC at IEAP CTU	19
³⁶	1.4.1 Motivation and Associated Challenges	20
³⁷	1.4.2 Coordinate Systems and Dimensions	20
³⁸	1.4.3 Magnetic Field Simulation	22
³⁹	2 Track Simulation	26
⁴⁰	2.1 Microscopic Simulation	26
⁴¹	2.1.1 First testing track	27
⁴²	2.1.2 Grid-like testing sample	27
⁴³	2.2 Runge-Kutta Simulation	27
⁴⁴	2.2.1 Testing sample	30
⁴⁵	3 Track Reconstruction	32
⁴⁶	3.1 Reconstruction Assuming Steady Drift	32
⁴⁷	3.2 Ionization Electron Map	33
⁴⁸	3.2.1 Map Simulation	37
⁴⁹	3.2.2 Gradient Descent Algorithm	40
⁵⁰	3.2.3 Interpolation on the Inverse Grid	41
⁵¹	3.3 Reconstruction testing	43
⁵²	3.4 Discrete Reconstruction	44
⁵³	4 Energy Reconstruction	47
⁵⁴	4.1 Cubic Spline Fit	47
⁵⁵	4.2 Circle and Lines Fit	49
⁵⁶	4.2.1 Two-dimensional fit	50
⁵⁷	4.2.2 Three-dimensional fit	51
⁵⁸	4.2.3 Testing on a Runge-Kutta sample	54

59	4.3 Runge-Kutta Fit	54
60	4.3.1 Testing on a microscopic sample	57
61	Conclusion	58
62	Bibliography	62
63	List of Abbreviations	71

⁶⁴ Motivation

⁶⁵ Or chapter 1? MFF UK thesis template uses Introduction as an unnumbered
⁶⁶ chapter, but it's not clear how they handle numbering inside the chapter. A Time
⁶⁷ Projection Chamber (TPC) [refs] is a gaseous detector that reconstructs charged
⁶⁸ particle trajectories by measuring the positions and drift times of ionization elec-
⁶⁹ trons (and sometimes also ions) created in the gas. The energies of these particles
⁷⁰ can be inferred from the curvatures of their trajectories in a magnetic field.

⁷¹ The goal of this thesis is to develop an algorithm for the reconstruction of
⁷² charged particle trajectories and energy in an *atypic* TPC with orthogonal elec-
⁷³ tric and magnetic fields, hereafter referred to as the Orthogonal Fields TPC
⁷⁴ (OFTPC), used in the X17 project at the Institute of Experimental and Ap-
⁷⁵ plied Physics, Czech Technical University in Prague (IEAP CTU). Furthermore,
⁷⁶ we present the results of testing of several (gradually improving) developed algo-
⁷⁷ rithms with different samples of simulated data. Put this somewhere, (maybe just
⁷⁸ the abstract?). We use the Garfield++ toolkit [1] for simulations in combination
⁷⁹ with the ROOT framework [2] for data analysis and visualization. Some of our
⁸⁰ more demanding simulations are run on the MetaCentrum grid [3].

⁸¹ The X17 project in IEAP CTU aims to reproduce measurements of anomalous
⁸² behavior in the angular correlation distribution of pairs produced by the Internal
⁸³ Pair Creation (IPC) mechanism [4] during the decay of certain excited nuclei
⁸⁴ (⁸Be, ¹²C, and ⁴He) observed by a team at ATOMKI in Hungary. I would leave
⁸⁵ this here as a short summary before I explain it in more detail in the sections
⁸⁶ below.

⁸⁷ Add citations: X17 project, VdG. Maybe also TPC, etc.

⁸⁸ 0.1 ATOMKI Anomaly

⁸⁹ Many different theories propose the existence of *new light boson(s)* that are weakly
⁹⁰ coupled to ordinary matter [5]. These particles are potential dark matter candi-
⁹¹ dates and could contribute to a solution of other issues with the Standard Model,
⁹² such as the strong CP problem¹ and the anomalous muon magnetic moment. Mass
⁹³ range of axions?

⁹⁴ A possible way of detecting such bosons with a short lifetime is to observe
⁹⁵ nuclear transitions of excited nuclei. If a boson was emitted during the transition
⁹⁶ and subsequently decayed into an electron-positron pair, we could observe this as
⁹⁷ a peak on top of the standard e^+e^- (both cursive and upright forms are used in
⁹⁸ different articles) angular correlation from the Internal Pair Creation (IPC) and
⁹⁹ the External Pair Creation (EPC).

¹⁰⁰ 0.1.1 ATOMKI Measurements

¹⁰¹ Historically, there were several measurements of the IPC in nuclear transitions
¹⁰² in ⁸Be at Institute für Kernphysik (Frankfurt) [6, 7, 8] and at ATOMKI (Debre-
¹⁰³ cen, Hungary) [9, 10] resulting in different anomalies with invariant mass in the

¹The CP symmetry could be violated in strong interactions according to the current formulation of quantum chromodynamics, but no such violation is observed.

range 5 – 15 MeV. This motivated the development of a better spectrometer at ATOMKI.

In 2015, a group at ATOMKI observed an anomalous IPC in ${}^8\text{Be}$ [11]. They used the ${}^7\text{Li}(p, \gamma){}^8\text{Be}$ reaction at the $E_p = 1030$ keV proton capture resonance to prepare the 18.15 MeV excited state ($J^\pi = 1^+, T = 0$). This state decays predominantly through M1 transitions to the ground state ($J^\pi = 0^+, T = 0$) and to the 3.03 MeV state ($J^\pi = 2^+, T = 0$) [12]. [Transition figure – all transitions of isotopes? IPC figure?](#)

The angular correlation of the e^+e^- pairs created internally in these transitions were measured and compared to the simulation; results from a narrow $E_{\text{sum}} = 18$ MeV region are shown in Fig. 0.1a. The simulation includes boson decay pairs for different boson masses. The disparity parameter y is used to describe the asymmetry of energy between the two particles. It is defined as

$$y = \frac{E_{e^-} - E_{e^+}}{E_{e^-} + E_{e^+}}, \quad (0.1)$$

where E_{e^-} and E_{e^+} are the kinetic energies of the electron and positron.

Their experimental setup was later upgraded ([details?](#)) and used for new measurements. In 2022 the ${}^8\text{Be}$ anomaly was also measured using the $E_p = 441$ keV resonance to produce the 17.64 MeV excited state ($J^\pi = 1^+, T = 1$) which again decays primarily to the ground state and the 3.03 MeV state [12]. The anomaly was also verified for $E_p = 650$ and 800 keV where E1 transitions from the direct proton capture dominate [13]. The results for e^+e^- with $E_{\text{sum}} \in [13.5, 20]$ MeV are shown in Fig. 0.1b.

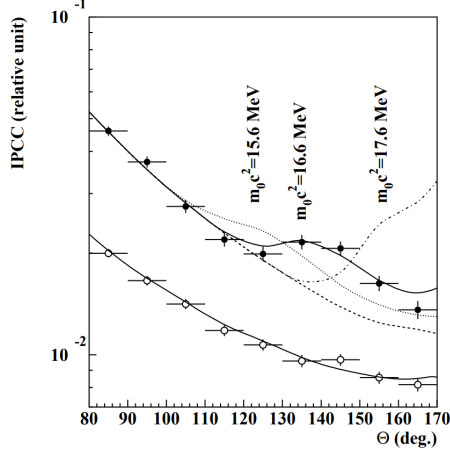
The newer setup was also used in 2021 to study the ${}^3\text{H}(p, e^+e^-){}^4\text{He}$ reaction at $E_p = 510, 610$ and 900 keV [14], inducing direct and resonant capture populating the overlapping first 20.21 MeV ($J^\pi = 0^+$) and second 21.01 MeV ($J^\pi = 0^-$) excited states [15]. The comparison of simulated and measured e^+e^- pair angular correlations in the $E_{\text{sum}} \in [18, 22]$ MeV region is shown in Fig. 0.1c.

In 2022, another anomaly was measured in the ${}^{11}\text{B}(p, e^+e^-){}^{12}\text{C}$ process [16]. The $E_p = 1388$ keV resonance was used to populate the 17.23 MeV excited state ($J^\pi = 1^-, T = 1$) with a large width $\Gamma = 1.15$ MeV [17]. This state decays mainly through E1 transitions to the ground state $J^\pi = 0^+$ and to the 4.44 MeV state $J^\pi = 2^+$. To compensate for energy losses in the target, five energies in the range $E_p = 1.5\text{--}2.5$ MeV were used. The experimental angular correlation for the 17.23 MeV transition to the ground state is shown in Fig. 0.1d.

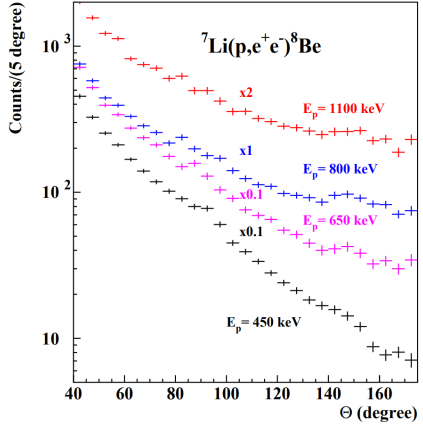
Possible explanations of the anomaly include experimental effects, higher order processes in the Standard Model [18, 19] or even a protophobic fifth force mediated by a new 17 MeV boson X17 [20]. [Not sure if the introduction should be referenced since even though it is related, it is an independent theory developed only \(?\) to explain these measurements. Zhang and Miller: <https://www.sciencedirect.com/science/article/pii/S0370269321000010> Paper from IEAP CTU: <https://arxiv.org/pdf/2309.12469.pdf>](#)

0.1.2 Other Experiments

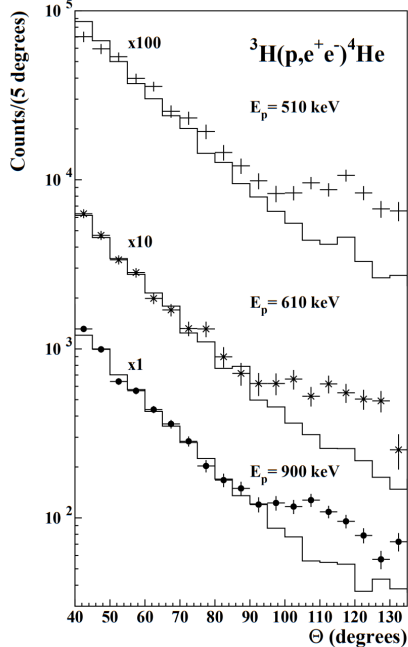
Since the ATOMKI measurements, several experiments have been initiated to attempt to replicate the results and search for the hypothetical X17 particle. The



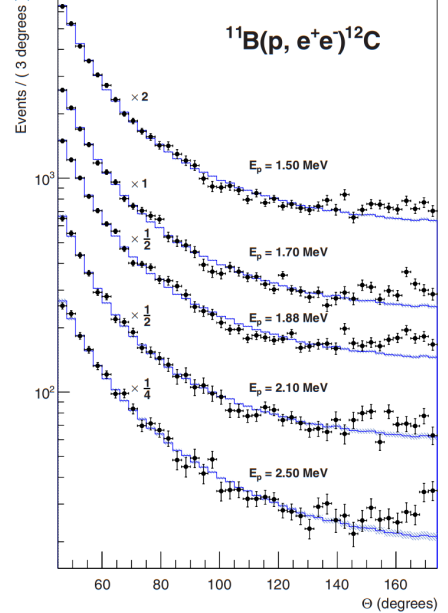
(a) Experimental e^+e^- pair correlations measured in the ${}^7\text{Li}(p, e^+e^-){}^8\text{Be}$ reaction with $|y| \leq 0.5$ (closed circles) and $|y| \geq 0.5$ (open circles) [11].



(b) Experimental e^+e^- pair correlations measured in the ${}^7\text{Li}(p, e^+e^-){}^8\text{Be}$ reaction with the improved setup for different proton beam energies [13].



(c) Experimental e^+e^- pair correlations measured in the ${}^3\text{H}(p, e^+e^-){}^4\text{He}$ reaction with $|y| \leq 0.3$ for different proton beam energies [14].



(d) Experimental e^+e^- pair correlations measured in the ${}^{11}\text{B}(p, e^+e^-){}^{12}\text{C}$ reaction for different proton beam energies [16].

Figure 0.1: The ATOMKI anomalous IPC measured for different nuclei.



Figure 0.2: Results from the Hanoi spectrometer – angular e^+e^- pair correlations measured in the ${}^7\text{Li}(p, e^+e^-){}^8\text{Be}$ reaction at $E_p = 1225$ keV [21].

following experiments have already produced results. Could cite the ATOMKI review paper here. NA64 at SPS: <https://arxiv.org/pdf/1803.07748>.

Two-arm e^+e^- spectrometer in Hanoi

The anomaly in ${}^8\text{Be}$ has been observed with a high ($> 4\sigma$ That's all they write in their article.) confidence by a team at the Hanoi University of Sciences for $E_p = 1225$ keV [21]. They built a two-arm spectrometer in collaboration with ATOMKI and calibrated it using the 17.6 MeV M1 transition. The results are shown in Fig. 0.2.

Collisions at Nuclotron in Dubna

At the Joint Institute for Nuclear Research in Dubna, signal in the form of enhanced structures in the $\gamma\gamma$ spectra at ~ 17 and ~ 38 MeV invariant masses for $p + \text{C}$, $d + \text{C}$ and $d + \text{Cu}$ reactions at momenta 5.5, 2.75, and 3.83 GeV per nucleon [22]. Monte Carlo simulations support the conclusion that the signals are a consequence of a decay of unknown particles X17 and E38.

The MEG II (Muon Electron Gamma) experiment

Experiments using the ${}^7\text{Li}(p, e^+e^-){}^8\text{Be}$ reaction were carried out at the Paul Scherrer Institute with the MEG II superconducting solenoid spectrometer [23]. Analysis of the data with $E_p = 1080$ keV exciting both of the resonances (beam fully stopping in the target) found no significant evidence supporting the X17 hypothesis, results are shown in Fig. 0.3. An upper bound (at 90% confidence) on the X17-to- γ branching ratio was set at $1.2 \cdot 10^{-5}$ for the 18.15 MeV state (larger than the ratio $5.8 \cdot 10^{-6}$ obtained by ATOMKI in 2016). Could add their 90% C.L bounds figure also. Insufficient statistics – 6.2 % (1.5σ) p-value.

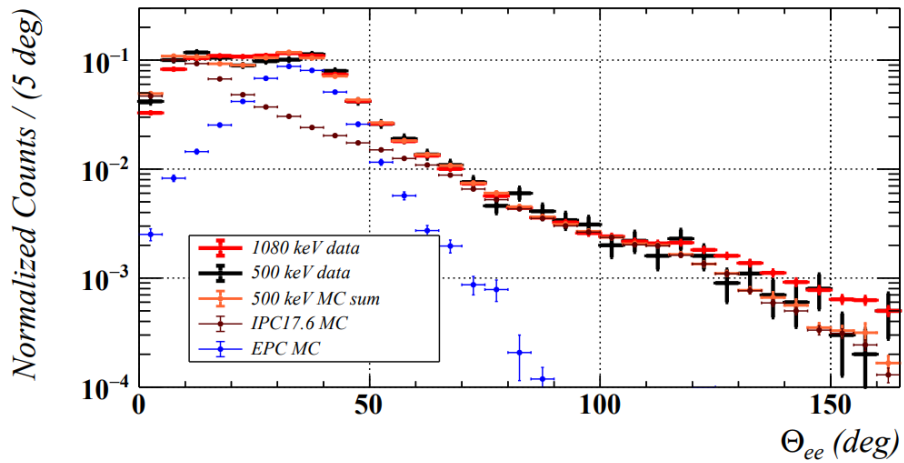


Figure 0.3: Results from the MEG II experiments – angular correlation of e^+e^- pairs with $E_{\text{sum}} \in [16, 20]$ MeV measured in the ${}^7\text{Li}(p, e^+e^-){}^8\text{Be}$ reaction with proton beam energies 500 and 1080 keV. The 500 keV dataset is fitted with Monte Carlo of both the IPC deexcitation and the EPC produced by gammas [23].

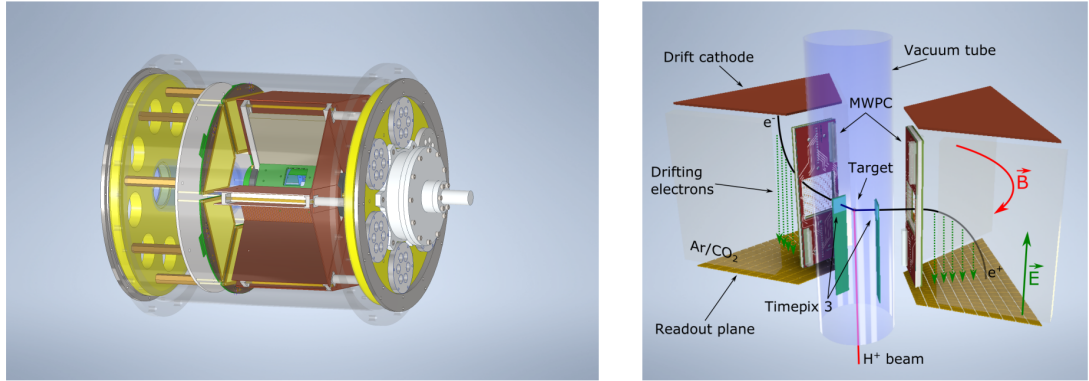


Figure 0.4: Schematics of the detector at the Van der Graaff facility at IEAP CTU (ref.).

170 0.2 X17 Project at IEAP CTU

171 The aim of the X17 project at the Van der Graaff facility of the Institute of
 172 Experimental and Applied Physics, Czech Technical University in Prague is to
 173 reproduce the results of the original ATOMKI experiments with ${}^7\text{Li}$ and ${}^3\text{H}$ tar-
 174 gets using an independent e^+e^- spectrometer. In order to effectively measure the
 175 anomaly, we need to reconstruct both the energy and the angular correlation of
 176 the e^+e^- pairs. The spectrometer will use three layers of detectors to achieve this
 177 – Timepix3 (TPX3) silicon pixel detector and Multi-Wire Proportional Cham-
 178 ber (MWPC) layers for the angle reconstruction and a Time Projection Cham-
 179 ber (TPC) layer for the energy reconstruction. The schematics of the prepared
 180 detector is in Fig. 0.4 Spectrometer CAD drawing (coordinates here or next chap-
 181 ter?). Cite some VdG paper, mention grant? Using https://cernbox.cern.ch/pdf-viewer/public/rf0oU1nqVLN3acZ/LuzH_submitted.pdf.

183 The energy of e^+e^- pair produced in the reaction is given by the energy

available E_r in the reaction and can be distributed between them arbitrarily. Nonetheless in the decay of the hypothetical X17 particle, electron and positron should have similar energy and we can therefore use a cut $|y| \leq 0.5$ in the disparity parameter (defined in Equation 0.1 **it was already used in ATOMKI figure captions, that's why it is defined prior to this**). Interesting events should rarely have a particle with an energy below $E_r/4$ (roughly 4 MeV). Electrons with such low energies are scattered significantly by even a thin layer of relatively light material, for this reason the TPX3 layer will be inside of the vacuum tube and the tube will have a thinned aluminum segment or KaptonTM windows.

TPX3 can measure (in each $55 \times 55 \mu\text{m}$ pixel of its 256×256 grid) time-of-arrival (ToA) with 1.6 ns precision and time-over-threshold (ToT) which reflects the deposited energy. This potentially allows 3D tracking if we increase the chip thickness at the cost of increased scattering. The layer can reconstruct the reaction vertex and the angular correlation with high precision.

The layer of MWPCs with sensitive area $40 \times 38 \text{ mm}^2$ will be outside of the beam pipe. It will provide an extra point on the particle trajectory which can help with the estimation of the reaction vertex and improve the TPC performance by providing its entry point.

The TPCs that are the subject of this thesis, are in a magnetic field generated by permanent magnets positioned between them and provide 3D track reconstruction and subsequent momentum and particle identification (its charge, or even type based on its stopping power). They avoid radiative losses thanks to the low density and atomic number of the gas mixture. For the readout, triple Gas Electron Multiplier (GEM) will be used. The magnetic field layout in our TPCs is atypical – orthogonal to the electric field inside the chamber, this is why we call them Orthogonal Fields TPC (OFTPC). Further details about our OFTPCs are provided in section 1.4.

1. Time Projection Chamber

A Time Projection Chamber (TPC) is a gaseous detector that uses the drift times of ionization electrons produced by a charged particle in an (ideally uniform) electric field to reconstruct the particle's 3D trajectory. The 2D projection is measured by an amplification stage at the end of the drift volume. When placed inside a magnetic field (typically parallel to the electric field), the momentum of the incident particle can be inferred from the curvature of its trajectory. Particle identification is also possible using the ionization energy loss inside the TPC (see Fig. 1.1). The following text (including Secs. 1.1 and 1.3) is based primarily on the reviews by Hilke [24] and the Particle Data Group [25].

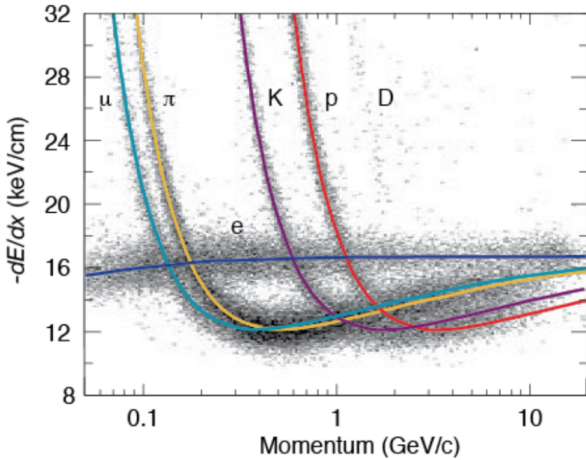


Figure 1.1: Particle identification in the PEP-4 TPC at SLAC based on the energy loss per distance $\frac{dE}{dx}$ in the 80:20 Ar:CH₄ filling at 8.5 atm pressure [26]. The reference doesn't point to the original PEP-4 article because this adapted version of the original picture that they used in the DUNE article looks better.

Large TPCs are sensitive to small distortions in the electric field (imperfections in the field cage, accumulation of positive ions in the gas volume) and to $\mathbf{E} \times \mathbf{B}$ effects on the drift velocity (see Eq. 1.1 below). Diffusion of the drifting electrons deteriorates the spacial resolution significantly, but it can be reduced up to ~ 10 times by a strong $\mathbf{B} \parallel \mathbf{E}$ field (see Eq. 1.8).

In neutrino and other rare-event experiments, large (up to 600 tons) Liquid Argon TPCs (LArTPCs) are used for particle identification and calorimetry. The ionization electrons can be drifted for many meters with a small diffusion. Scintillation photons are also measured. Negative ions?

1.1 Charge transport in gases

When a charged particle crosses the volume of a TPC, it loses energy by excitation and ionization of the detector gas (how much – from dE/dx + density → footnote?). Most ionizing collision produce a single ionization electron, sometimes a few secondary electrons are produced near the collision vertex, creating a cluster. In rare cases, the ionization electron has energy large enough to create

236 a measurable track, such an electron is called a δ -electron (terminology, just like
237 bellow – technically it's a (primary) ionization electron causing other (secondary)
238 ionization).

239 After their release, the ionization electrons are separated from positive ions
240 by the electric field and they both drift and diffuse in opposite directions towards
241 the electrodes. The charges are accelerated (different word?) by the electric field
242 inside the chamber, and they lose speed by colliding with the gas particles, quickly
243 reaching a constant (for a given field \mathbf{E}, \mathbf{B}) mean drift velocity. The electrons can
244 be absorbed by electronegative impurities, such as halides, O_2 , and H_2O .

245 In mixtures with a noble gas component, if the excitation energy of the noble
246 gas is higher than the ionization potential of an admixture, more free electrons can
247 be produced through collisions of the gas particles (so-called Penning transfer)
248 and through absorption of emitted photons.

249 If the electric field is strong enough, the electrons can cause further ion-
250 ization and excitation of the gas, leading to the development of a Townsend
251 avalanche (ref).

252 1.1.1 Drift

253 In many gases (called "hot", e.g., Ar or CH_4), the drift velocity is much greater
254 than that of their thermal motion thanks to a high proportion of elastic collisions.
255 On the other hand, "cold" gases like CO_2 have a higher proportion of inelastic
256 collisions (e.g., thanks to the excitation of rotational and vibrational states) and
257 therefore much lower (value? magnitude (implied?)) drift velocity. Or maybe it
258 is not so simple, because slowing down the electrons inelastically into a certain
259 minimum of elastic scattering cross-section increases drift velocity? In case of
260 $\text{Ar}+\text{CO}_2$ this is clearly not the case for low electric fields, so maybe irrelevant
261 here (or is the effect opposite for small additions?).

262 The ions produced by the ionization lose a significant portion of their energy
263 during each collision since their mass is close to the mass of the gas particles (see
264 the source material – average energy loss during collision $\Delta E = \frac{2m_i M}{(m_i + M)^2}$, this
265 way it's more accurate). This, together with their large collision cross section,
266 makes their drift velocity much smaller (about three orders of magnitude) and
267 their energy is close to thermal. Since their momenta are not randomized to such
268 an extent during collisions, their diffusion is smaller (move this to the diffusion
269 subsection, reformulate).

270 The drift is also influenced by the magnetic field. Langevin derived a good
271 approximation for the drift velocity vector:

$$\mathbf{v}_d = \left(\frac{\mathbf{E}}{\|\mathbf{E}\|} + \omega\tau \frac{\mathbf{E} \times \mathbf{B}}{\|\mathbf{E}\| \|\mathbf{B}\|} + \omega^2\tau^2 \frac{\mathbf{E} \cdot \mathbf{B}}{\|\mathbf{E}\| \|\mathbf{B}\|} \cdot \frac{\mathbf{B}}{\|\mathbf{B}\|} \right) \frac{q\tau}{m(1 + \omega^2\tau^2)} \|\mathbf{E}\|, \quad (1.1)$$

272 where q is the charge of the particle, m is its mass, τ is the mean time between
273 collisions and $\omega = \frac{q}{m} \|\mathbf{B}\|$ is the Larmor frequency. For orthogonal fields $\mathbf{E} \perp \mathbf{B}$,
274 it can be shown that the magnetic field bends the direction of the drift by the
275 so-called Lorentz angle:

$$\tan \psi = -\omega\tau. \quad (1.2)$$

276 The drift of ions is only negligibly influenced by the magnetic field ($\omega\tau \sim 10^{-4}$
277 is small due to the low drift velocity – better (?) because it takes τ into account

278 and differs only by E/B ratio (if the magnetic contribution to the magnitude is
279 small)). In a standard TPC, \mathbf{E} is parallel to \mathbf{B} and the influence of the magnetic
280 field on the drift is minimal. Without magnetic field, we can write

$$\mathbf{v}_d = \frac{q\tau}{m} \mathbf{E} = \mu \mathbf{E}, \quad (1.3)$$

281 where μ is called charge mobility.

282 1.1.2 Diffusion

283 All of the theory is from the same source mentioned at the beginning. None of the
284 simulations explicitly depend on this. Due to collisions, a cloud of electrons or
285 ions originating from the same point will show a Gaussian density distribution at
286 time t while drifting in the electric field $\mathbf{E} = (0, 0, E_z)$ along the z -coordinate (287 coordinates defined by the electric field):

$$\rho(x, y, z, t) = (4\pi Dt)^{-\frac{3}{2}} \exp\left(-\frac{x^2 + y^2 + (z - v_d t)^2}{4Dt}\right), \quad (1.4)$$

288 where the diffusion coefficient D can be expressed as

$$D = \frac{\lambda^2}{3\tau} = \frac{\lambda v_d}{3} = \frac{v_d^2 \tau}{3} = \frac{2\varepsilon\tau}{3m}, \quad (1.5)$$

289 where λ is the mean free path and ε the mean kinetic energy. The lateral diffusion
290 width σ_x after a drift distance L can be expressed as

$$\sigma_x^2 = 2Dt = \frac{4\varepsilon L}{3qE_z}. \quad (1.6)$$

291 The minimal diffusion width is given by the lowest possible energy of the particles
292 $\varepsilon_{\text{th}} = \frac{3}{2}kT$ (corresponding to thermal motion):

$$\sigma_{x, \text{min}}^2 = \frac{2kTL}{qE}. \quad (1.7)$$

293 For electrons in "cold gases" (e.g., Ar/CO₂ mixture), the diffusion approaches this
294 limit up to a certain field intensity (~100 V/cm at 1 atm pressure)¹. In reality, the
295 transversal diffusion of electrons can differ significantly from their longitudinal
296 diffusion and simulations are necessary to get a precise result.

297 In most TPCs, the transversal (but not the longitudinal) diffusion is reduced
298 by the magnetic field, since it is parallel to the electric field and curves the
299 diffusing electrons around their mean trajectory:

$$\frac{D_T(B)}{D_T(0)} = \frac{1}{C + \omega^2 \tau_2^2}, \quad (1.8)$$

300 where C and τ_2 are parameters dependent on the gas used. At low intensity of
301 the magnetic field, we can use an approximation $C \approx 1$ and $\tau_2 \approx \tau$.

¹For us $\sigma_{x, \text{min}} = 0.45$ mm, quite close to the actual diffusion 0.5-0.7 mm – details of the calculation.

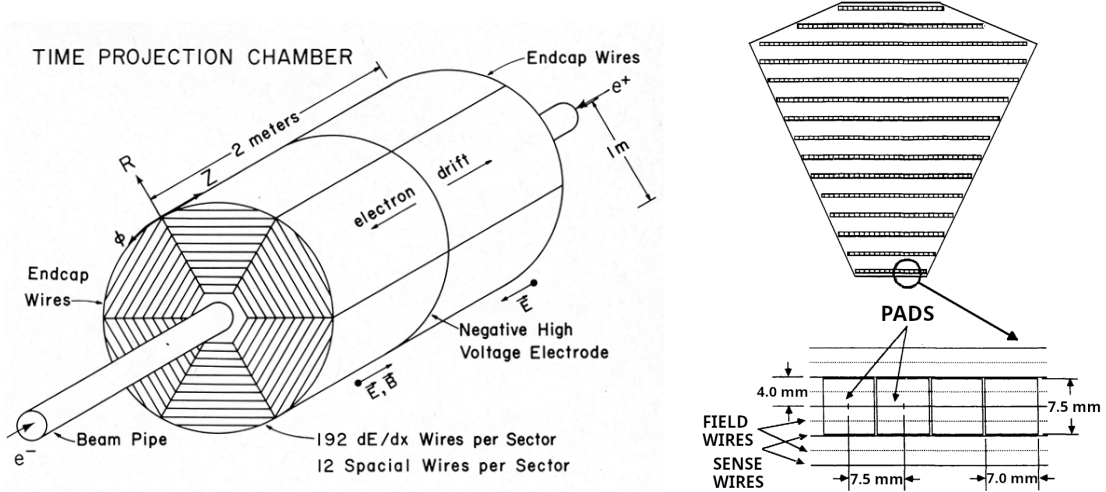


Figure 1.2: Schematic view of the PEP-4 TPC [28]. A charged particle produced in a collision in the beam pipe creates a spiral ionization track in the magnetic field. The central cathode then accelerates ionization electrons towards the endcap anode wires where they are multiplied and read out. A TPC sector with a detailed view of one of the pad rows is shown on the right [29].

302 1.2 Examples of TPCs

303 1.2.1 The original TPC at PEP-4 at SLAC

304 The original TPC used in the PEP-4 experiment at SLAC in the 1980s (Fig. 1.2)
 305 was a $2\text{ m} \times 2\text{ m}$ hollow cylinder with a central cathode that produced a strong
 306 electric field 750 V/cm , making the ionization electrons drift towards one of the
 307 endcaps [27]. It was filled with a 80:20 Ar:CH₄ mixture at 8.5 atm pressure
 308 and placed inside a 0.4 T solenoidal magnetic field. The readout consisted of
 309 MWPCs, where electrons are accelerated towards the anode wires fast enough to
 310 further ionize the gas and cause an avalanche (details are provided in Sec. 1.3.1).
 311 The wires had radial spacing 4 mm, fifteen of the sense wires had the cathode
 312 segmented into $7.0 \times 7.5\text{ mm}^2$ pads 4 mm under them (Fig. 1.2 right). When
 313 collecting electrons on the anode wire, signal is induced on the nearest 2-3 cathode
 314 pads.

315 1.2.2 ALICE TPC

316 The ALICE TPC (Fig. 1.3) is the main detector used for charged particle tracking
 317 and recognition in collisions at the ALICE experiment at the CERN LHC [30].
 318 Similarly to PEP-4, it is a hollow cylinder with outer radius 2.5 m and height 5 m.
 319 It is placed in a 0.5 T solenoidal magnetic field, and the central cathode generates
 320 a 400 V/cm electric field inside the field cage. The gas mixture in the detector
 321 is 90:10:5 Ne:CO₂:N₂, mainly chosen for its higher ion mobility compared to Ar
 322 mixtures. In 2020, the readout of the TPC was upgraded from MWPCs to stacks
 323 of four GEM foils (principle described in Sec. 1.3.2). This allows reading events
 324 continuously at a higher rate.

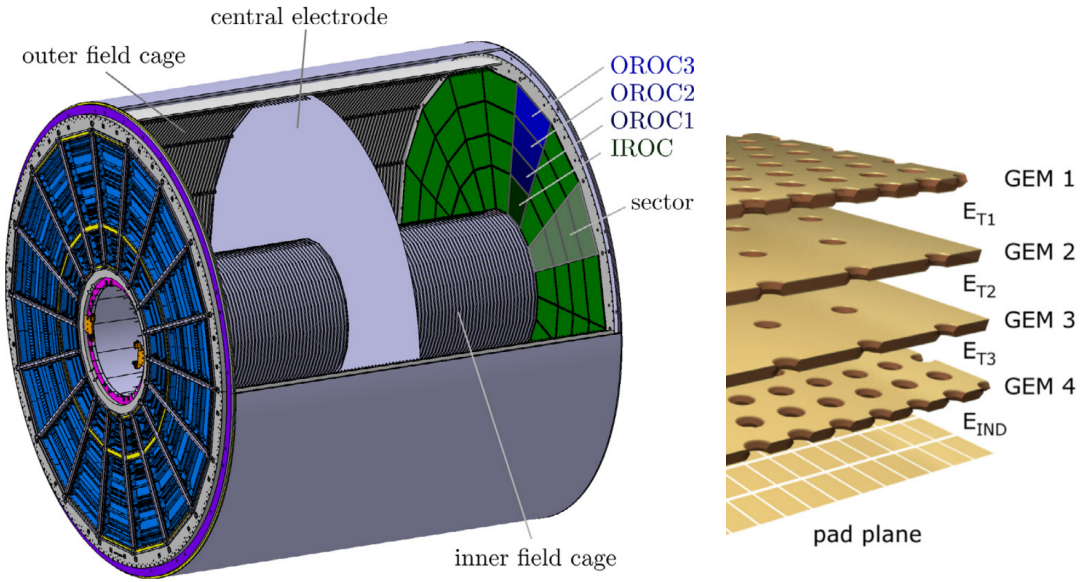


Figure 1.3: Schematic view of the ALICE TPC [31]. The readout at each endcap is divided into 18 sectors, each subdivided into an Inner Readout Chamber (IROC) with one GEM stack and Outer Readout Chamber (OROC) with three GEM stacks. A visualization of a GEM stack is on the right [32].

325 1.2.3 CERES/NA45 radial-drift TPC

326 In 1998, the CERES/NA45 (Cherenkov Ring Electron Spectrometer) experiment
 327 (Fig. 1.4) at the CERN SPS was upgraded with the first radial-drift TPC (rTPC)
 328 to achieve a higher momentum resolution [33]. Unlike a standard TPC, the elec-
 329 tric field 600–200 V/cm was arranged radially with the magnetic field (inhomoge-
 330 neous, up to 0.5 T) by two solenoidal coils with opposite polarity. The outward
 331 drift of the ionization electrons is affected by the crossing fields as shown in Eq. 1.1
 332 and the drift velocity is not uniform due to the varying electric field. The rTPC
 333 was filled with an 80:20 Ne:CO₂ gas mixture, which has relatively small diffu-
 334 sion coefficients and Lorentz angle. The readout was handled by conventional
 335 MWPCs (Fig. 1.5).

336 The field configuration in an rTPC enables a larger number of pads compared
 337 to a standard TPC, leading to improved spatial resolution and possibility of larger
 338 multiplicity rates. Since the drift time is lower, the detector is faster.

339 After an algorithm described in this thesis was developed for our OFTPCs at
 340 IEAP CTU, we noticed the similarities with the approach used by the CERES/NA45||
 341 rTPC, when accounting for the transport process of charged clusters in the com-
 342 plex fields. The detector hit coordinates (pad, time, and plane) were transformed
 343 using look-up tables. The tables were calculated using a Runge-Kutta method to
 344 integrate the Langevin approximation of the drift velocity (Eq. 1.1). The drift
 345 velocity in the radial field was calibrated using seven parallel laser rays. This
 346 calibration was then used to make a correction compared to the MAGBOLTZ
 347 Monte Carlo drift [34]. **Measured mobility differs significantly from MAGBOLTZ,**
 348 **but this might be improved in the newer versions?** The tracks were fitted using
 349 reference tables with hit coordinates of tracks simulated with GEANT Monte
 350 Carlo (**not such a big problem for us right now, might be an idea if the recon-**

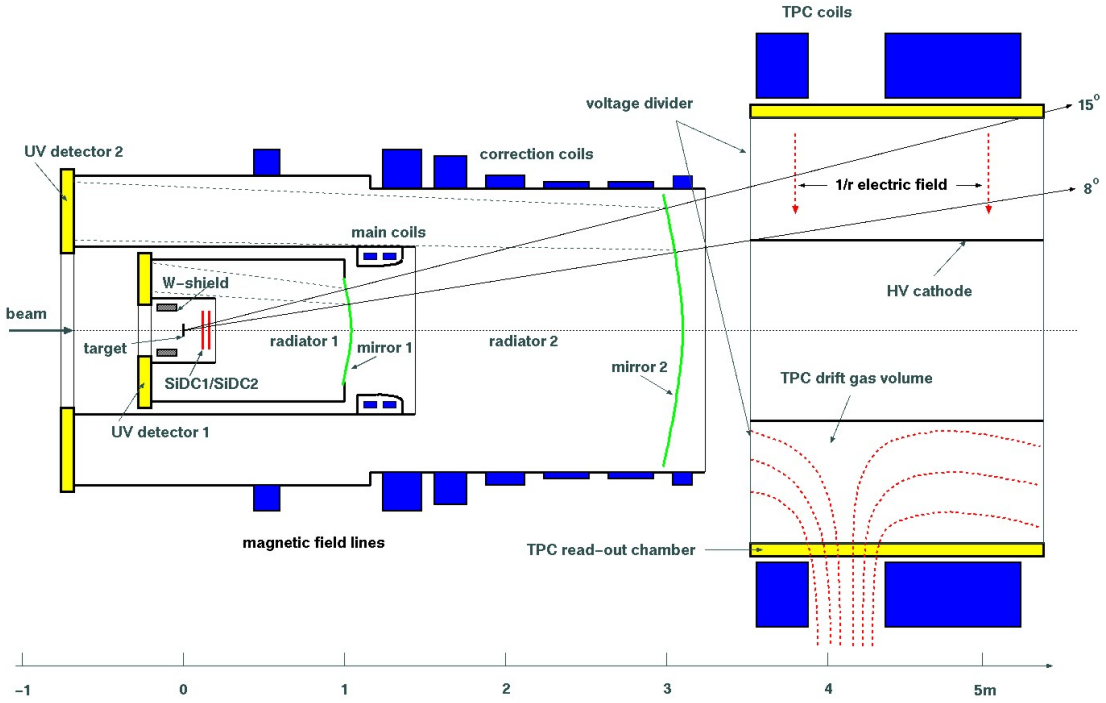


Figure 1.4: Experimental setup of the CERES/NA45 experiment with two Ring Imaging Cherenkov Counters (RICHs) on the left and a rTPC on the right. The magnetic field (red) is generated by two solenoidal coils (blue) with opposite polarity. Produced ionization electrons drift outward radially towards the readout chamber (yellow) [33].

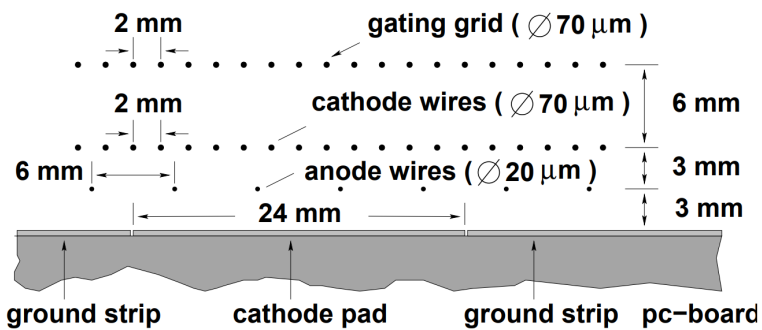


Figure 1.5: Cross section of a CERES/NA45 readout MWPC. The wires are stretched in the azimuthal direction above the pad plane. The gating grid controls the passage of electrons and ions. [33].

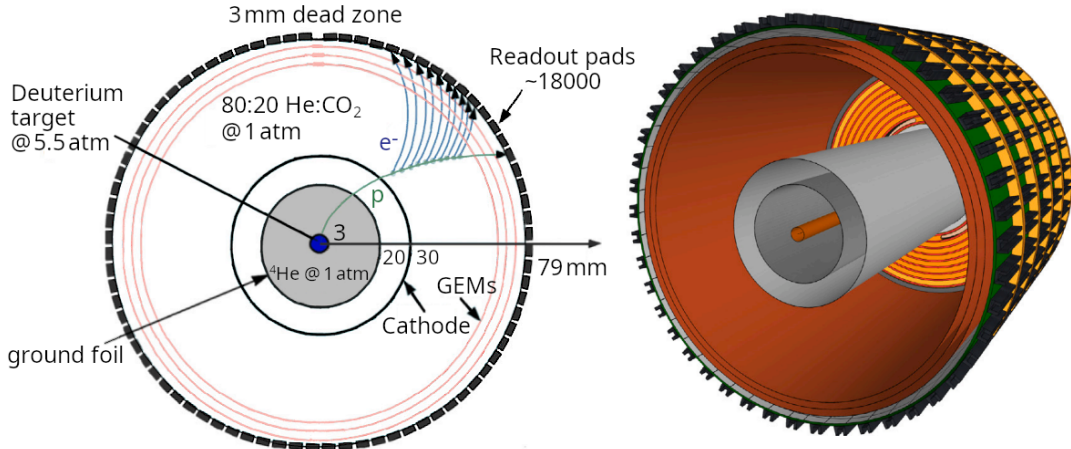


Figure 1.6: Schematic view of the BONuS12 rTPC [35].

351 structure gets too slow).

352 1.2.4 Other interesting radial-drift TPCs

353 muEDM at PSI: [https://arxiv.org/pdf/2307.01535](https://arxiv.org/pdf/2307.01535.pdf),

354 FTPC at STAR at RHIC: [https://arxiv.org/pdf/nucl-ex/0211014](https://arxiv.org/pdf/nucl-ex/0211014.pdf)

355 BONuS12 rTPC

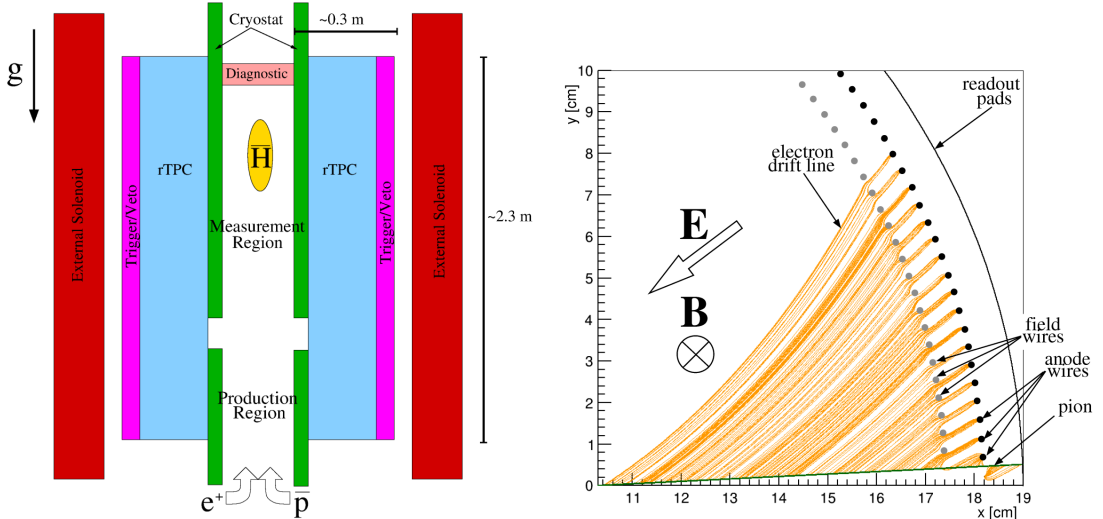
356 In 2020, the Barely Off-shell Neutron Structure 12 GeV (BONuS12) experiment
 357 used an rTPC (Fig. 1.6) to measure low-momentum spectator protons produced
 358 in $e^-d \rightarrow e^-p_sX$ scattering [35]. It was filled with a 80:20 He:CO₂ gas mixture and
 359 placed inside a 4 T solenoidal magnetic field, perpendicular to the radial electric
 360 field (1100 V/cm on average), tilting the drift (see Eq. 1.2). The amplification
 361 used cylindrical triple GEM stacks.

362 Garfield++ simulations and study of reconstructed tracks have shown that the
 363 radial component of the drift velocity almost proportional to the radial electric
 364 field, and the r -coordinate can be reconstructed using an analytical formula. Sim-
 365 ilarly, the azimuthal component is nearly proportional to the radial component,
 366 resulting in a largely constant Lorentz angle between the radial and actual direc-
 367 tion, and the ϕ -coordinate can be solved analytically. The remaining z -coordinate
 368 stays undistorted. The momentum is determined by fitting tracks with a helix,
 369 while accounting for the energy losses (the small variability of magnetic field along
 370 the z -axis has a negligible effect).

371 ALPHA-g rTPC

372 In 2023, the Antihydrogen Laser Physics Apparatus (ALPHA) collaboration pub-
 373 lished results of measurements of antihydrogen (\bar{H}) annihilation² after release
 374 from magnetic confinement, showing that it behaves in a way consistent with grav-
 375 itational attraction to the Earth [36]. They used a 2.3 m long rTPC (Fig. 1.7a)

²The main \bar{p} annihilation mode is into several π^\pm and π^0 , only the π^\pm tracks are long enough to be reconstructed. The scattering of π^\pm is not negligible, and photons from π^0 decay create e^+e^- pairs as background.



(a) Sketch of ALPHA-g. Antiprotons and positrons are injected from the bottom and form \bar{H} in a Penning trap while being cooled by the cryostat (green). The annihilation is reconstructed by the rTPC (blue).

(b) Cross section view of the rTPC (Garfield++ simulation). The electrons (orange) produced by a pion track (green) drift towards the anode wires, while influenced by the axial magnetic field. The size of the field and anode wires is exaggerated.

Figure 1.7: Schematic view of the ALPHA-g detector [37].

with a 40 cm outer and 20 cm inner diameter in a 1 T solenoidal magnetic field, and filled with an Ar/CO₂ mixture [37]. The readout consists of an MWPC (Fig. 1.7b). The radial confinement of the cold \bar{H} is achieved with a superconducting octupole magnet, the axial with a set of so-called *mirror* coils.

The *r*-coordinate of the ionization cluster is reconstructed from the drift time using a tabulated space-time relation. The 3D position of the interaction (cluster) vertex is obtained by matching the wires and pads by drift time using a k-d tree algorithm. Reconstructed tracks are fitted with a helix using the least squares method [38].

1.3 Readout

1.3.1 Multi-Wire Proportional Chamber

In most TPCs operated in experiments, Multi-Wire Proportional Chamber (MWPC) was used for the readout (Fig. 1.8). The electrons enter the chamber through a cathode grid and get accelerated by a strong electric field towards the parallel, thin anode wires and create an avalanche, multiplying the signal. The trajectory can be reconstructed from the drift time and two coordinates measured using

- a) two segmented cathodes (wires or strips) rotated by 90° or
- b) the ratio of charge collected on two sides of the hit resistive wires.

For high counting rates, the positive ions from the avalanches accumulate, creating a space charge that distorts the electric field. This can be solved by using a gating grid near the readout plane to collect these ions at the cost of introducing a dead time in the detector.

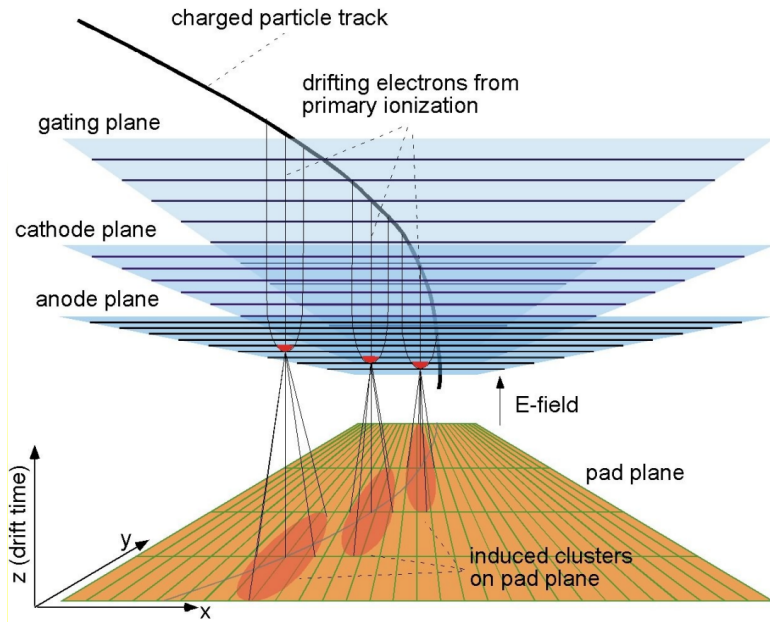


Figure 1.8: Schematic view of the ALICE MWPC readout (working principle) [39].

398 1.3.2 Micro-Pattern Gaseous Detectors

399 In order to avoid MWPC limitations (e.g., diffusion, wire $\mathbf{E} \times \mathbf{B}$ effect, space
400 charge effects), a family of Micro-Pattern Gaseous Detector (MPGD) technologies
401 are being developed. The readouts can reach higher spatial resolution (down to
402 30 μm) with faster response time (ns range) and much higher rate capability.

403 Gas Electron Multiplier

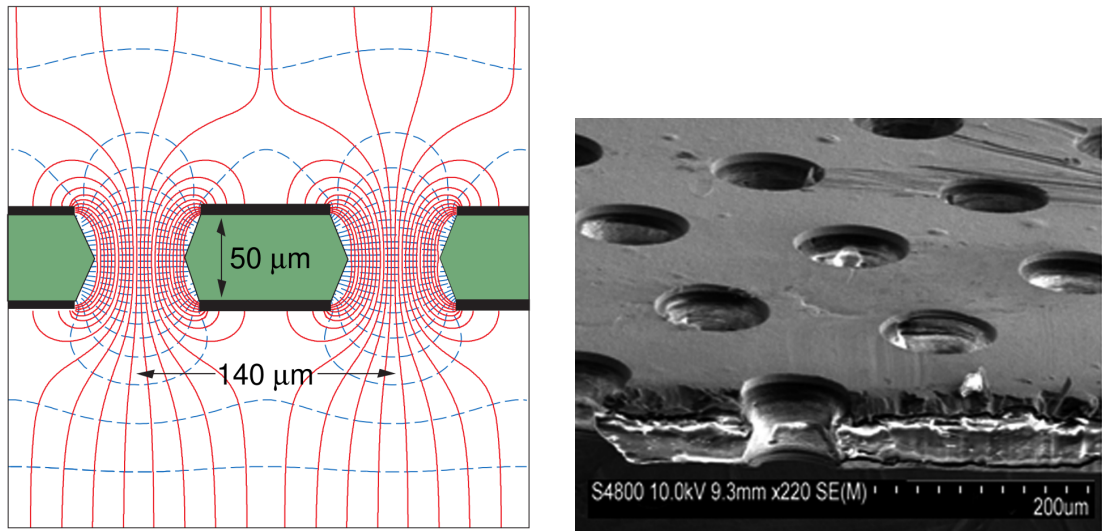
404 A Gas Electron Multiplier (GEM) is a thin metal-coated polyimide sheet with
405 a dense pattern of small, chemically etched holes (Fig. 1.9). The amplification is
406 achieved by applying voltage across the metal layers and placing the foil between
407 two moderate uniform electric fields. This creates a strong electric field inside the
408 holes that accelerates the incoming electrons and causes avalanches (see Fig. 1.10).
409 Some charges may land on the dielectric surfaces due to diffusion, modifying the
410 field and affecting gain.

411 Double or triple stacks of GEMs are usually used to create a sufficient gain
412 while maintaining stability (reducing discharges). From the last foil, the electrons
413 drift to a segmented anode where the signal is read. The ion backflow is reduced
414 compared to MWPC.

415 A cheaper alternative (especially for large area coverage) is a THick GEM
416 (THGEM) with a \sim 10-fold upscaling of geometrical parameters. It can be made
417 by mechanically drilling holes into a standard Printed Circuit Board (PCB) and
418 creating a circular rim around the holes by etching the metal coating.

419 Micromegas

420 In a MICRO-MEsh GAseous Structure (Micromegas) (in sources I viewed it is not
421 capitalized) electrons pass through a fine mesh (made out of very thin wires) into



(a) A schematic view of a GEM cell with its typical dimensions, electric field lines (red), and equipotentials (blue) [25].

(b) A scanning electron microscope image of a GEM foil [40].

Figure 1.9: Gas Electron Multiplier (GEM).

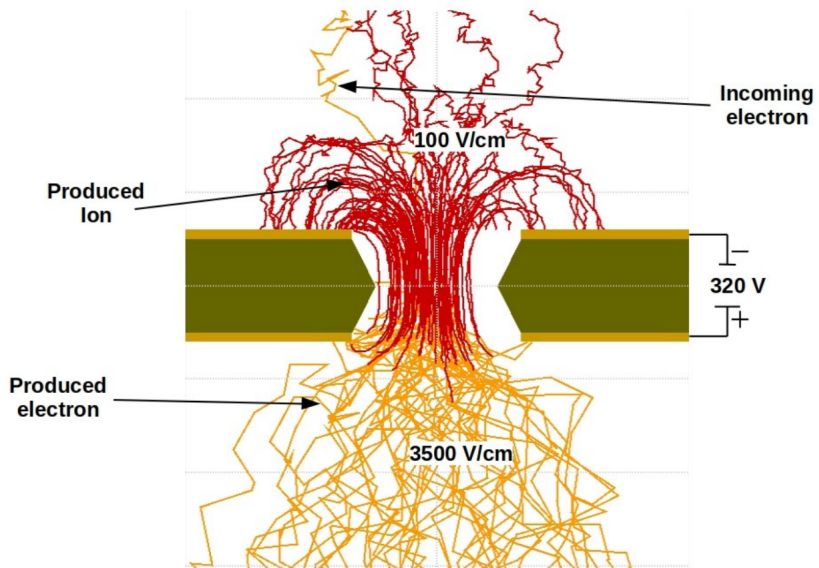
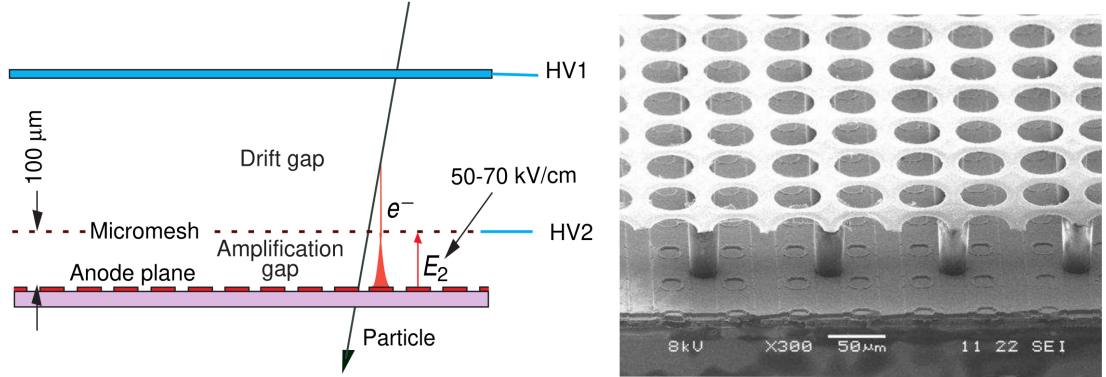


Figure 1.10: Garfield simulation of an avalanche in a GEM hole [41]. An incoming electron (orange) is accelerated in the strong electric field of the GEM and causes further ionization multiplying the number of free electrons (orange). Most of the produced cations (red) are captured by the GEM cathode.



(a) A schematic view of a Micromegas detector.

(b) A scanning electron microscope image of a Micromegas "GridPix" detector.

Figure 1.11: MICRO-MEsh Gaseous Structure (Micromegas) [25].

a narrow amplification gap where they are multiplied in the high field and read as a signal on the segmented anode (Fig. 1.11a). Very high field ($30-80 \text{ kV/cm}^2$) is necessary to achieve sufficient gain. Ion backflow is heavily suppressed by the mesh.

A Timepix chip (a high granularity pixel detector) can be used for the readout anode to achieve the best spatial resolution, making an integrated readout called GridPix (Fig. 1.11b). Thanks to the high spatial resolution, it is possible to distinguish individual electron clusters, which enables a new method of particle identification.

Other MPGDs

A Resistive Plate WELL (RPWELL) consists of a THGEM with only the top side metal-coated, mounted on a resistive film deposited on a thin isolating sheet (which is read out similarly to a Resistive Plate Chamber (RPC)). Due to the higher field in the closed holes of the THGEM, a higher gain can be reached for the same voltage. A Micro-RWELL (μ -RWELL) is a similar architecture with ~ 7 times smaller pitch (distance between holes). These options provide a better spark resistance and could allow to cover large areas for a lower cost.

A Micro-Pixel Gas Chamber (μ -PIC) is a PCB with anode strips on one side and orthogonal cathode strips on the other. The cathode has a resistive coating and a regular pattern of uncoated regions with anode "dots" penetrating the PCB at the centers.

1.4 Orthogonal Fields TPC at IEAP CTU

At IEAP CTU, we are going to use six identical atypical TPCs with inhomogeneous toroidal magnetic field **orthogonal** to the electric field (details below), hereafter referred to as Orthogonal Fields TPC (OFTPC). It has the shape of isosceles trapezoidal prism 16 centimeters high with triple-GEM readout on one of its bases. Dimensions of the OFTPC are discussed in detail in section 1.4.2 below. Throughout this thesis, we assume a uniform electric field along the z axis with $E_z = -400 \text{ V/cm}$. Isn't the field affected by the MWPCs? Eventually a sim-

ulation will be needed. Measured particles enter the OFTPC through a window after crossing the MWPC. Gas mixture used in the detector (70/30) and its effect – some graph with the mixture, reasons for the choice. Add a figure of the real TPC. More about the design choices.

1.4.1 Motivation and Associated Challenges

The reasons for the unusual field layout are mostly cost related:

- a) we use permanent magnets instead of a solenoid and parallel fields are difficult to accomplish this way,
- b) granularity of the TPC readout is limited in order to fit one SAMPA/SRS hybrid in each sector – parallel fields would bend the trajectories parallel to the readout requiring more pads and different architecture.

In this thesis, we will show that such a setup can reach a similar energy resolution as common cylindrical TPCs while reducing the overall cost.

The layout introduces two complications to the track reconstruction – the trajectory in inhomogeneous field is not circular and the drift is distorted by the magnetic field as shown in the Equation 1.1(in our case $\omega\tau \approx 0.08$ for 0.3 T assuming $\mu \approx 0.25$ T⁻¹, varies inside the detector). We will deal with these effects in the upcoming chapters.

The diffusion in such setup is larger since parallel orientation reduces diffusion by curling the electrons in the x - y direction (see Equation 1.8), but for our relatively weak magnetic field and short drift distance, the difference is negligible.

1.4.2 Coordinate Systems and Dimensions

In order to describe events in our detector, we use three distinct spaces: the detector space \mathcal{D} , the readout space \mathcal{R} and the pad space \mathcal{P} (different spaces that describe different things and each has their own coordinate system, so maybe rename the section somehow?). Each space is later used to represent ionization electrons at different stages of the detection process: their creation in the gas, their final position when hitting the readout plane, and finally their representation in the discrete pad space.

Detector Space

The detector space \mathcal{D} represents the physical space of our detector. We describe it using Cartesian coordinates (x, y, z) . The z -axis is the detector's axis of symmetry, with its negative direction aligned with the proton beam. The origin $(0, 0, 0)$ is located at the center of the irradiated target. The positive x -axis passes through the center of one the OFTPCs along the intersection of its two planes of symmetry. The y -axis is then chosen to maintain a right-handed coordinate system.

Since the detector has a hexagonal symmetry, we use only one of its sectors in this work – the first sector $\mathcal{D}_1 \subset \mathcal{D}$ which is defined by the condition:

$$(x, y, z) \in \mathcal{D}_1 \Leftrightarrow |y| \leq x \tan \frac{\pi}{6}. \quad (1.9)$$

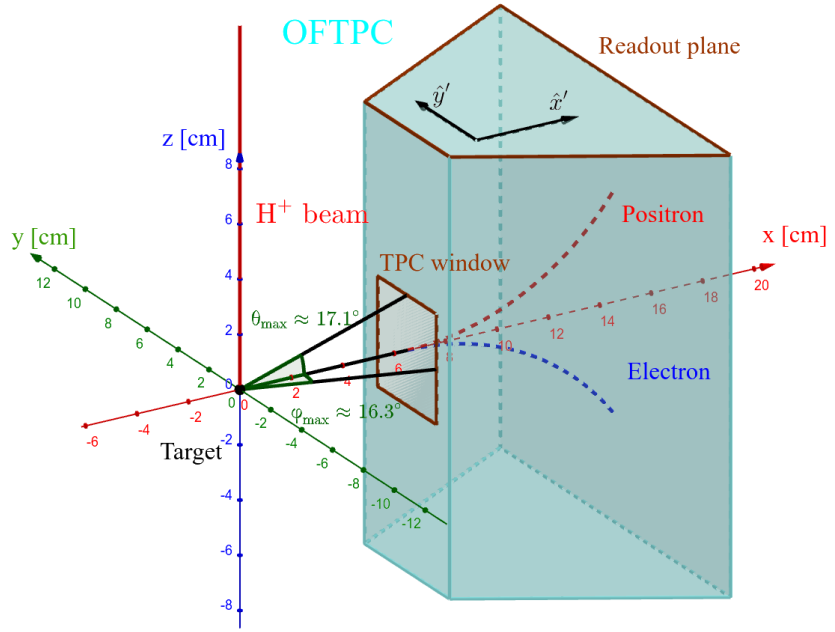


Figure 1.12: Schematics of the first sector OFTPC with detector space coordinates.

490 Simulations in this sector can be applied to all sectors by rotating the coordinates
 491 accordingly. The volume of the OFTPC in this sector, which has the shape of
 492 a trapezoidal prism, has these boundaries:

$$x \in [x_{\min}, x_{\max}] = [6.51, 14.61] \text{ cm}, \quad (1.10)$$

$$z \in [z_{\min}, z_{\max}] = [-8, 8] \text{ cm}, \quad (1.11)$$

$$y_{\max}(x_{\min}) = -y_{\min}(x_{\min}) = 2.75 \text{ cm}, \quad (1.12)$$

$$y_{\max}(x_{\max}) = -y_{\min}(x_{\max}) = 7.45 \text{ cm}, \quad (1.13)$$

493 where $y_{\max}(x)$ is the maximal value of the y -coordinate for a given x . The read-
 494 out is located at $z = 8$ cm; for some purposes, we also define the distance to
 495 the readout $d_r = 8 \text{ cm} - z$ as an alternative to the z -coordinate. **Keeping this**
 496 **paragraph as it is because the OFTPC volume is distinct from the first sector**
 497 **and some parts of this thesis use the space beyond this volume.** The OFTPC
 498 window has width 3.8 cm and height 4.0 cm.

499 We also use spherical coordinates (r, θ, φ) with the elevation angle θ measured
 500 relative to the xy plane. Angles θ and φ are useful when describing the direction
 501 of e^+/e^- tracks. Their maximal values considered for the initial direction in
 502 simulations are $\theta_{\max} \approx 17.1^\circ$ and $\varphi_{\max} \approx 16.3^\circ$ as shown in Fig. 1.12.

503 Readout Space

504 The readout space \mathcal{R} represents the drift time and final positions of ionization
 505 electrons as measured by an ideal continuous readout. We describe it using
 506 coordinates (x', y', t) , where x' and y' correspond to the detector coordinates at
 507 the readout plane ($z = 8$ cm).

508 Currently not entirely sure how to put this into a figure since only x' and
 509 y' correspond to the detector coordinates, it will make more sense when

510 **visualizing the map.** The drift time t is approximately proportional to d_r .

511 Pad Space

512 The pad space \mathcal{P} represents the time bin and pad number of ionization electrons
513 as measured by an ideal discrete readout:

$$\mathcal{P} = \{(n_{\text{pad}}, n_t) \in \mathbb{N}^2 \mid n_{\text{pad}} \leq 128\}. \quad (1.14)$$

514 **Rewrite to reflect this:** Technically both values can be zero as defined in the
515 code (max channel 127). It is not really a subspace of \mathcal{R} but there is a mapping
516 from \mathcal{R} to \mathcal{P} . It is a discretization of a part of \mathcal{R} , the mapping can be adjusted
517 depending on the simulation. If we assume uniform electric field there will be
518 gaps, we don't use gaps in the reconstruction since the electrons should be pulled
519 towards the pads.

520 The readout of the OFTPC will consist (is the design final?) of 128 rectangular
521 pads arranged in a staggered pattern. Parameters of the pad layout are shown
522 in Fig. 1.13. The bottom left corner of n -th pad has coordinates $(x_{1,n}, y_{1,n})$, the
523 top right $(x_{2,n}, y_{2,n})$ and its center has coordinates $(x_{c,n}, y_{c,n})$. The gap between
524 neighboring pads is $g = 0.08$ cm. Time will be read out in discrete bins of size
525 $t_{\text{bin}} = 100$ ns (details?). Could also describe pad-related functions.

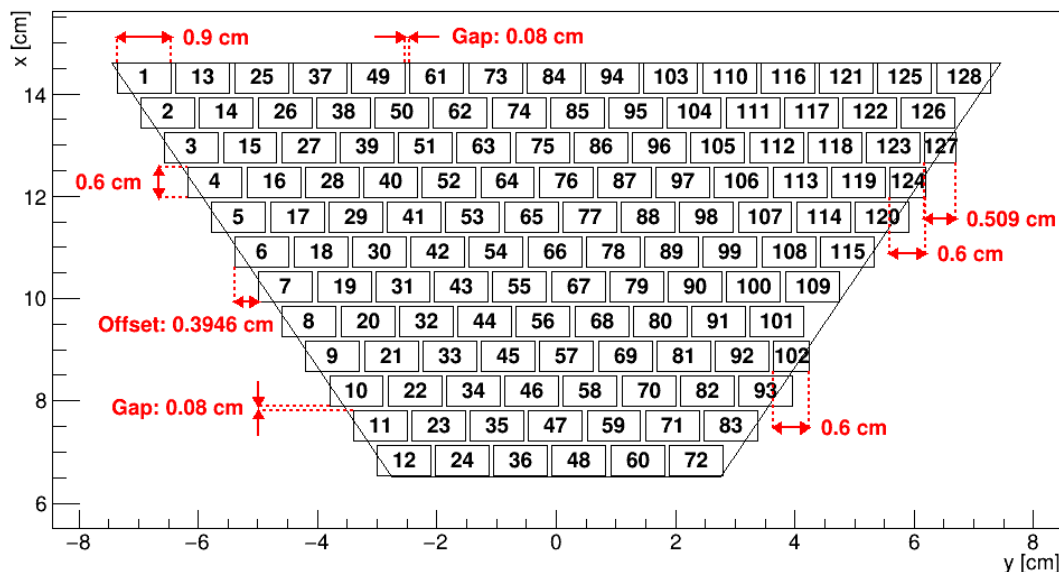
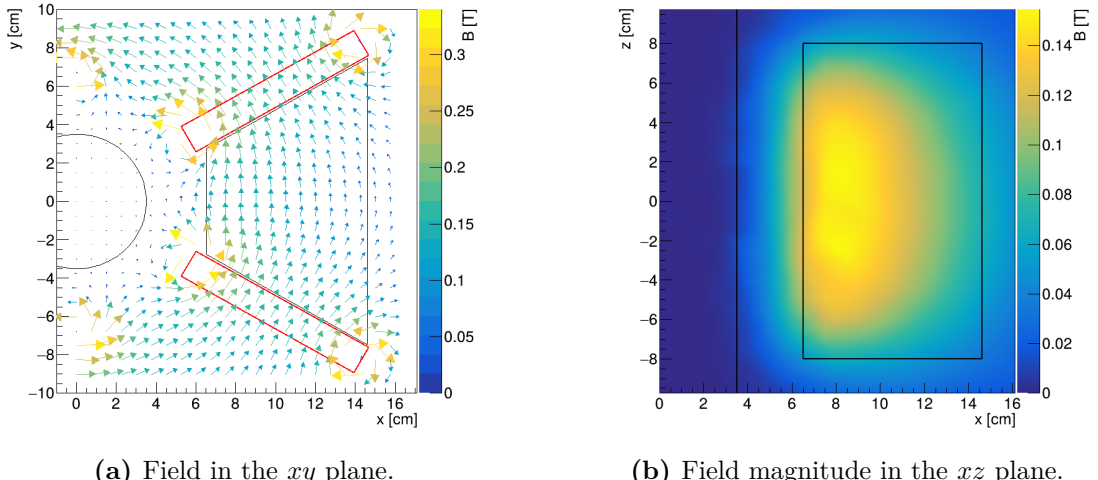


Figure 1.13: Pad layout of the OFTPC and its parameters. Pads 102, 124 and 127 are irregular, the rest has the same dimensions.

526 1.4.3 Magnetic Field Simulation

527 The magnetic field inside our detector is produced by six permanent magnets. It
528 was simulated using Ansys Maxwell (citation) which gives us values on a regular
529 grid. More details, vacuum tube, magnets (homogeneous?, density?). Visualization
530 of the magnetic field is shown in Fig. 1.14. Whenever we need to work with
531 values outside this grid, we use trilinear interpolation described below.



(a) Field in the xy plane.

(b) Field magnitude in the xz plane.

Figure 1.14: Magnetic field simulation results. The OFTPC volume and the vacuum tube are marked with black lines, the magnets are marked with red lines. **The coordinates of the magnets from the CAD drawing seem to be 9/10 of the ones from the magnetic simulation (fixed, the magnetic simulation parameters are off).**

532 Trilinear Interpolation

533 Trilinear interpolation is a 3D generalization of linear interpolation³. It can be
 534 used to interpolate a function whose values are known on a regular grid with
 535 rectangular prism cells. We use this simple method for interpolating the magnetic
 536 field, and it is later used in Section 3.2.2 to interpolate the Ionization Electron
 537 Map, a key component of our track reconstruction algorithm. In both cases, we
 538 use a regular cubic grid (apparently it is also called a Cartesian grid).

539 Let us consider a cell of our regular grid (a cube) with an edge of length a
 540 containing the point $\mathbf{C} = (x, y, z)$ where we want to interpolate a function
 541 $f: \mathbb{R}^3 \rightarrow \mathbb{R}$. We know the values of this function at the vertices of the cell
 542 $\mathbf{C}_{ijk} = (x_0 + ia, y_0 + ja, z_0 + ka)$, where $\mathbf{C}_{000} = (x_0, y_0, z_0)$ is the origin of the
 543 cell (is that clear?), and $i, j, k \in \{0, 1\}$ are indices. We also define the points $\mathbf{C}_{ij} =$
 544 $= (x, y_0 + ia, z_0 + ja)$ and $\mathbf{C}_i = (x, y, z_0 + ia)$. Then the interpolated value $\hat{f}(\mathbf{C})$
 545 can be calculated as a composition of three linear interpolations (see Fig. 1.15):

$$\hat{f}(\mathbf{C}_{ij}) = (1 - x_d) f(\mathbf{C}_{0ij}) + x_d f(\mathbf{C}_{1ij}), \quad (1.15)$$

$$\hat{f}(\mathbf{C}_i) = (1 - y_d) \hat{f}(\mathbf{C}_{0i}) + y_d \hat{f}(\mathbf{C}_{1i}), \quad (1.16)$$

$$\hat{f}(\mathbf{C}) = (1 - z_d) \hat{f}(\mathbf{C}_0) + z_d \hat{f}(\mathbf{C}_1), \quad (1.17)$$

546 where x_d , y_d , and z_d are given as follows:

$$x_d = \frac{x - x_0}{a}, \quad y_d = \frac{y - y_0}{a}, \quad z_d = \frac{z - z_0}{a}. \quad (1.18)$$

³Linear interpolation in point $x \in (x_1, x_2)$ of a function $f: \mathbb{R} \rightarrow \mathbb{R}$ known in points $x_1 < x_2$ is the convex combination $\hat{f}(x) = (1 - x_d)f(x_1) + x_d f(x_2)$, where $x_d = \frac{x - x_1}{x_2 - x_1} \in (0, 1)$.

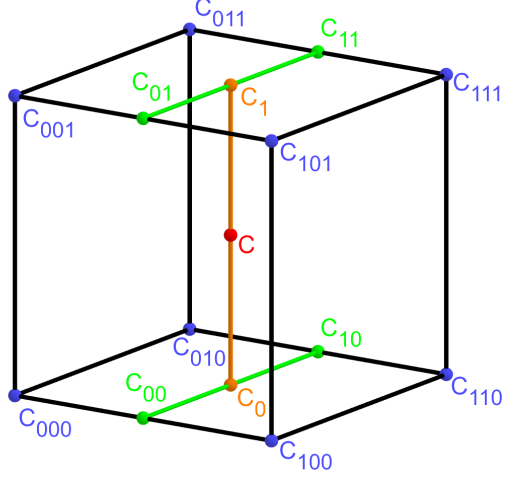


Figure 1.15: Visualization of trilinear interpolation as a composition of linear interpolations (inspired by [42]). We want to interpolate the value in the red point \mathbf{C} . First we interpolate between the four pairs of blue points sharing the last two indices along the x -axis (Eq. 1.15), then between the two pairs of the resulting green points along the y -axis (Eq. 1.16) and finally between the two resulting orange points along the z -axis to get the final red value (Eq. 1.17).

547 We can also write

$$\hat{f}(\mathbf{C}) = \sum_{i,j,k \in \{0,1\}} t_x^i t_y^j t_z^k f(\mathbf{C}_{ijk}), \quad (1.19)$$

$$t_\alpha \stackrel{\text{def}}{=} \begin{pmatrix} t_\alpha^0 \\ t_\alpha^1 \end{pmatrix} = \begin{pmatrix} 1 - \alpha_d \\ \alpha_d \end{pmatrix}, \quad (1.20)$$

548 where $\alpha \in \{x, y, z\}$ is an index. This gives a nice geometric interpretation to the
549 trilinear interpolation as shown in Fig. 1.16. From this form and the figure, it is
550 apparent that the final interpolated value does not depend on the order of axes
551 along which we perform linear interpolations (see Fig. 1.15). Furthermore, we
552 can write $\hat{f}(\mathbf{C})$ as a polynomial:

$$\hat{f}(\mathbf{C}) = \sum_{\alpha, \beta, \gamma \in \{0,1\}} \sum_{i=0}^{\alpha} \sum_{j=0}^{\beta} \sum_{k=0}^{\gamma} (-1)^{(\alpha-i)+(\beta-j)+(\gamma-k)} f(\mathbf{C}_{ijk}) x_d^\alpha y_d^\beta z_d^\gamma. \quad (1.21)$$

553 We take advantage of this form when generalizing trilinear interpolation to irreg-
554 ular grid in section 3.2.3.

555 Maybe a citation here, although I am not sure it is necessary since it could
556 be considered common knowledge. The last two equations are my own (but I'm
557 not sure that's worth mentioning unless there's a citation).

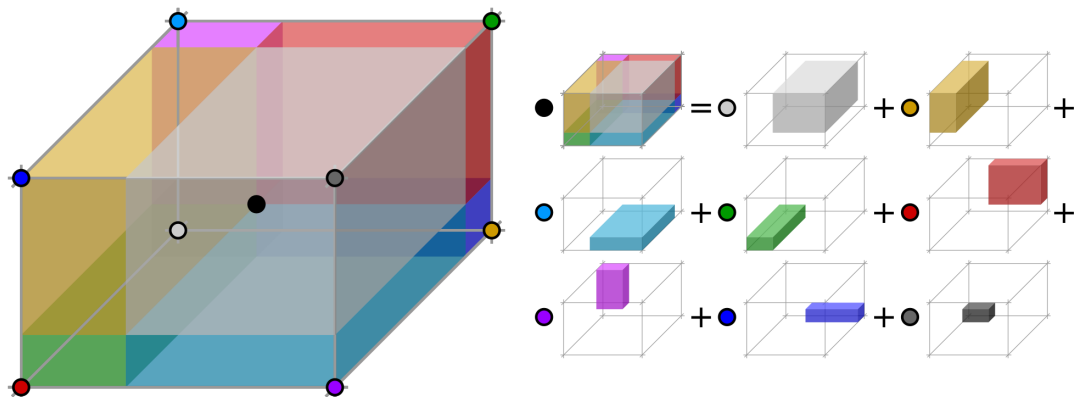


Figure 1.16: Geometric interpretation of trilinear interpolation as expressed in Equation 1.19. The colored dots represent the values in given points and the colored boxes represent the volume in the opposite corner by which the corresponding values are multiplied. The black dot represents the interpolated value which is multiplied by the entire volume [43].

2. Track Simulation

In order to develop and test the reconstruction algorithm, electron and positron tracks are simulated inside the first detector sector \mathcal{D}_1 (see Section 1.4.2) with different initial parameters (origin, initial direction and kinetic energy). Two approaches are currently used to simulate tracks, each of them for different purpose.

The **Microscopic Simulation** uses the Garfield++ toolkit [1]. Within this toolkit:

- a) Magboltz, since it is mentioned later. Or maybe just class MediumMagboltz with the collision rates?
- b) the High Energy Electro-Dynamics (HEED) program [44] is used to simulate the primary particle,
- c) the class *AvalancheMicroscopic* to simulate the drift of secondary electrons created by ionization in the gas.

This is the most precise and time-consuming simulation used; our current goal is to be able to successfully reconstruct its results and determine our best-case energy resolution.

The **Runge-Kutta Simulation** uses the 4th order Runge-Kutta numerical integration (add citation for Runge-Kutta) to simulate the trajectory of the primary particle in the electromagnetic field inside the detector. It is relatively fast since it does not simulate the secondary particles. It is used as part of our reconstruction algorithm and for testing some parts of the reconstruction.

All of these simulations require the knowledge of the electromagnetic field (both **E** and **B**) inside the detector. A uniform electric field of $400 \text{ V}\cdot\text{cm}^{-1}$ is assumed. The magnetic field was simulated in Maxwell (see Section 1.4.3). add citation

Single track in positive x direction or initial parameter randomization. Importance of gas composition, used gas compositions.

2.1 Microscopic Simulation

The microscopic simulation, the most detailed simulation used in this work, is performed using the Garfield++ toolkit [1].

The electron transport properties are simulated using the program Magboltz (add citation), (details?). Two different gas mixtures were compared – 90:10 and 70:30 Ar:CO₂. The second mixture will be used in our detector (this was probably known a priori, but the first tests that I started with used 90/10, so maybe just note that the results justify the fact so far). The temperature is set to 20 °C, the pressure is atmospheric.

The primary track is simulated using the program HEED, which is an implementation of the photo-absorption ionization model [44] (see the reference, moved it to the end of sentence). This program provides the parameters of ionizing collisions. HEED can also be used to simulate the transport of delta electrons; we do not account for these in the current simulation (but plan to include them in the future – maybe mention only in the conclusion/future section). The photons created in the atomic relaxation cascade (fluorescence reabsorption, related to the spread of avalanches in GM det.?) are also not simulated.

602 Finally, we use the microscopic tracking provided by the class *AvalancheMicroscopic* in Garfield++ to simulate the drift of the ionization electrons. Each
 603 electron is followed from collision to collision using the equation of motion and
 604 the collision rates calculated by Magboltz (how fast is this? maybe it slows down
 605 the simulation when spreading it across multiple jobs?).

606 Add more detailed and better description of HEED, and microscopic tracking
 607 (each their own subsection?). Could also mention Monte Carlo (requires gas file
 608 generation - Magboltz) and Runge-Kutta simulation implemented in Garfield,
 609 why we don't use them (another subsection? rename the section to Garfield++
 610 simulation and mention all relevant parts?).

612 2.1.1 First testing track

613 The first electron track simulated for testing purposes was chosen to have a special
 614 set of parameters:

- 615 • the starting point of the track is the origin of the coordinate system,
- 616 • the initial direction is along the positive x -axis,
- 617 • the momentum is 8 MeV/c (the kinetic energy is 7.505 MeV).

618 Such a track moves in the XZ plane in the toroidal magnetic field of the detector,
 619 because the particle's velocity vector is always perpendicular to the field. At first,
 620 we simulated such a track in 90:10 Ar:CO₂ gas mixture, later we added a simu-
 621 lation in 70:30 Ar:CO₂, which we plan to use in our detector. The comparison of
 622 both simulations is in Fig. 2.1. In the first tests, the initial energy of produced
 623 ionization was set to 0.1 eV instead of the value generated by HEED.

624 2.1.2 Grid-like testing sample

625 In order to test all steps of the reconstruction, a sample of tracks with a grid-like
 626 distribution of parameters was generated on MetaCentrum. Five sets of 9702
 627 tracks were generated with every combination of these parameters:

- 628 • electron and positron tracks,
- 629 • 11 different kinetic energies $E_{\text{kin}} \in [3, 13]$ MeV,
- 630 • 21 different azimuth angles $\varphi \in [-16.3^\circ, 16.3^\circ]$ and
- 631 • 21 different elevation angles $\theta \in [-17.1^\circ, 17.1^\circ]$.

632 A visualization of a set of e^+/e^- tracks with the same kinetic energy is shown in
 633 Fig. 2.2 (plotting actual HEED tracks using ROOT should be also possible (but
 634 hard to make look good?)). In the 70:30 Ar:CO₂ atmosphere, each track takes
 635 5-30 CPU hours to simulate. Every tenth point on the drift line was stored, the
 636 whole sample has 3.1 terabytes (or 1.4 gigabytes without drift lines).

637 2.2 Runge-Kutta Simulation

638 The Runge-Kutta simulation in this work uses the Runge-Kutta 4th order (RK4)
 639 method to numerically integrate the equation of motion of a relativistic charged
 640 particle in an electromagnetic field. Given a system of first order differential
 641 equations

$$\frac{dy}{dt} = f(t, y(t)) \quad (2.1)$$

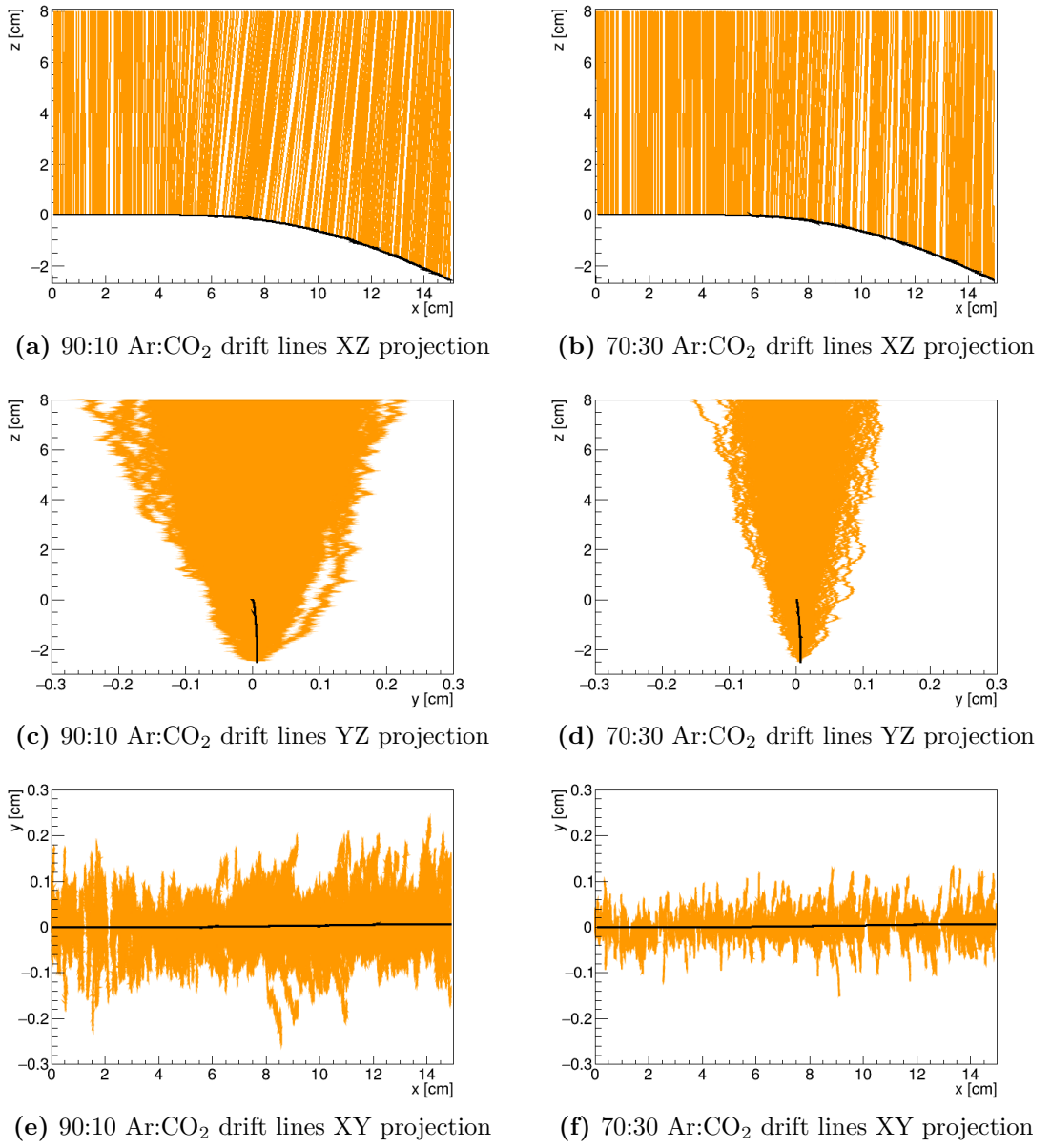


Figure 2.1: Comparison of drift lines for two different gas mixtures 90:10 and 70:30 Ar:CO₂. The electron track is marked in black, the drift lines of the ionization electrons are marked in orange. In this example, we assume a larger OFTPC volume with readout at $z = 8$ cm.

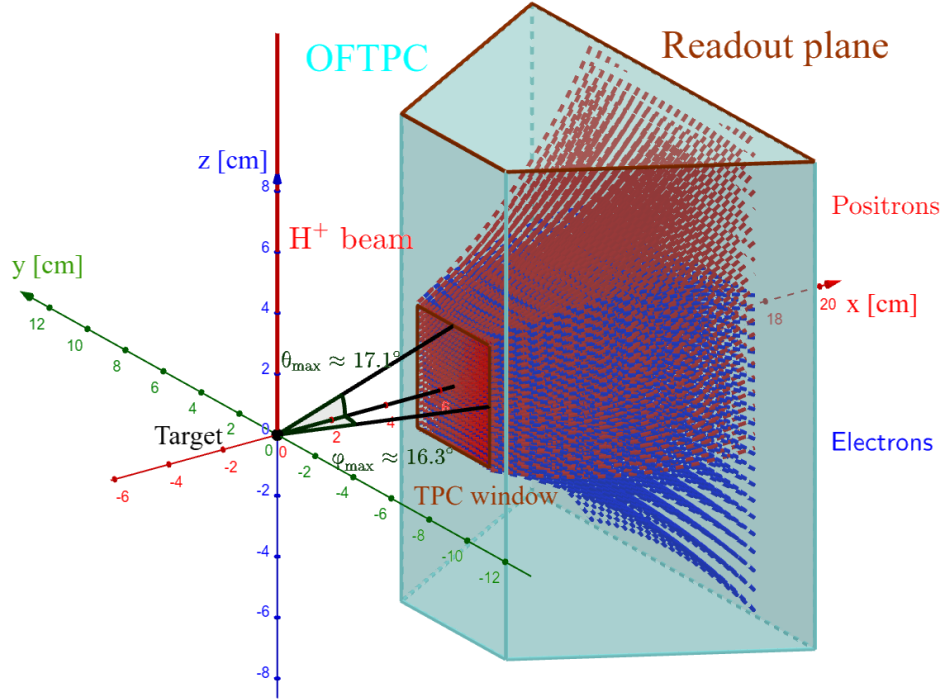


Figure 2.2: A visualization of a set of tracks from the grid-like testing sample with the same kinetic energy.

642 with an initial condition

$$\mathbf{y}(t_0) = \mathbf{y}_0, \quad (2.2)$$

643 we iteratively compute the estimate $\mathbf{y}_n = \mathbf{y}(t_n) = \mathbf{y}(t_0 + nh)$ as follows (citation?
644 common knowledge?):

$$\mathbf{k}_1 = \mathbf{f}(t_n, \mathbf{y}_n), \quad (2.3)$$

$$\mathbf{k}_2 = \mathbf{f}\left(t_n + \frac{h}{2}, \mathbf{y}_n + \frac{h\mathbf{k}_1}{2}\right), \quad (2.4)$$

$$\mathbf{k}_3 = \mathbf{f}\left(t_n + \frac{h}{2}, \mathbf{y}_n + \frac{h\mathbf{k}_2}{2}\right), \quad (2.5)$$

$$\mathbf{k}_4 = \mathbf{f}(t_n + h, \mathbf{y}_n + h\mathbf{k}_3), \quad (2.6)$$

645

$$\mathbf{y}_{n+1} = \mathbf{y}_n + \frac{1}{6}(\mathbf{k}_1 + 2\mathbf{k}_2 + 2\mathbf{k}_3 + \mathbf{k}_4). \quad (2.7)$$

646 Alternate forms (infinitely many) possible, accuracy vs computational cost. Runge-
647 Kutta-Fehlberg with adaptive step size also possible, can potentially save some
648 computation time especially in rapidly changing field (so maybe not in this case).

649 In our case, we want to integrate the equation of motion, given by the rela-
650 tivistic Lorentz force:

$$F_L^\mu = m \frac{du^\mu}{d\tau} = q F^{\mu\nu} u_\nu, \quad (2.8)$$

651 where the Einstein summation convention is used, m is the mass of the particle,
652 q is its charge, u^μ is its four-velocity, τ is the proper time (i.e., time in the particle's
653 frame of reference) and $F^{\mu\nu}$ is the electromagnetic tensor at given coordinates x^μ

654 (we consider it to be time-independent in our detector). Given the electric $\mathbf{E} =$
 655 $= (E_x, E_y, E_z)$ and the magnetic field $\mathbf{B} = (B_x, B_y, B_z)$ and using the metric
 656 signature $(+, -, -, -)$, the equation expands to

$$\frac{d}{d\tau} \begin{pmatrix} \gamma c \\ \gamma v_x \\ \gamma v_y \\ \gamma v_z \end{pmatrix} = \frac{q}{m} \begin{pmatrix} 0 & -\frac{E_x}{c} & -\frac{E_y}{c} & -\frac{E_z}{c} \\ \frac{E_x}{c} & 0 & -B_z & B_y \\ \frac{E_y}{c} & B_z & 0 & -B_x \\ \frac{E_z}{c} & -B_y & B_x & 0 \end{pmatrix} \begin{pmatrix} \gamma c \\ \gamma v_x \\ \gamma v_y \\ \gamma v_z \end{pmatrix}, \quad (2.9)$$

657 where c is the speed of light in vacuum, $\mathbf{v} = (v_x, v_y, v_z)$ is the particle's velocity
 658 and $\gamma = (1 - \frac{v^2}{c^2})^{-\frac{1}{2}}$ is the Lorentz factor (wrong magnetic field sign in the
 659 implementation???). Together with the equation

$$\frac{d}{d\tau} \begin{pmatrix} ct \\ x \\ y \\ z \end{pmatrix} = \begin{pmatrix} \gamma c \\ \gamma v_x \\ \gamma v_y \\ \gamma v_z \end{pmatrix} = u^\mu, \quad (2.10)$$

660 we get a system of eight first order differential equations for x^μ and u^μ , which
 661 we can integrate using the Runge-Kutta method described above. As a result of
 662 this integration, we get the position $\mathbf{x}(\tau_n)$, the velocity $\mathbf{v}(\tau_n)$ and the detector
 663 time $t(\tau_n)$ for every proper time $\tau_n = n\tau_{\text{step}}$. Integrating using the proper time
 664 means that the step size in t gets larger by the gamma factor $\frac{dt}{d\tau} = \gamma$ (maybe
 665 change it and integrate the detector time or adjust the step size accordingly). The
 666 only difference is in the step size (because t gets also calculated as it is among the
 667 8 variables). It might be even better to adjust the step size using approximate
 668 distance traveled. As initial conditions, we use the origin of the track
 669 (x_0, y_0, z_0) , the initial velocity direction vector $\mathbf{n} = (\cos \varphi \cos \theta, \sin \varphi \cos \theta, \sin \theta)$
 670 and the kinetic energy E_{kin} (initial parameters of the simulation (fit is in chapter
 671 4)), we then compute γ and $\|\mathbf{v}\|$:

$$\gamma = 1 + \frac{E_{\text{kin}}}{E_0}, \quad (2.11)$$

$$\|\mathbf{v}\| = c\sqrt{1 - \gamma^{-2}}. \quad (2.12)$$

672 2.2.1 Testing sample

673 Example of RK simulation – first testing track, randomized sample of 100000
 674 tracks (could also move them to circle 3D fit).

675 In order to test the simulation and reconstruction, a sample of 100 000 tracks
 676 with randomized parameters was generated:

- 677 the Runge-Kutta step was set to 0.1 ns (proper time, which wouldn't be a
 678 problem but this way the "spatial" step depends on energy),
- 679 the kinetic energy of the particle $E_{\text{kin}} \in [4, 12]$ MeV,
- 680 the starting point of the track is a random point in the OFTPC window,

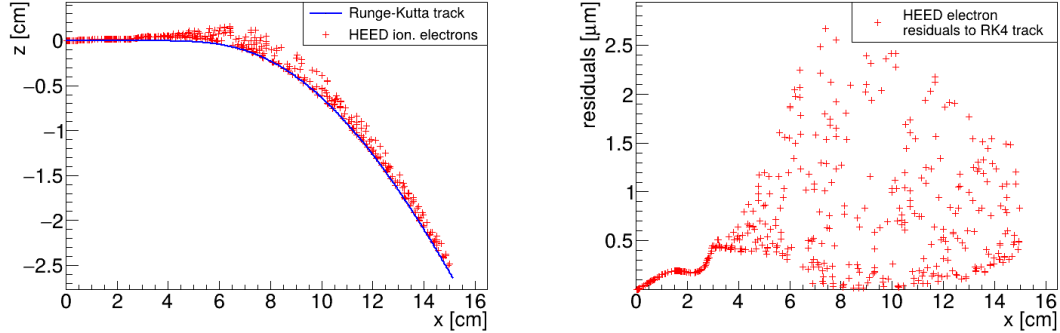


Figure 2.3: A comparison of the HEED track from the microscopic simulation in Section 2.1.1 with a Runge-Kutta track with the same initial parameters and $\tau_{\text{step}} = 0.1 \text{ ps}$ (reducing the step further doesn't make a visible difference). In the view of the tracks on the left, the distance of the HEED ionization electrons from the RK4 track is exaggerated $1000\times$. On the right, the dependence of the HEED electrons residuals (i.e., their shortest distance to the RK4 track) on their z -coordinate is shown. The images look the same even for $100,000\times$ smaller step, so the residuals are a result of something that HEED does (maybe a different interpolation technique for the magnetic field? the pattern looks similar for two different tracks so it can't be scattering).

When exaggerating, the HEED ionization electrons are moved away along the shortest line connecting them to the RK4 track. The computation of this distance is described in Section 4.3.

- 681 • the initial direction is given by the line connecting a random point on the
- 682 target¹ (a disc with 1 mm radius in the YZ plane).
- 683 Since the Runge-Kutta simulation is quite fast², it can be run locally on any
- 684 computer. Add a figure with simulated tracks (sample). An example Runge-
- 685 Kutta track is compared with the corresponding microscopic track in Fig. 2.3.

¹To generate a random point on the target, we generate a random angle α and a random square of the distance from origin r^2 to get a uniform distribution.

²One track with $\tau_{\text{step}} = 0.1 \text{ ps}$ takes less than one millisecond to simulate.

686 3. Track Reconstruction

687 As the first step of the reconstruction algorithm, we reconstruct the track of
688 a primary particle – either an electron or a positron. Then, using this information,
689 we determine the energy of the particle (Section 4).

690 The **Reconstruction Assuming Steady Drift (RASD)** uses the stan-
691 dard TPC approach. With parallel fields, the drift inside a uniform electric field
692 remains undistorted (as shown in Equation 1.1). Therefore, we only need to re-
693 construct the z -coordinate from the drift time using the known drift velocity. We
694 also assume that the readout coordinates (x', y', t) are known exactly, neglecting
695 the pads and time binning.

696 Reconstruction using an **Ionization Electron Map** (from now on referred
697 to as *the map*) uses a simulation of the drift of secondary (ionization) electrons
698 within the detector volume. This simulation can then be used to interpolate the
699 initial position of the secondary electrons. In the first iteration of this method
700 the readout is assumed to be continuous.

701 We present two algorithms using the map for reconstruction. The first one uses
702 a gradient descent algorithm along with trilinear interpolation (see Section 1.4.3)
703 of the map. The second method uses interpolation on the irregular inverse grid
704 with a polynomial.

705 The **Discrete Reconstruction** uses the map; instead of reconstructing the
706 exact position of each electron, we reconstruct the center of each hit pad together
707 with the time corresponding to the midpoint of the time bin. The electron count
708 in each TPC bin (consisting of the pad and the time bin) serves as an idealized
709 collected charge, which is then used as a weight in the energy reconstruction fit.

710 3.1 Reconstruction Assuming Steady Drift

711 As the first step, we tried to reconstruct a simulated electron track with a special
712 set of initial parameters, described in detail in Section 2.1.1. The starting point
713 is given by the origin of our coordinate system and its initial direction is given by
714 the positive x -axis. This means the magnetic field of our detector is perpendicular
715 to the momentum of the particle at all times, and we can reduce the problem to
716 two-dimensional space.

717 For the reconstruction, we decided to use the common method used in a stan-
718 dard TPC (*similar to?, cite some source(s)!*). We call this method *Reconstruction*
719 *Assuming Steady Drift (RASD)*. This will allow us to explore the significance of
720 the atypical behavior in our OFTPC. Additionally, we assume the readout is con-
721 tinuous to further simplify the problem. In this approximation, we reconstruct
722 the initial position of each ionization electron.

723 The reconstruction is then defined by the following relations between the
724 coordinates of the detector space and the readout space (see Section 1.4.2):

$$x = x', \tag{3.1}$$

$$y = y', \tag{3.2}$$

$$z = 8 \text{ cm} - d_r = 8 \text{ cm} - v_d t, \tag{3.3}$$

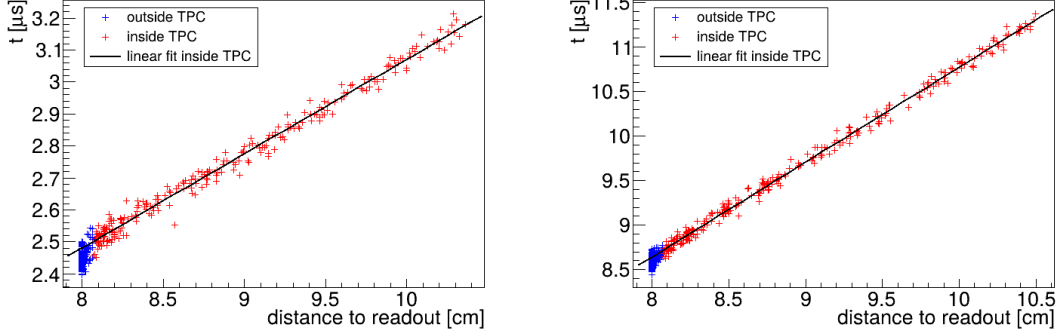


Figure 3.1: Linear fit of the drift time t dependence on the distance to the readout $d_r = 8 \text{ cm} - z$ for the ionization electrons in 90:10 (left) and 70:30 (right) Ar:CO₂ gas composition. Only electrons inside the TPC (red) are fitted. The parameters are $v_d = 3.39 \text{ cm}/\mu\text{s}$, $d_0 = -0.41 \text{ cm}$ for 90:10, and $v_d = 0.939 \text{ cm}/\mu\text{s}$, $d_0 = -0.11 \text{ cm}$ for 70:30 Ar:CO₂.

where d_r is the distance to the readout, and v_d is the drift velocity of electrons in the given gas mixture. At a phenomenological level, this velocity can be considered as a function of the electric field \mathbf{E} and the magnetic field \mathbf{B} as shown in Equation 1.1. The Garfield++ toolkit uses this fact to accelerate their drift simulation with non-microscopic approaches (could mention in the simulation chapter). Since we assume a uniform electric field in the detector and in this approximation we want to neglect the effect of our unusual magnetic field, we consider the drift velocity constant. We can estimate the drift velocity by fitting the dependence $d_r(t)$ of ionization electrons from a simulated track with a linear function:

$$d_r(t) = v_d t + d_0. \quad (3.4)$$

The fit was applied on two tracks with different gas composition, the result is in Fig. 3.1. Compare with real drift velocities – a good indication of the tilt of drift lines. The obtained parameters are then used for the reconstruction shown in Fig. 3.2. From the residuals shown in Fig. 3.3, we can see that this reconstruction algorithm leads to significant deviations from the simulated track (up to 1.1 cm for 90:10, and up to 0.3 cm for 70:30 Ar:CO₂), especially in the faster gas mixture 90:10 (as expected – for a higher mean time between collisions in Equation 1.1, the effect of the magnetic field is bigger). These deviations are mainly caused by the shift in the x -coordinate due to the tilt of the drift lines in magnetic field. In order to account for this, we need to develop a better algorithm. There is also a small irregularity in the z -coordinate but it is comparable with the diffusion. We can/will also later show that this has a significant effect on the reconstructed energy.

3.2 Ionization Electron Map

Inside an OFTPC (\exists more than one, also considering it a general concept rather than the specific OFTPC used at this experiment), the drift of the ionization electrons is significantly affected by its magnetic field as shown in Equation 1.1, see also Fig. 2.1. We need to take this into account for accurate reconstruction (should be easy to run the reconstruction without the map and show how

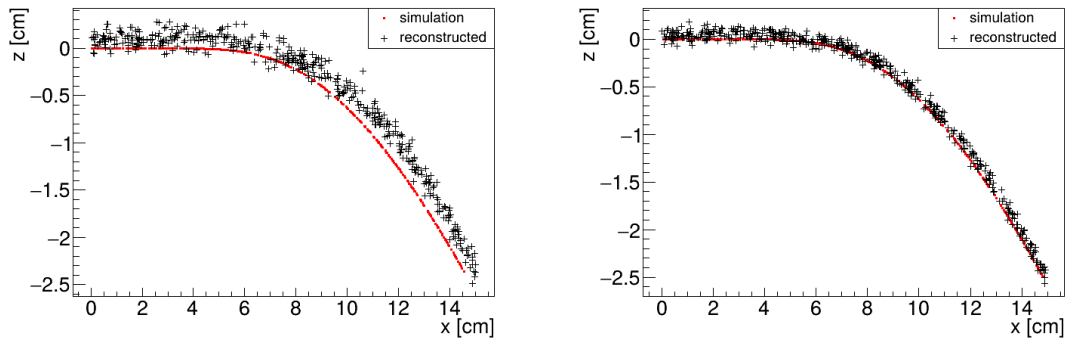


Figure 3.2: Reconstruction (black) of the starting position of ionization electrons (red) using parameters obtained from the fit (Fig. 3.1). Two gas compositions 90:10 (left) and 70:30 Ar:CO₂ (right) are compared.

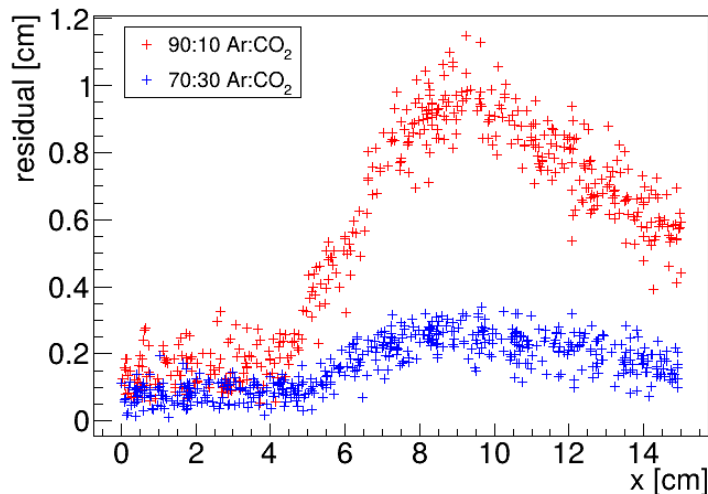
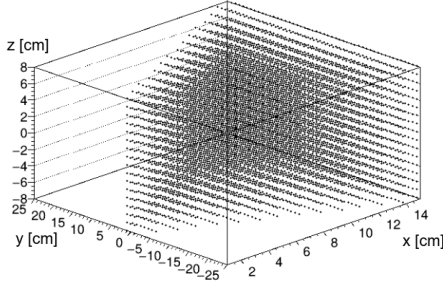


Figure 3.3: Comparison of residuals (i.e., the distance from the reconstructed point to the simulated ionization electron starting point) dependence on x for two gas mixtures 90:10 (red) and 70:30 Ar:CO₂ (blue).

Detector space \mathcal{D}



Readout space \mathcal{R}

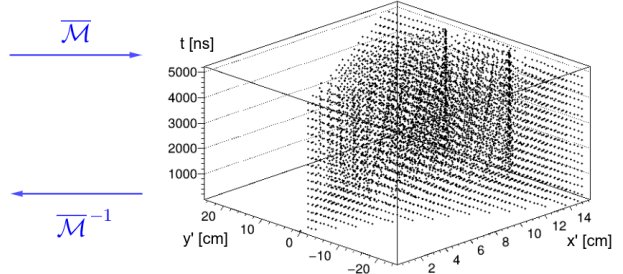


Figure 3.4: A 3D visualization of the mapping of means $\bar{\mathcal{M}}$ for the 90:10 Ar:CO₂ gas. A regular grid \mathbb{G} with $l = 1$ cm in the detector space is mapped to an irregular grid $\mathbb{G}^{-1} \equiv \bar{\mathcal{M}}(\mathbb{G})$ in the readout space.

much it improves the results). In the first approximation, we assume a continuous readout (i.e., we neglect the anode segmentation into pads). We can then reconstruct the original position of each ionization electron using its readout coordinates. For this purpose, we use the ionization electron map.

The ionization electron map represents a mapping from the detector space to the readout space (see Section 1.4.2). It tells us what readout coordinates (x', y', t) we can expect on average for an ionization electron created at the detector coordinates (x, y, z) . More precisely, it is a mapping to the distributions on the readout space; we can simplify this as only the means $\bar{\mathcal{M}}$ and the covariance matrices \mathcal{M}_{Σ} , assuming Gaussian distribution:

$$\bar{\mathcal{M}}: \mathcal{D} \longrightarrow \mathcal{R}, \quad (x, y, z) \longmapsto \bar{\mathbf{X}}^T \equiv (\bar{x}', \bar{y}', \bar{t}), \quad (3.5)$$

$$\mathcal{M}_{\Sigma}: \mathcal{D} \longrightarrow \mathbb{R}^{3 \times 3}, \quad (x, y, z) \longmapsto \Sigma \equiv \begin{pmatrix} \sigma_{x'}^2 & \text{cov}(x', y') & \text{cov}(x', t) \\ \text{cov}(y', x') & \sigma_{y'}^2 & \text{cov}(y', t) \\ \text{cov}(t, x') & \text{cov}(t, y') & \sigma_t^2 \end{pmatrix}, \quad (3.6)$$

$$\mathcal{M}: \mathcal{D} \longrightarrow D(\mathcal{R}), \quad (x, y, z) \longmapsto N(\mathbf{X}) \equiv \frac{\exp\left(-\frac{1}{2}(\mathbf{X} - \bar{\mathbf{X}})^T \Sigma (\mathbf{X} - \bar{\mathbf{X}})\right)}{\sqrt{(2\pi)^3 |\Sigma|}}. \quad (3.7)$$

To get an approximation of this mapping, we simulate the drift of ionization electrons generated on a regular Cartesian grid $\mathbb{G} \subset \mathcal{D}$ with spacing l inside the volume of our OFTPC¹ (see the visualization in Fig. 3.4). In Fig. 3.5, you can see an example of drift lines from a test of the simulation. After testing runs, two map simulations were made with different gas composition, their parameters are shown in Table 3.1.

In order to get accurate results, we use the microscopic simulation of these electrons described in Section 2.1 (Monte Carlo from *AvalancheMC* was also considered but it doesn't (didn't? CERES used it from MAGBOLTZ???) include magnetic field, we can probably improve this anyway using the fast track simulation with map proposed in the future section). It is also useful to simulate multiple (N) electrons originating from the same position so that we can account for the random fluctuations due to collisions. Using the readout coordinates of

¹The detector walls are not considered and we simulate the drift even outside of the OFTPC which allows us to interpolate even close to the walls

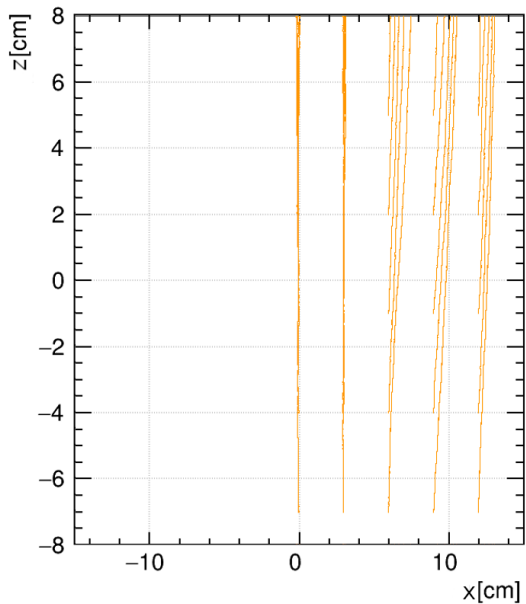


Figure 3.5: A test of the 90:10 Ar:CO₂ map simulation with spacing $l = 1.5$ cm. The resulting drift lines of evenly spaced electrons are displayed in orange.

Table 3.1: Comparison of parameters of two map simulations.

Parameter	90:10 Ar:CO ₂ map	70:30 Ar:CO ₂ map
N	100	100
l	1.0 cm	0.5 cm
z bounds	$[-8, 8]$ cm	$[-8, 8]$ cm
x bounds	$[0, 15]$ cm	$[-1.5, 15.0]$ cm
y bounds	$ y \leq x \cdot \tan \frac{\pi}{3}$	$ y \leq (x + 1.5 \text{ cm}) \cdot \tan \frac{\pi}{6}$
initial energy	0.1 eV	0.1 eV
init. direction	randomized	randomized

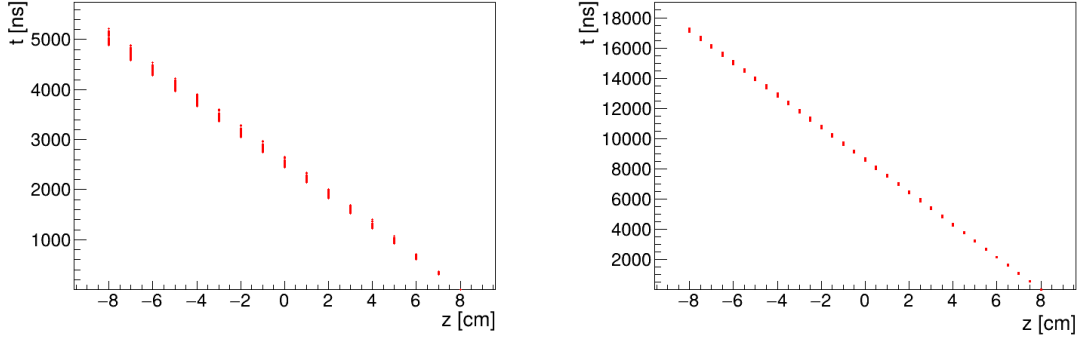


Figure 3.6: Dependence of the drift times of the simulated map $\bar{\mathcal{M}}$ on the z -coordinate. Two gas mixtures 90:10 (left) and 70:30 Ar:CO₂ (right) are compared. The spread is caused by varying Lorentz angles.

776 the electrons, we then estimate the means and the covariance matrix:

$$\bar{\mathbf{X}} = \frac{1}{N} \sum_{i=1}^N \mathbf{X}_i, \quad \Sigma = \frac{1}{N-1} \sum_{i=1}^N (\mathbf{X}_i - \bar{\mathbf{X}})(\mathbf{X}_i - \bar{\mathbf{X}})^T, \quad (3.8)$$

777 where \mathbf{X}_i represents the readout coordinates $(x'_i, y'_i, t_i)^T$ of the i -th electron. The
778 matrix (resp. its submatrix) can then be used to plot error ellipsoid (resp. el-
779 lipse). The axes correspond to the eigenvectors, errors along these axes for a given
780 confidence level p can be computed using the chi-squared distribution

$$\sigma_i = \sqrt{\lambda_i \chi_k^2(p)}, \quad (3.9)$$

781 where λ_i is the corresponding eigenvalue and k is the number of degrees of free-
782 dom.

783 As shown in Figs. 3.6 and 3.7, the drift times in the map are no longer propor-
784 tional to the z -coordinate due to the varying Lorentz angles in the inhomogeneous
785 magnetic field (see Equation 1.2). As expected, the effect is considerably larger in
786 gases with higher drift velocities. Similarly, the drift distortion (i.e., its deviation
787 from the vertical lines) is huge for the "faster" gas, but still significant for the
788 "slower" one, as demonstrated in Figs. 3.8 to 3.10.

789 When evaluating the map inside the grid, we use trilinear interpolation (see
790 Section 1.4.3). From now on, we will use the same symbol \mathcal{M} for this interpolated
791 simulation.

792 Finally, we need to invert the map to get the original detector coordinates
793 (x, y, z) from the given readout coordinates (x', y', t) . In our case, it is reasonable
794 to assume that the mapping $\bar{\mathcal{M}}$ (we lose the information about the distribution
795 (a wild idea how to recover this is in the Future section but it will only make sense
796 if the GEM is already accounted for and is very preliminary as there are many
797 factors to consider)) is one-to-one (as seen in the simulations). We implemented
798 two methods for this purpose: the gradient descent search (Section 3.2.2) and
799 interpolation on the inverse grid (Section 3.2.3).

800 3.2.1 Map Simulation

801 The simulation (?) of the map is a computationally heavy task. For this reason,
802 we use the MetaCentrum grid [3] to parallelize needed calculations. At first,

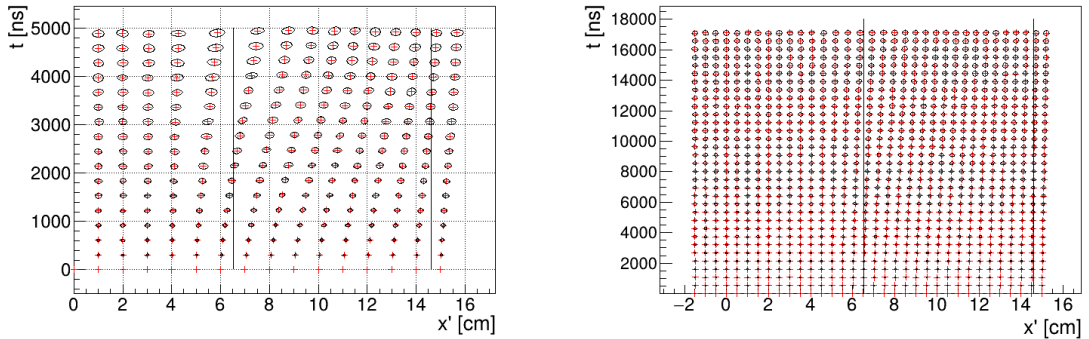


Figure 3.7: The $x't$ projection of the $\mathcal{M}(\mathbb{G}_{y=0})$ mapping of a part of the regular grid \mathbb{G} . The means $\overline{\mathcal{M}}(\mathbb{G}_{y=0})$ are marked with red crosses, and the diffusion error is denoted by black 95% confidence error ellipses computed from the diagonalized covariance matrices $\mathcal{M}_\Sigma(\mathbb{G}_{y=0})$. Two gas mixtures 90:10 (left) and 70:30 Ar:CO₂ (right) are compared. The first mixture shows differences of t for electrons with same initial z but different initial x . For the second mixture, these differences are negligible in comparison with the diffusion.

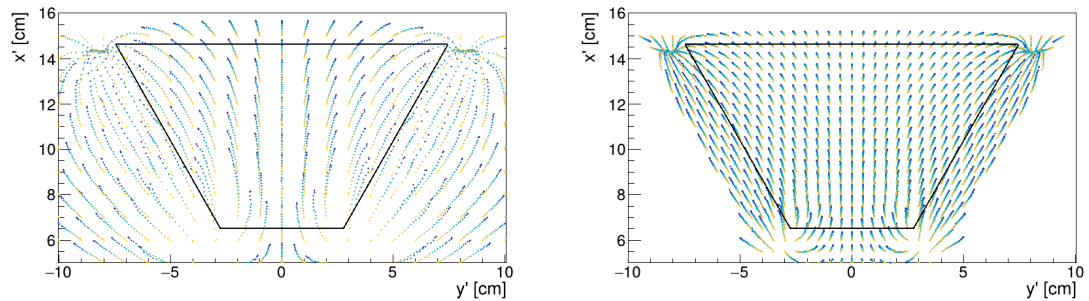
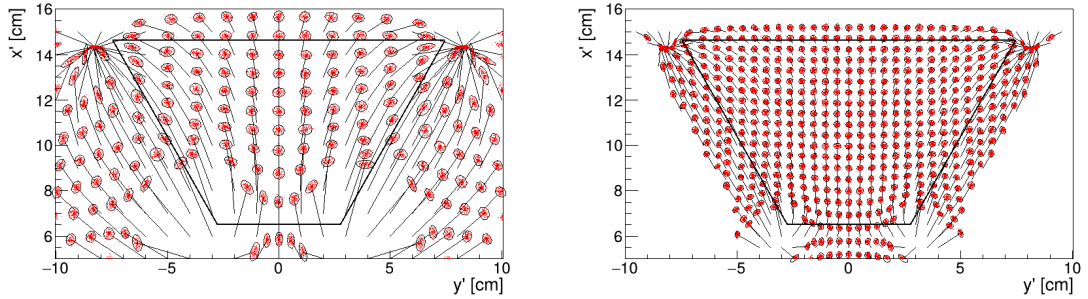
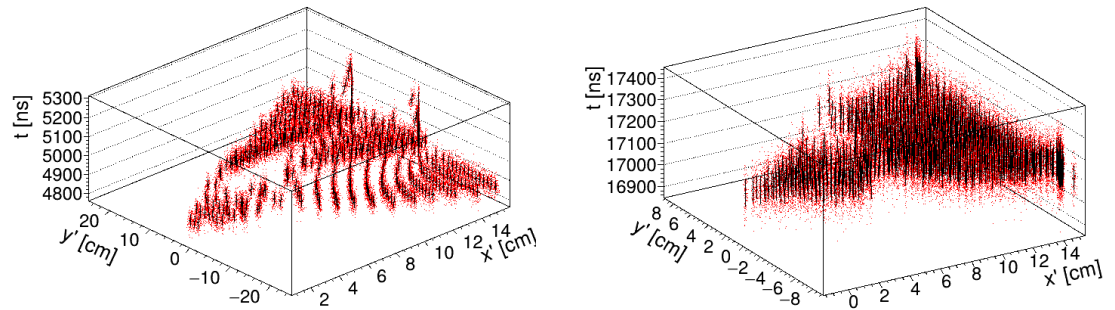


Figure 3.8: The regular grid \mathbb{G} projected by the mapping $\overline{\mathcal{M}}$ from the detector space onto the $x'y'$ plane (t is not plotted). Layers with lower z -coordinate (i.e., further away from the readout) are displayed with darker colors. The OFTPC volume is marked with black lines. Two gas mixtures 90:10 (left) and 70:30 Ar:CO₂ (right) are compared.



(a) The $x'y'$ projection of $\mathcal{M}(\mathbb{G}_{-8})$ (similar as in Fig. 3.8), the diffusion is denoted with the 95% error ellipses from the diagonalized sample covariance matrices $\mathcal{M}_\Sigma(\mathbb{G}_{-8}) \leftrightarrow$ Equation 3.8, and computed using Equation 3.9. The mean values $\bar{\mathcal{M}}(\mathbb{G}_{-8})$ are connected by black arrows with the corresponding starting position (x, y) of the simulated electrons. The OFTPC volume is marked with black lines.



(b) The full mapping $\mathcal{M}(\mathbb{G}_{-8})$, the diffusion is marked using standard error bars (black) from the diagonalized sample covariance matrices (Equations 3.8 and 3.9).

Figure 3.9: The $\mathcal{M}(\mathbb{G}_{-8})$ mapping of the bottom ($z = -8$ cm) layer \mathbb{G}_{-8} of the regular grid $\mathbb{G} \subset \mathcal{D}$. It includes both the mapping of means $\bar{\mathcal{M}}$ and of covariances \mathcal{M}_Σ . Individual electrons from the map simulation are marked with red dots. Two gas mixtures 90:10 (left) and 70:30 Ar:CO₂ (right) are compared.

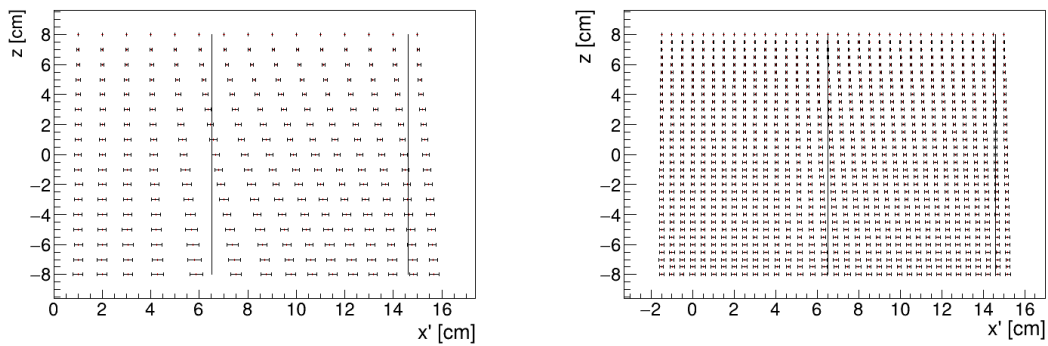


Figure 3.10: The readout coordinate x' for points on the grid $\mathbb{G}_{y=0}$ plotted against their initial coordinate z . The means are marked with red crosses, the diffusion in x' is denoted by standard error bars. Two gas mixtures 90:10 (left) and 70:30 Ar:CO₂ (right) are compared.

803 this was done by evenly distributing the simulated electrons across the individual
 804 jobs in a simulation with only one electron per vertex in the regular grid \mathbb{G} with
 805 a spacing of one centimeter. Later, a more efficient approach was implemented,
 806 accounting for the varying lengths of the drift of individual electrons. If we index
 807 the vertices of \mathbb{G} in the order of increasing coordinates y, x, z (picture will make
 808 things clearer), we can express the number n_l of full XY layers (i.e., electrons
 809 with the same z coordinate, the mapping of one such layer is shown in Fig. 3.9b)
 810 with index less than or equal to i

$$n_l(i) = \left\lfloor \frac{i}{n_{xy}} \right\rfloor, \quad (3.10)$$

811 where n_{xy} is the number of electrons in each XY layer calculated simply by count-
 812 ing the electrons that satisfy boundary conditions for x and y . These conditions
 813 should be mentioned above; sector condition + maximal x value. The number of
 814 electrons remaining in the top layer is then

$$n_r(i) = i \bmod n_{xy}. \quad (3.11)$$

815 Finally, we can calculate the sum of the drift gaps of electrons up to index i

$$d_{\text{sum}} = (z_{\max} - z_{\min})n_{xy}n_l - \frac{n_l(n_l - 1)}{2}n_{xy}l + n_r(z_{\max} - z_{\min} - n_l l). \quad (3.12)$$

816 We then use a binary search algorithm to find the maximum index i such that
 817 the value of this sum is less than the fraction $\frac{\text{job id}}{\max \text{ job id}}$ of the total sum. This way
 818 we obtain the minimal and the maximal index of electrons simulated in the given
 819 job.

820 The obtained map is then stored in a custom class template *Field*, could
 821 expand on that. Maybe earlier, since the same template is used for the magnetic
 822 field.

823 Simulation inside of one sector (at first double angle). Extra space on the
 824 sensor. Using qsub (not sure if important). Add plots of distortion of the coor-
 825 dinates.

826

827 3.2.2 Gradient Descent Algorithm

828 The first implemented method of reconstruction uses a gradient descent algorithm
 829 to calculate an inversion of the map $\overline{\mathcal{M}}$ in a given point. Gradient descent is
 830 an iterative minimization algorithm for multivariate functions. Let $R \in \mathcal{R}$ be
 831 a point in the readout space; we want to find a point $D = (x, y, z) \in \mathcal{D}$ in the
 832 detector space such that

$$\overline{\mathcal{M}}(D) = R = (x'_R, y'_R, t_R). \quad (3.13)$$

833 We define a function f_R in the readout space as a distance in this space:

$$f_R(x', y', t) = \sqrt{(x' - x'_R)^2 + (y' - y'_R)^2 + v_d^2(t - t_R)^2}, \quad (3.14)$$

834 where v_d is an approximation of the drift velocity in the TPC, obtained from the
 835 reconstruction in Section 3.1 (there will be an image with the linear fit here). We
 836 make an initial guess (actually in the original code we just take $z = 0$):

$$D_0 = (x'_R, y'_R, v_d t). \quad (3.15)$$

837 Assuming we have the n -th estimate D_n , we calculate the i -th component of the
 838 gradient of $f_R \circ \bar{\mathcal{M}}$ numerically using central differences: (signs look correct)

$$[\nabla(f_R \circ \bar{\mathcal{M}})]^i(D_n) \approx \frac{f_R(\bar{\mathcal{M}}(D_n + s \cdot e^i)) - f_R(\bar{\mathcal{M}}(D_n - s \cdot e^i))}{2s}, \quad (3.16)$$

839 where $e^i \in \mathcal{D}$ is the i -th coordinate vector and s is the step size. The step size
 840 should be sufficiently small; initially, we set it as a fraction $s = \frac{l}{10}$ of the map's
 841 grid spacing l . During the minimization, we check that $f_R(\bar{\mathcal{M}}(D_n)) < 10s$ at
 842 all times and decrease the step if needed. When using trilinear interpolation, it
 843 would be more efficient to calculate the gradient explicitly (\pm same result). This
 844 could be implemented inside the *Field* template class. The next iteration can be
 845 calculated as follows:

$$D_{n+1} = D_n - \gamma \nabla(f_R \circ \bar{\mathcal{M}})(D_n), \quad (3.17)$$

846 where $\gamma \in \mathbb{R}^+$ is the damping coefficient. It should be set to a small enough
 847 value to ensure convergence, but large enough for sufficient converging speed. In
 848 order to avoid oscillation around the minimum, we also check that the size of the
 849 damped gradient does not exceed (or get too close to) the current value of the
 850 non-negative function:

$$10 \|\gamma \nabla(f_R \circ \bar{\mathcal{M}})(D_n)\| < f_R(D_n), \quad (3.18)$$

851 and lower γ otherwise. The minimization stops either when the error $f_R(\bar{\mathcal{M}}(D_n))$
 852 drops below a specified value or when the number of iterations exceeds a certain
 853 limit (in this case, a message is printed into the console).

854 The parameters of this method can be further optimized (e.g., a better choice
 855 of γ and s , analytical computation of the gradient²); instead, we later decided to
 856 use the interpolation on the inverse grid described in the next section.

857 Measure reconstruction duration and compare it with the inverse grid inter-
 858 polation? Also compare the result? Typical evolution of D_n during search. Not
 859 sure if this has to be cited.

860 3.2.3 Interpolation on the Inverse Grid

861 Interpolation should be generally faster than the gradient descent since we don't
 862 need to iterate. We also don't need to optimize it to improve performance, if
 863 it's too slow we can even calculate the coefficients for the entire map before
 864 reconstruction (again, do some profiling). Very rough profiling shows that the
 865 difference in the current state is at least one order of magnitude.

²The gradient can be computed analytically when using the trilinear interpolation, see Eq. 1.21.

866 The best current algorithm uses the interpolation on the inverse grid. Rather
 867 than inverting the trilinearly interpolated map using a numerical minimization
 868 method as in the previous section, we take advantage of the fact that the map
 869 $\bar{\mathcal{M}}$ is one-to-one (isomorphism is supposed to preserve structure, not sure how
 870 to interpret that here, not the best description, we already (kind of) assume it
 871 is a bijection by saying we will invert it). Since we have simulated values of this
 872 map on a regular grid in the detector space \mathcal{D} , we also know the inverse map $\bar{\mathcal{M}}^{-1}$
 873 on the irregular inverse grid in the readout space \mathcal{R} . To get an approximation
 874 of the inverse map in the entire readout space, we can use interpolation (general
 875 concept, the specific choice is described below).

876 Since the inverse grid is irregular, trilinear interpolation cannot be applied.
 877 Given that the simulated map is dense enough to provide a good approximation
 878 considering the size of our pads, we can adopt a similar approach.³ As shown in
 879 Equation 1.21 in Section 1.4.3, trilinear interpolation (shouldn't need an article
 880 when talking about a general concept) can be expressed as a polynomial:

$$\hat{f}(x, y, z) = axyz + bxy + cxz + dyz + ex + fy + gz + h, \quad (3.19)$$

881 where a, b, c, d, e, f, g, h are coefficients uniquely determined by the values of the
 882 function at the vertices of the interpolation cell (can be calculated in the way
 883 shown in the mentioned equation, not sure what more to add). We can generalize
 884 this for a function defined on an irregular grid. Given the function values at any
 885 eight points, we can write a system of eight linear equations

$$\begin{pmatrix} x_1y_1z_1 & x_1y_1 & x_1z_1 & y_1z_1 & x_1 & y_1 & z_1 & 1 \\ \vdots & \vdots \\ x_8y_8z_8 & x_8y_8 & x_8z_8 & y_8z_8 & x_8 & y_8 & z_8 & 1 \end{pmatrix} \begin{pmatrix} a \\ \vdots \\ h \end{pmatrix} = \begin{pmatrix} f(x_1, y_1, z_1) \\ \vdots \\ f(x_8, y_8, z_8) \end{pmatrix}, \quad (3.20)$$

886 which has a unique solution for the coefficients for most values of (x_n, y_n, z_n) and
 887 $f(x_n, y_n, z_n)$, where $n \in \{1, \dots, 8\}$.

888 This approach introduces a small complication: finding the correct pseudocell
 889 (i.e., the image of eight vertices forming a cubic cell in the regular grid) in
 890 the inverse grid. The eight irregularly spaced vertices of this pseudocell do not
 891 define a unique volume, so there are multiple possible ways to partition \mathcal{R} into
 892 pseudocells, with no obvious choice among them.

893 We are currently ignoring this problem and performing binary search along
 894 x, y, z (in this order). It shouldn't matter too much because the 70/30 map
 895 doesn't cause such a big distortion and was even accidentally extrapolated for all
 896 z different from the central plane.

³A more complicated and computationally heavy alternative would be natural neighbor interpolation or Kriging.

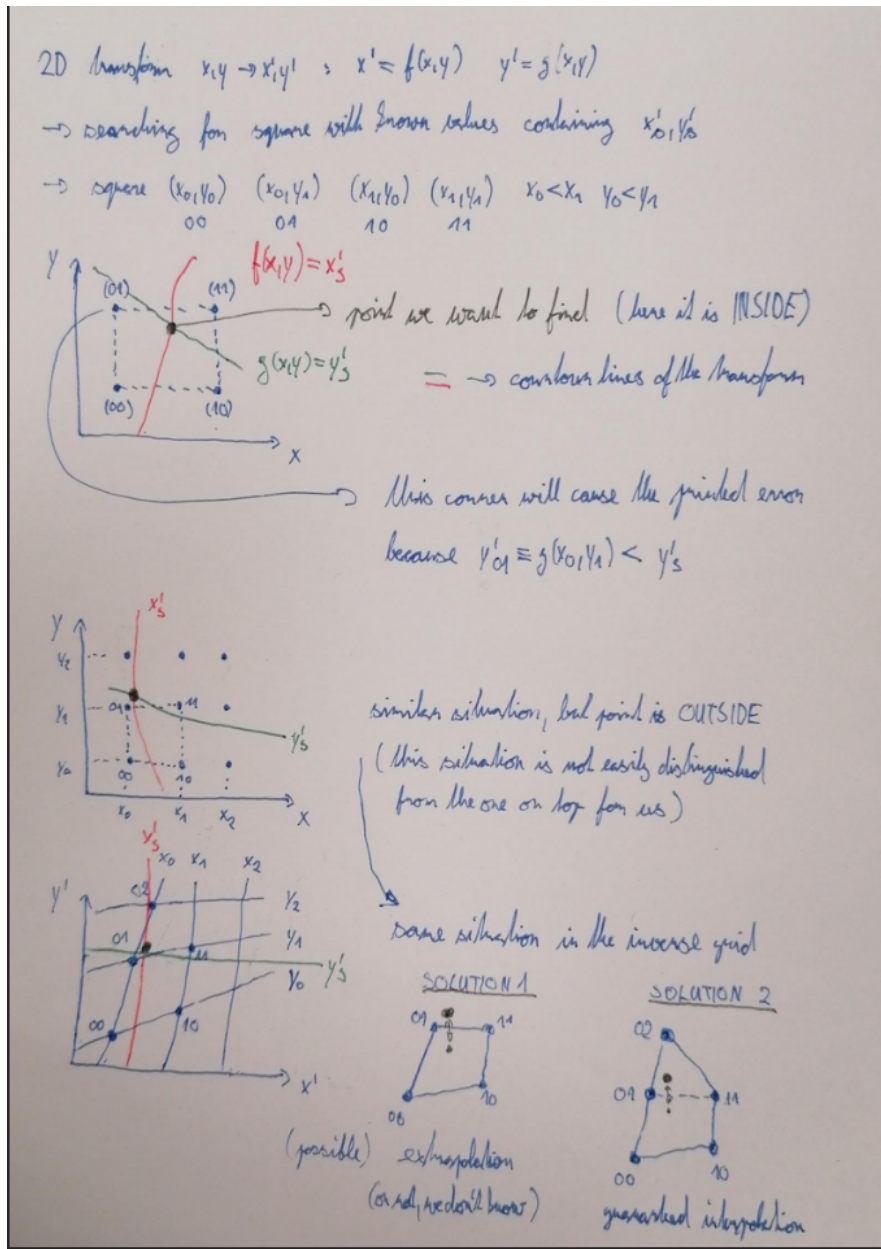


Figure 3.11: Selection of the points for interpolation. Create better images; use the explanation interpolation vs. extrapolation strange property. Solution 2 probably does not make much sense.

897 3.3 Reconstruction testing

898 The continuous reconstruction using the map was tested on microscopic tracks
 899 with parameters described in Sec. 2.1.1. The difference between the reconstructed
 900 positions obtained using the two map inversion algorithms was found to be smaller
 901 than the uncertainty from diffusion by several orders of magnitude. In its unop-
 902 timized state, the gradient descent search was significantly slower (at least ten
 903 times) than the interpolation on the inverse grid.

904 An example of reconstruction of tracks in 90:10 and 70:30 Ar:CO₂ gas mixture
 905 is shown in Fig. 3.12. We can clearly see that the results have improved com-

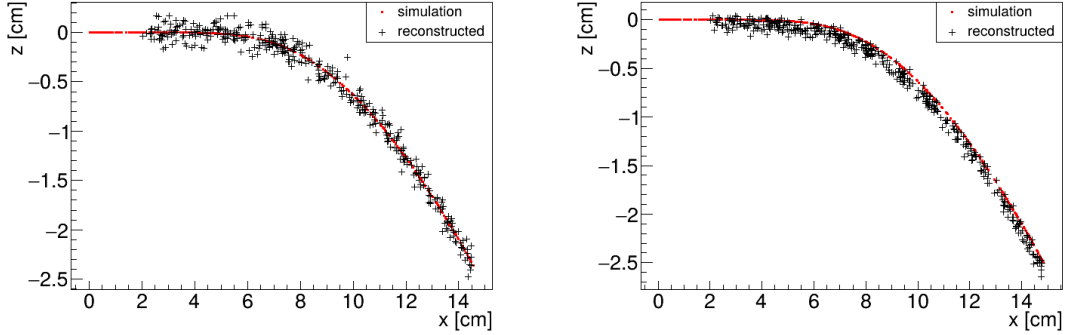


Figure 3.12: Reconstruction (black) of the starting position of ionization electrons (red) using the inversion of the ionization electron map. Two gas compositions 90:10 (left) and 70:30 Ar:CO₂ (right) are compared.

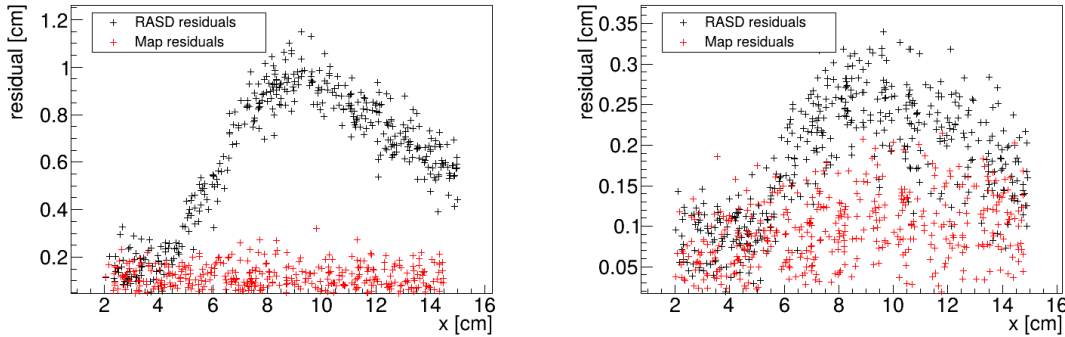


Figure 3.13: Comparison of residuals from the RASD (black) and map inversion (red) reconstruction methods. Tracks in two different gas compositions 90:10 (left) and 70:30 Ar:CO₂ (right) are compared.

pare to the Reconstruction Assuming Steady Drift (RASD) (shown in Fig. 3.2). A comparison of the residuals of reconstructed positions (i.e., their distances to the real starting positions) is shown in Fig. 3.13. The histograms of residuals, as well as residuals of individual coordinates, are shown in Figs. 3.14 and 3.15. The bin width for the histograms was chosen using the Scott's rule⁴. As expected, the mean values of the coordinate residuals is zero. The only exception is the z -coordinate in the 70:30 Ar:CO₂ track, where the mean is -0.064 cm (further than one standard deviation 0.051 cm from zero). This is caused by the non-zero initial energy of the ionization electrons (neglected in the other track) which is unaccounted for in the map simulation. Since the primary electron bends towards negative z , the ionization electrons are more likely to be released in this direction (and also bend in the magnetic field towards this direction).

3.4 Discrete Reconstruction

Reconstruction with pads and time bins. Maybe testing different pads.

⁴The optimal bin width for normally distributed data of size N with sample standard deviation $\hat{\sigma}$ is $\hat{\sigma} \sqrt[3]{\frac{24\sqrt{\pi}}{N}}$ [45].

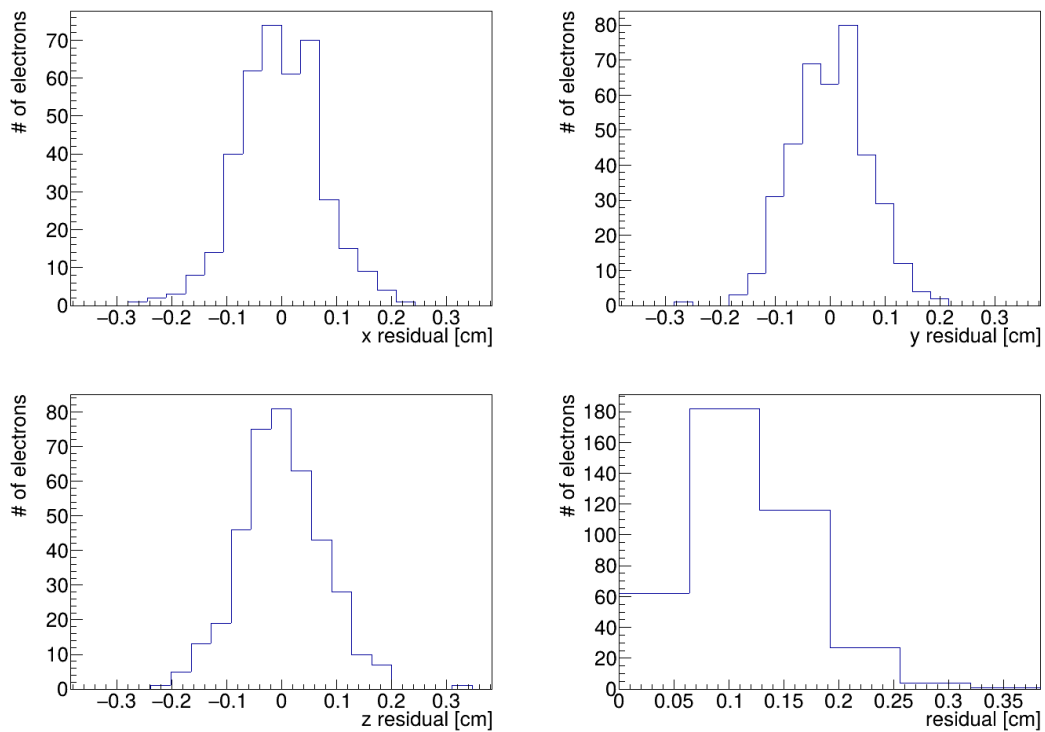


Figure 3.14: Map inversion reconstruction residuals (for the individual coordinates and total) of the testing track in 90:10 Ar:CO₂ gas mixture.

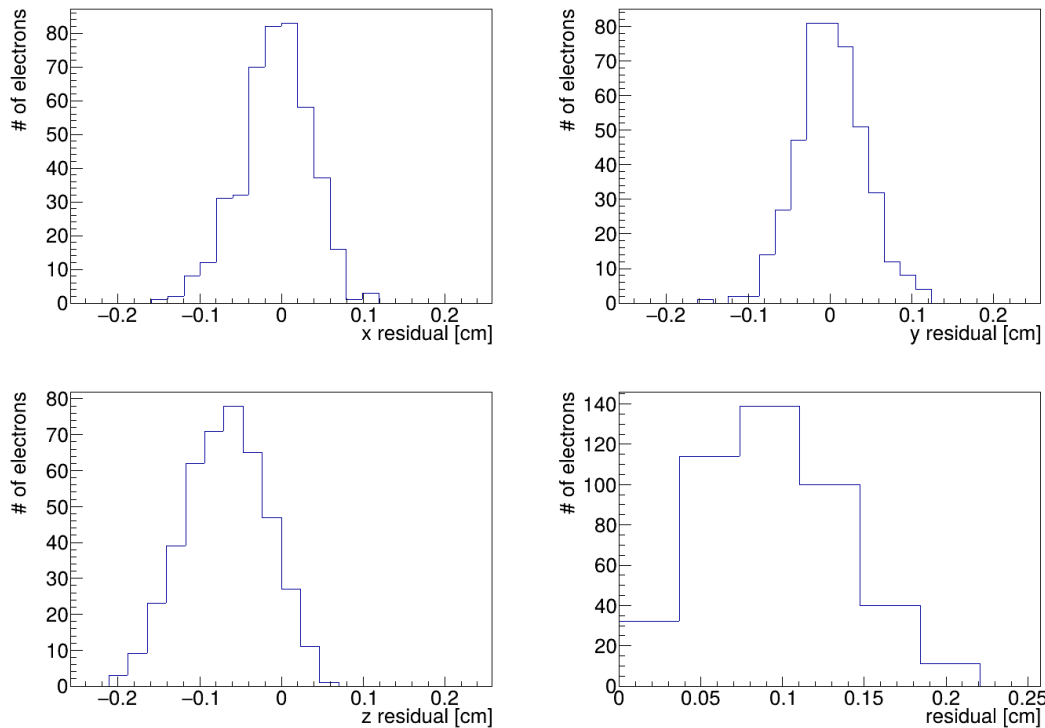


Figure 3.15: Map inversion reconstruction residuals (for the individual coordinates and total) of the testing track in 70:30 Ar:CO₂ gas mixture.

920 It is also possible to make this a subsection of the map, making the previous
 921 subsections parts of a new subsection 'Map Inversion'.

922 In order to get a more realistic representation of a track measured in the
 923 OFTPC, we need to take the discretization of the position and time data into
 924 account. The readout of the OFTPC will consist of 128 pads, their layout is
 925 shown in Fig. 1.13. Time is read out in discrete bins of size $t_{\text{bin}} = 100 \text{ ns}$.

926 As the first approximation, we can neglect the multiplication in the triple-GEM,
 927 and assume an ideal charge readout. The time measurement starts at the begin-
 928 ning of the electron/positron simulation (depending on the specific simulation it
 929 can correspond to the production in the target or when entering the OFTPC,
 930 here the specific time doesn't matter too much since the primary particle trav-
 931 els basically at light speed (30 ps/cm) which is circa immediate given the time
 932 binning). Randomize this time a bit and see what it does to the reconstruction.
 933 The readout coordinates $(x', y', t) \in \mathcal{R}$ of each ionization electron can be mapped
 934 to the pad coordinates $(n_{\text{pad}}, n_t) \in \mathcal{P}$:

$$n_{\text{pad}} = n : (x', y') \in \left[x_{1,n} - \frac{g}{2}, x_{2,n} + \frac{g}{2} \right] \times \left[y_{1,n} - \frac{g}{2}, y_{2,n} + \frac{g}{2} \right], \quad (3.21)$$

$$n_t = \left\lceil \frac{t}{t_{\text{bin}}} \right\rceil, \quad (3.22)$$

935 where $x, y_{1,n}$ and $x, y_{2,n}$ are the opposing pad corner coordinates, and g is the
 936 gap between the pads (described in detail in Section 1.4.2). This way, the clos-
 937 est pad is assigned to each readout position within the OFTPC volume⁵. Makes
 938 sense since the pads attract the electrons, the inhomogeneity of electric field is
 939 neglected. The number of electrons collected by each pad (i.e., collected charge)
 940 in each time bin is then counted and serves as a weight for the energy recon-
 941 struction. The reconstructed track consists of points for each $(n, n_t) \in \mathcal{P}$, we get
 942 these by reconstructing the position of a hypothetical electron with the readout
 943 coordinates of the pad/time bin center:⁶

$$\mathcal{D} \ni (x, y, z) = \overline{\mathcal{M}} \left(x_{c,n}, y_{c,n}, \left(n_t - \frac{1}{2} \right) t_{\text{bin}} \right). \quad (3.23)$$

⁵Some positions near the wall are not handled and some pads extend beyond the OFTPC volume. This is where an electric field simulation would come in handy.

⁶Mapping the center of the pad (along with the midpoint of the time bin) isn't necessarily the best approach since it might not correspond to the average parameters of an electron with these readout parameters.

944 4. Energy Reconstruction

945 The second stage is the reconstruction of the particle's energy using a fit of its
946 reconstructed track (see Section 3). We have tested three ways of reconstructing
947 the energy. Fitting is done using the MINUIT algorithm implemented in
948 ROOT [2]. Cite some CERN article directly on MINUIT, can add a section. Or
949 is it done using MIGRAD? The circle and RK4 probably was.

950 The **Cubic Spline Fit** was a tested and later rejected method of energy
951 reconstruction. It uses smoothly connected piecewise cubic polynomials between
952 uniformly spaced nodes. The reconstructed energy is calculated using the fit
953 parameters by computing the radius of curvature in different points of the fitted
954 curve using the known magnitude of the magnetic field perpendicular to the
955 trajectory. We rejected this method because the tuning of the fit turned out
956 to be unpractical compared to the other used methods. Reconstructs energy at
957 every position (even though the actual energy doesn't change much) and it might
958 be slower but no profiling has been done yet. Of course, it wasn't tested on the
959 newer track reconstruction methods at all.

960 The **Circle and Lines Fit** was chosen as an alternative since this corresponds
961 to the shape of a trajectory of a charged particle crossing a finite volume with
962 a homogeneous magnetic field. The energy of the particle can be estimated using
963 the fitted radius and the magnitude of the perpendicular magnetic field in the
964 middle of the TPC.

965 The **Runge-Kutta Fit** uses the 4th order Runge-Kutta numerical integration
966 described in Section 2.2. Initial parameters of the track (including the particle's
967 energy) are optimized so that the integrated trajectory fits to the reconstructed
968 one. This fit can also be performed as a single parameter (i.e., energy) fit if we
969 get the initial position and orientation of the particle on the entrance to the TPC
970 from previous detectors (TPX3 and MWPC, see Section 0.2).

971 4.1 Cubic Spline Fit

972 The first method for the estimation of the kinetic energy of the particle uses
973 a cubic spline fit. We use an electron track simulated using the microscopic

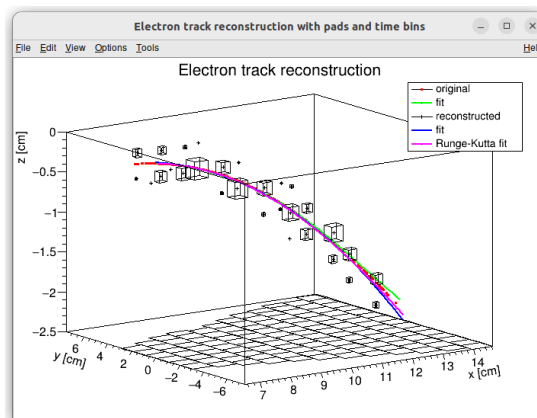


Figure 4.1: Example of a fitted reconstructed track. Swap for better image.

simulation, described in detail in Section 2.1.1. The track was reconstructed using the map described in Section 3.2.

In order to calculate the spline, we use the class *TSplines3* from ROOT. This allows us to evaluate the spline using the coordinates (x_n, z_n) of each node and the derivatives d_1, d_2 in the first and the last node. We can fit these parameters of a fixed amount of nodes to the simulated trajectory. We use the IMPROVE algorithm provided by the *TMinuit* class in ROOT (there are some guidelines for fonts in MFF UK template (Czech version) that I will eventually apply (see notes in the conclusion)). This algorithm attempts to find a better local minimum after converging (could reformulate a bit, taken word for word from some manual).

After the fit converges, we calculate an energy estimate using the radius of curvature, which we can extract from the fitted spline equation at every point of the trajectory. The part of the spline corresponding to a given node is defined as

$$z(x) = z_n + b\Delta x + c(\Delta x)^2 + d(\Delta x)^3, \quad (4.1)$$

where $\Delta x = x - x_n$ and b, c, d are coefficients. Using this equation, we derive the radius of curvature¹ as:

$$r(x) = \frac{(1 + z'^2(x))^{\frac{3}{2}}}{z''(x)} = \frac{(1 + (b + 2c\Delta x + 3d(\Delta x)^2)^2)^{\frac{3}{2}}}{2c + 6d\Delta x}. \quad (4.2)$$

Based on the geometry of our detector, we assume that the magnetic field satisfies $\mathbf{B}(x, 0, z) = (0, B(x, z), 0)$ for a track in the XZ plane. Since the electron is relativistic, the effect of the electric field on its trajectory is negligible. The Lorentz force F_L is then always perpendicular to the momentum of the electron and acts as a centripetal force F_c (not quite sure how to handle this then?):

$$\begin{aligned} \mathbf{F}_L &= \mathbf{F}_c, \\ \|e\mathbf{v} \times \mathbf{B}\| &= \frac{\gamma m_e v^2}{r}, \\ ec\beta B &= \frac{E_{0e}\beta^2}{r\sqrt{1 - \beta^2}}, \\ \sqrt{1 - \beta^2} &= \frac{E_{0e}\beta}{ecBr}, \end{aligned} \quad (4.3)$$

$$\beta^2(x) = \left[1 + \left(\frac{E_{0e}}{ecB(x, z(x))r(x)} \right)^2 \right]^{-1}, \quad (4.4)$$

where e is the elementary charge, c is the speed of light in vacuum, m_e is the rest mass of electron, $E_{0e} = m_e c^2$ is its rest energy, γ is the Lorentz factor, \mathbf{v} is the velocity of the electron, and $\beta = \frac{v}{c}$. The kinetic energy for a given point on the trajectory is then given as

$$E_{\text{kin}}(x) = \left(\frac{1}{\sqrt{1 - \beta^2(x)}} - 1 \right) E_{0e}. \quad (4.5)$$

¹For the general formula see https://en.wikipedia.org/wiki/Curvature#Graph_of_a_function.

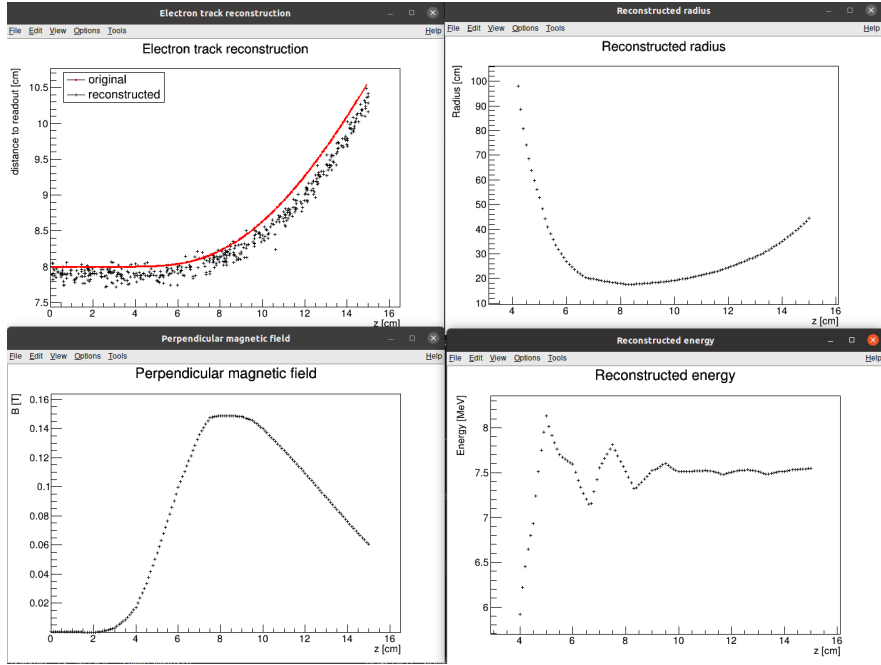


Figure 4.2: First attempt at a track reconstruction using only the drift velocity. Spline energy reconstruction attempt. Swap for better image(s) – subfigure environment, correct coordinates.

998 We can then average these estimates at multiple points (possibly using some
 999 weights to account for the change in accuracy, this wasn't optimized and we just
 1000 ended with the graph) to get a single value. This method was later rejected in
 1001 favor of the circle and lines fit (the name was already established at the beginning
 1002 of the chapter) described in the next section. Add some figures.

1003 4.2 Circle and Lines Fit

1004 Another way to estimate the particle's kinetic energy is to fit its (??) trajectory
 1005 with a circular arc with lines attached smoothly. This shape of trajectory cor-
 1006 responds to a movement of a charged particle through a homogeneous magnetic
 1007 field perpendicular to the particle's momentum and limited to a certain volume.
 1008 In general, the shape of such a trajectory with a non-perpendicularly oriented
 1009 momentum is a spiral. In our case, the magnetic field is approximately toroidal
 1010 and the particle motion is nearly perpendicular to it (verify, could add some
 1011 magnetic field plots in different vertical planes; shouldn't have a big effect on the
 1012 reconstructed radius anyway). At first, we tested a 2D version of this fit, then
 1013 we adapted it to 3D.

1014 The field in our detector is not homogeneous, it is therefore not entirely clear
 1015 what value of magnetic field should be used along with the fitted radius (using
 1016 equations 4.4 and 4.5) to get the best estimate for the kinetic energy. Since we
 1017 only use this method as the first iteration of the particle's energy that we later
 1018 refine, an optimal solution of this problem is not required. Instead, we tested two
 1019 options: taking the value of the field in the middle of the fitted circular arc (or
 1020 is it in the middle x of the OFTPC?) and taking the average field along it. We

1021 haven't really tried to plot this for multiple tracks, but these estimates are saved
1022 somewhere and could be plotted.

1023 4.2.1 Two-dimensional fit

1024 In the 2D case, the fitted function used for the electron track² described in Section
1025 2.1.1 (one specific track at the time, technically this function doesn't work
1026 for a curvature that gets outside of the semicircle) is defined as follows:

$$z(x) = \begin{cases} a_1x + b_1 & x < x_1 \\ z_0 + \sqrt{r^2 - (x - x_0)^2} & x_1 \leq x \leq x_2 \\ a_2x + b_2 & x > x_2 \end{cases}, \quad (4.6)$$

1027 where $a_{1,2}$ and $b_{1,2}$ are the parameters of the lines, (x_0, z_0) is the center of the circle,
1028 r is its radius, and $(x_{1,2}, z_{1,2})$ are the coordinates of the function's nodes. That
1029 means we have 9 parameters ($z_{1,2}$ are not used in the function) along with 2 continuity
1030 conditions and 2 smoothness conditions (9 parameters of the described
1031 function, 5 of them independent after taking the conditions into account). For
1032 the fit, we use the coordinates of the nodes and the radius of the circle, which
1033 gives us 5 independent parameters (only the radius has to be larger than half
1034 of the distance between nodes). The continuity conditions (combined with the
1035 relations for $z_{1,2}$) are

$$z_{1,2} = a_{1,2}x_{1,2} + b_{1,2} = z_0 - \sqrt{r^2 - (x_{1,2} - x_0)^2}, \quad (4.7)$$

1036 the smoothness conditions are

$$a_{1,2} = \frac{x_0 - x_{1,2}}{\sqrt{r^2 - (x_{1,2} - x_0)^2}}. \quad (4.8)$$

1037 Together with the Equation 4.7 we get the values of $b_{1,2}$

$$b_{1,2} = z_{1,2} - a_{1,2}x_{1,2}. \quad (4.9)$$

1038 For the coordinates of the center of the circle, we can use the fact that the center
1039 has to lie on the axis of its chord. In other words, there is a value of a parameter t
1040 such that, using the parametric equation of the axis

$$\begin{pmatrix} x_0 \\ z_0 \end{pmatrix} = \begin{pmatrix} \frac{x_1+x_2}{2} \\ \frac{z_1+z_2}{2} \end{pmatrix} + t \begin{pmatrix} \frac{z_2-z_1}{2} \\ \frac{x_1-x_2}{2} \end{pmatrix}. \quad (4.10)$$

1041 At the same time, the center has to be in a distance of r from the nodes:

$$\begin{aligned} (x_1 - x_0)^2 + (z_1 - z_0)^2 &= r^2, \\ \left(\frac{x_1 - x_2}{2} + \frac{z_1 - z_2}{2}t \right)^2 + \left(\frac{z_1 - z_2}{2} + \frac{x_2 - x_1}{2}t \right)^2 &= r^2, \\ \left(\left(\frac{x_2 - x_1}{2} \right)^2 + \left(\frac{z_2 - z_1}{2} \right)^2 \right)t^2 + \left(\frac{x_2 - x_1}{2} \right)^2 + \left(\frac{z_2 - z_1}{2} \right)^2 - r^2 &= 0. \end{aligned} \quad (4.11)$$

²Electron tracks bend towards negative z , we need to use the upper part of the circle.

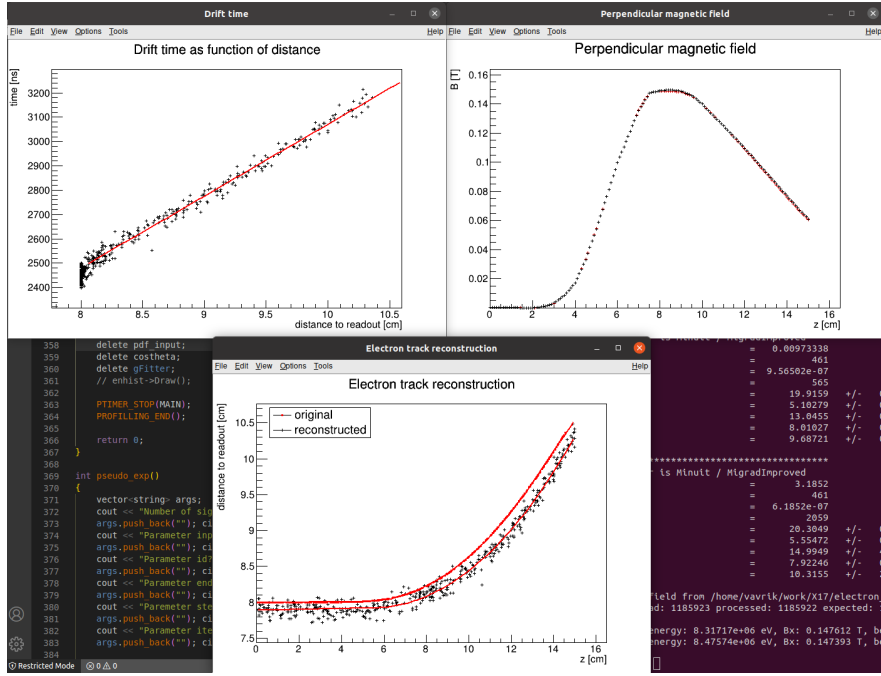


Figure 4.3: First attempt at a track reconstruction using only the drift velocity. Circle and Lines Fit in 2D. Swap for better image, correct coordinates. Bias should be described in the previous chapter, not here.

1042 Since our electron track bends towards negative z and $x_2 > x_1$, we only care
 1043 about the solution with $t > 0$

$$t = \sqrt{\frac{r^2}{\left(\frac{x_2-x_1}{2}\right)^2 + \left(\frac{z_2-z_1}{2}\right)^2} - 1}, \quad (4.12)$$

$$\begin{aligned} x_0 &= \frac{x_1 + x_2}{2} + \frac{z_2 - z_1}{2} \sqrt{\frac{r^2}{\left(\frac{x_2-x_1}{2}\right)^2 + \left(\frac{z_2-z_1}{2}\right)^2} - 1}, \\ z_0 &= \frac{z_1 + z_2}{2} - \frac{x_2 - x_1}{2} \sqrt{\frac{r^2}{\left(\frac{x_2-x_1}{2}\right)^2 + \left(\frac{z_2-z_1}{2}\right)^2} - 1}. \end{aligned} \quad (4.13)$$

1044 The function defined in Equation 4.6 along with equations 4.8, 4.9, and 4.13
 1045 derived using the continuity and smoothness conditions (combined with the re-
 1046 lations for $z_{1,2}$) fully define our fitted function with parameters $r, x_{1,2}, z_{1,2}$. Some
 1047 pictures of the fit on the tested track. Results of the fit. Again, the actual fit
 1048 uses 8-z. Use GeoGebra schematics to generate a picture of 2D geometry.

1049 4.2.2 Three-dimensional fit

1050 In three dimensions, the shape of a trajectory of a charged particle in a uniform
 1051 magnetic field is a cylindrical helix. Nevertheless, since we assume that the
 1052 field is approximately perpendicular to the particle's momentum at all times,
 1053 we will further approximate the trajectory with a circular arc $\mathbf{X}_C(\phi)$ (with lines
 1054 $\mathbf{X}_{L1}(t), \mathbf{X}_{L2}(s)$ attached smoothly).

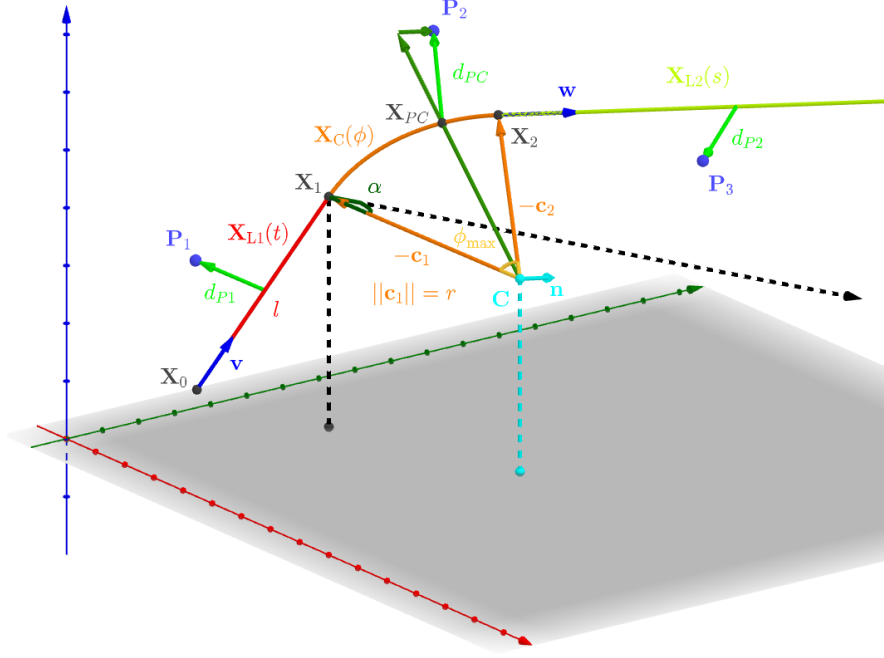


Figure 4.4: Visualization of the 3D geometry of the Circle and Lines Fit and its parameters.

We assume that the initial position $\mathbf{X}_0 = (x_0, y_0, z_0)$ and direction θ, φ (spherical angles as in Section 1.4.2) are known, since this information will be provided by TPX3 and MWPC layers. We could further refine it at the end of the current algorithm with some kind of global fit (all detector layers). The fit then has four free parameters (see Fig. 4.4):

- the length of the first line l (as measured from the initial position),
- the radius of the circular arc r ,
- the central angle of the arc $\phi_{\max} \in [0, 2\pi]$,
- the direction of the curvature given by the angle $\alpha \in [0, 2\pi]$ (right-handed with respect to the particle direction, $\alpha = 0$ if the particle curves towards negative z in a plane given by $\hat{\mathbf{z}}$ and the direction vector).

Using these parameters, we can derive a parametrization of the whole curve. Let \mathbf{v} be the initial unit direction vector, i.e., using the spherical angles

$$\mathbf{v} = (\cos \varphi \cos \theta, \sin \varphi \cos \theta, \sin \theta)^T, \quad (4.14)$$

then we can parameterize the first line as follows:

$$\mathbf{X}_{L1}(t) = \mathbf{X}_0 + t\mathbf{v} \quad t \in [0, l]. \quad (4.15)$$

This gives us the starting point of the arc

$$\mathbf{X}_1 = \mathbf{X}_{L1}(l) = \mathbf{X}_0 + l\mathbf{v}. \quad (4.16)$$

The vector \mathbf{c}_1 that lies in the plane of curvature and points from \mathbf{X}_1 to the center of curvature can be calculated using a composition of rotations. First, we rotate \mathbf{v} to point in the $\hat{\mathbf{x}}$ direction, the normal for $\alpha = 0$ than points in the $-\hat{\mathbf{z}}$ direction,

1073 we apply the α rotation and reverse the rotations into the $\hat{\mathbf{x}}$ direction: (parameters
1074 are explained in the bullet points above)

$$\begin{aligned}
\mathbf{c}_1 &= R_z(\varphi)R_y(-\theta)R_x(\alpha)R_y\left(\frac{\pi}{2}\right)R_y(\theta)R_z(-\varphi)\mathbf{v}, \\
&= R_z(\varphi)R_y(-\theta)R_x(\alpha)(-\hat{\mathbf{z}}), \\
&= \begin{pmatrix} \cos \varphi & -\sin \varphi & 0 \\ \sin \varphi & \cos \varphi & 0 \\ 0 & 0 & 1 \end{pmatrix} \begin{pmatrix} \cos \theta & 0 & -\sin \theta \\ 0 & 1 & 0 \\ \sin \theta & 0 & \cos \theta \end{pmatrix} \begin{pmatrix} 1 & 0 & 0 \\ 0 & \cos \alpha & -\sin \alpha \\ 0 & \sin \alpha & \cos \alpha \end{pmatrix} \begin{pmatrix} 0 \\ 0 \\ -1 \end{pmatrix}, \quad (4.17) \\
&= \begin{pmatrix} -\sin \alpha \sin \varphi + \cos \alpha \cos \varphi \sin \theta \\ \sin \alpha \cos \varphi + \cos \alpha \sin \varphi \sin \theta \\ -\cos \alpha \cos \theta \end{pmatrix}.
\end{aligned}$$

1075 Signs should be correct because right-handed rotation around y rotates z into x
1076 and this one is the opposite. Seems like in this part of the code θ is actually taken
1077 from the pole. Instead of the equator plane. Similarly by rotating $\hat{\mathbf{y}}$, we can get
1078 the normal vector $\mathbf{n} = \mathbf{v} \times \mathbf{c}_1$ perpendicular to the plane of the trajectory:

$$\mathbf{n} = R_z(\varphi)R_y(-\theta)R_x(\alpha)\hat{\mathbf{y}} = \begin{pmatrix} -\cos \alpha \sin \varphi - \sin \alpha \cos \varphi \sin \theta \\ \cos \alpha \cos \varphi - \sin \alpha \sin \varphi \sin \theta \\ \sin \alpha \cos \theta \end{pmatrix}. \quad (4.18)$$

1079 This allows us to express the coordinates of the center \mathbf{C} of the circular arc:

$$\mathbf{C} = \mathbf{X}_1 + r\mathbf{c}_1. \quad (4.19)$$

1080 We can then get the parametrization and the endpoint of the circular arc using
1081 Rodrigues' rotation formula: (all parameters explained in the bullet points above)

$$\begin{aligned}
\mathbf{c}_2 &= \mathbf{c}_1 \cos \phi_{\max} + (\mathbf{n} \times \mathbf{c}_1) \sin \phi_{\max} + \mathbf{n}(\mathbf{n} \cdot \mathbf{c}_1)(1 - \cos \phi_{\max}), \\
&= \mathbf{c}_1 \cos \phi_{\max} - \mathbf{v} \sin \phi_{\max},
\end{aligned} \quad (4.20)$$

$$\mathbf{X}_C(\phi) = \mathbf{C} - r(\mathbf{c}_1 \cos \phi - \mathbf{v} \sin \phi) \quad \phi \in [0, \phi_{\max}], \quad (4.21)$$

$$\mathbf{X}_2 = \mathbf{X}_C(\phi_{\max}) = \mathbf{C} - r\mathbf{c}_2, \quad (4.22)$$

1082 and if we define the direction vector of the second line, we also get its parametrization
1083

$$\mathbf{w} = \mathbf{v} \cos \phi_{\max} + (\mathbf{n} \times \mathbf{v}) \sin \phi_{\max} = \mathbf{v} \cos \phi_{\max} + \mathbf{c}_1 \sin \phi_{\max}, \quad (4.23)$$

$$\mathbf{X}_{L2}(s) = \mathbf{X}_2 + s\mathbf{w} \quad s \in [0, \infty). \quad (4.24)$$

1084 The fit is performed as a (weighted) least square minimization (MIGRAD
1085 ROOT), therefore we need to derive the distance of any point \mathbf{P} to the fitted
1086 curve. For the first line, we simply compute the parameter value of the closest
1087 point on the line:

$$\begin{aligned}
t_P &= \mathbf{v} \cdot (\mathbf{P} - \mathbf{X}_1), \\
d_{P1} &= \|\mathbf{P} - \mathbf{X}_{L1}(t_P)\|.
\end{aligned} \quad (4.25)$$

1088 If the parameter value is outside of its bounds defined above, we take the boundary
1089 value instead. The distance to the second line is computed likewise. For the

1090 circular arc (specific circular arc in the fit), we find the closest point (on the arc)
 1091 by projecting the center connecting line onto the arc plane:

$$\mathbf{X}_{PC} = \mathbf{C} + r \frac{(\mathbf{P} - \mathbf{C}) - (\mathbf{n} \cdot (\mathbf{P} - \mathbf{C}))\mathbf{n}}{\|(\mathbf{P} - \mathbf{C}) - (\mathbf{n} \cdot (\mathbf{P} - \mathbf{C}))\mathbf{n}\|}, \quad (4.26)$$

$$d_{PC} = \|\mathbf{P} - \mathbf{X}_{PC}\| \quad (4.27)$$

1092 If the point \mathbf{X}_{PC} lies outside of the arc, distance to the closest endpoint is taken
 1093 instead. The shortest distance out of d_{P1}, d_{PC}, d_{P2} is then taken as the distance
 1094 to the curve. When calculating energy with the average field, only the arc is
 1095 considered. Middle field in the current implementation taken in the middle x
 1096 plane (intersection with the curve). TVirtualFitter+MIGRAD, maximal num of
 1097 iterations, toleration. Different uncertainties in x, y, z not taken into account.

1098 Fit details (parameter bounds, initial setting).

1099 4.2.3 Testing on a Runge-Kutta sample

1100 The three dimensional circle and lines fit was tested on a sample of Runge-Kutta
 1101 tracks with randomized parameters described in Section 2.2.1. These tracks of
 1102 primary electrons and positrons consist of points calculated with the RK4 algo-
 1103 rithm for a given proper time step (step can be adjusted by dividing by the gamma
 1104 factor → detector time). Fitting with circle only was also partially implemented
 1105 (didn't work but could be fixed/tuned).

1106 4.3 Runge-Kutta Fit

1107 The Runge-Kutta fit uses the Runge-Kutta 4th order (RK4) numerical integra-
 1108 tion of the equation of motion (see Section 2.2) to find the best values of the track
 1109 parameters – the track origin, initial velocity direction and the kinetic energy. In
 1110 order to speed up the energy reconstruction, an initial guess of these parameters
 1111 can be obtained from the 3D circle fit described in the previous section. Fur-
 1112 thermore, assuming we know the track origin and orientation, we can perform
 1113 a single parameter fit of the kinetic energy (do some profiling and show that it is
 1114 faster – below in the microscopic testing).

1115 The fit is performed as a least square minimization of the (weighted) distances
 1116 of the track points (true ionization vertices from the simulation or reconstructed
 1117 points). The simulated RK4 track consists of line segments with known endpoints,
 1118 therefore we can calculate the distance of a point from this segment analogically
 1119 to Equation 4.25 with \mathbf{v} given as a unit vector in the direction of the segment.

1120 We need to find the segment with the lowest distance. We assume, that the
 1121 distance $d_{\mathbf{P}}(\tau)$ of a point \mathbf{P} to the point on the track (a curve parameterized
 1122 by the proper time τ) $\mathbf{X}(\tau)$ has a single minimum (local and global), no local
 1123 maximum (except the interval endpoints) and no saddle point

$$\exists! \tau_{\min} \in [0, \tau_N]: (\forall \tau \in [0, \tau_N]: d_{\mathbf{P}}(\tau) \geq d_{\mathbf{P}}(\tau_{\min})) \vee \frac{dd_{\mathbf{P}}}{d\tau}(\tau_{\min}) = 0, \quad (4.28)$$

1124 where N is the number of RK4 steps. This is a reasonable assumption for a track
 1125 with an approximate shape of a circular arc with a radius r , since the distance d

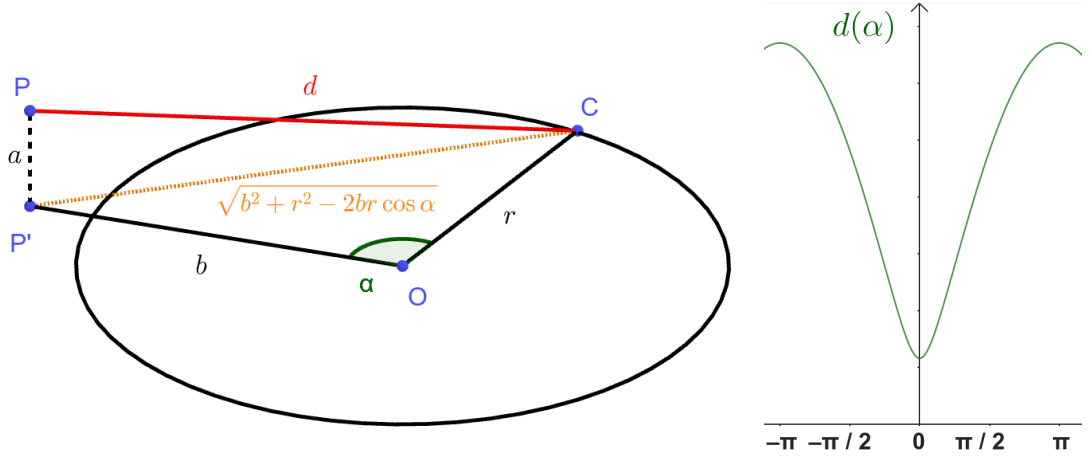


Figure 4.5: Demonstration of the convexity of the distance function $d(\alpha)$ for a circular track (see Equation 4.29).

from a point **C** on the corresponding circle of a point **P** offset by a from the arc plane and by b from the arc's center when projected on its plane is given by the law of cosines:

$$d^2 = a^2 + b^2 + r^2 - 2br \cos \alpha, \quad (4.29)$$

where α is the angle between points **C** and **P** as seen from the center of the arc (see Fig. 4.5). This function is strictly convex for $\alpha \in (-\frac{\pi}{2}, \frac{\pi}{2})$ and in our case, the center of the arc lies outside of the detector and α is restricted to a small interval around zero (especially considering that the initial guess should make the fitted trajectory reasonably close to any relevant point, in the worst-case scenario, the distance is overestimated which should keep the fit from converging to such solutions).

In a more general case, if we consider the vector $\mathbf{a}(\tau) = \mathbf{P} - \mathbf{X}(\tau)$ whose size is $\|\mathbf{a}(\tau)\| = d_{\mathbf{P}}(\tau)$, then we get

$$2d_{\mathbf{P}} \frac{dd_{\mathbf{P}}}{d\tau} = \frac{dd_{\mathbf{P}}^2}{d\tau} = 2\mathbf{a} \cdot \frac{d\mathbf{a}}{d\tau} = -2\mathbf{a} \cdot \frac{d\mathbf{X}}{d\tau}, \quad (4.30)$$

therefore for the derivative of $d_{\mathbf{P}}(\tau)$ to be zero, $\mathbf{a}(\tau)$ has to be perpendicular to the tangent of the track. In 3D, for a given $\mathbf{X}(\tau)$, this condition restricts **P** to a plane. This means that on a curving track, for any two points $\mathbf{X}(\tau_1), \mathbf{X}(\tau_2)$ with non-parallel tangents, we can find a point **P** that has $\frac{dd_{\mathbf{P}}}{d\tau}(\tau_1) = \frac{dd_{\mathbf{P}}}{d\tau}(\tau_2) = 0$, which violates the assumption 4.28. If we have a circle-and-lines track as described in the previous sections, such a point has to lie outside of the circular sector given by the arc.

For a planar track $\mathbf{X}(\tau) = (X_1(\tau), X_2(\tau))$, the envelope of all its normals is the evolute of the curve (i.e., the set of centers of all its osculating circles). If the track has a monotonous tangent angle

$$\alpha(\tau) = \text{atan} \frac{\frac{dX_2}{d\tau}}{\frac{dX_1}{d\tau}} \quad (4.31)$$

with minimal and maximal α differing by less than π (i.e., the track changes direction by less than 180°), then all intersections of the track's normals must lie

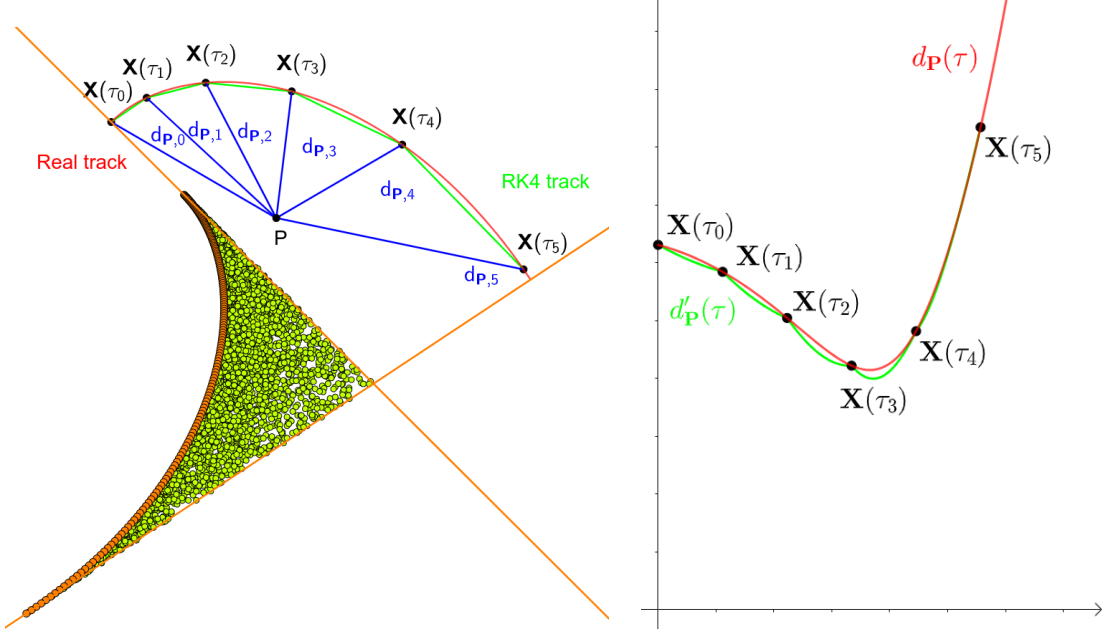


Figure 4.6: An example track (red) with a polygonal chain approximation (green, representing a RK4 simulation). The distance of the point \mathbf{P} from the chain is found using a binary search among the distances to the vertices $d_{\mathbf{P}}(\tau_i)$ (blue) and subsequently calculating the distance to segments neighboring the found vertex (thus finding the minimum of the function $d'_{\mathbf{P}}(\tau)$, function $d_{\mathbf{P}}(\tau)$ for the actual track is showed for reference). This approach works if the condition 4.28 is satisfied, which is not the case for a point from the green area bordered by the normals at endpoints and the evolute of the track (orange).

in an area bordered by the evolute and the normals at the beginning and the end of the curve (from their intersection with the evolute to their mutual intersection, see Figs. 4.6 and 4.7). Together, these three boundaries define a closed shape that will lie outside of the OFTPC for a typical track in our detector³.

With the assumption 4.28, we can find the segment on the RK4 track with the lowest distance to a given point \mathbf{P} using a binary search algorithm. Let the distance of the point from the n -th vertex be $d_{\mathbf{P},n} = d_{\mathbf{P}}(\tau_n)$. Then the difference $\Delta d_{\mathbf{P},n} = d_{\mathbf{P},n} - d_{\mathbf{P},n-1}$ satisfies

$$\begin{aligned}\Delta d_{\mathbf{P},n} &< 0 \quad \forall n \text{ such that } \tau_n < \tau_{\min}, \\ \Delta d_{\mathbf{P},n} &> 0 \quad \forall n \text{ such that } \tau_{n-1} > \tau_{\min}.\end{aligned}\tag{4.32}$$

Therefore, we can search for the segment containing $d_{\mathbf{P},\min} = d_{\mathbf{P}}(\tau_{\min})$ with binary search starting with $\Delta d_{\mathbf{P},1}$ and $\Delta d_{\mathbf{P},N}$, then calculate the difference $\Delta d_{\mathbf{P},m}$ for the middle index $m = \left\lfloor \frac{N+1}{2} \right\rfloor$. If $\Delta d_{\mathbf{P},m} > 0$ (minor bug in the implementation – if the value for the maximal index is negative, it shouldn't change anything), we can replace the higher index with m , otherwise we replace the lower index. The search stops when the difference between the minimal and maximal index is one. Would it be better if they were the same (maybe not)? Then the minimal

³The smallest anticipated radius of curvature is 39 cm for an electron or positron with a kinetic energy 3 MeV in a 0.3 T magnetic field. All points in the exclusion area must be farther from the track and therefore outside the OFTPC.

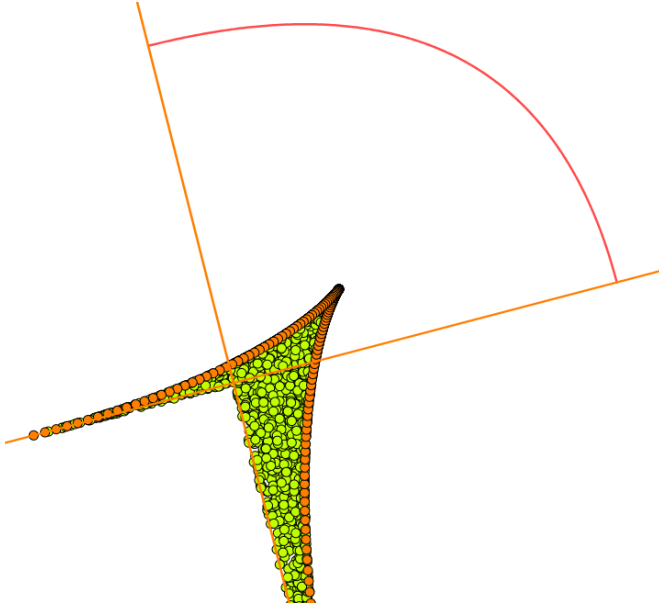


Figure 4.7: An exclusion area (green) of a track (red) bordered by its evolute and the normals at endpoints (orange), where the assumption 4.28 is violated. Unlike the track in Fig. 4.6, this track has a minimal curvature point in the middle, corresponding to the cusp on its evolute.

value is $d_{P,n-1}$ or $d_{P,N}$ and we can take the minimum of the distances from the two segments connected to $n - 1$. Currently taking the maximal index (and starting at $N - 2$ maximal index $\leftrightarrow N - 1$ -th point), this should be equivalent, since either $\Delta d_{P,\max} > 0$ (in the code is equivalent to max-1 here) or we are at $N - 1$. The minimum of the two distances still taken.

Same details with MIGRAD etc. as previously.

4.3.1 Testing on a microscopic sample

The Runge-Kutta fit together with the 3D circle-and-lines pre-fit was tested on a sample of tracks simulated using the microscopic simulation described in Section 2.1. At first, few tracks with randomized initial parameters (same as the Runge-Kutta sample in Section 2.2.1) were generated for preliminary testing. Later, a sample with a grid-like distribution of track parameters was generated (see Section 2.1.2 for details).

Initial parameters of the HEED track (also should be in the first testing track). Initial parameters set in the circle fit (if electron set alpha one way, otherwise other way) and parameter bounds.

Conclusion

1182 Here or at the end of each section. Something about the future of this work?

1183

1184 Notes

1185 General notes about the thesis:

- 1186 • Check that all of the classes and other code are marked the same way in
1187 the text. I used italics somewhere, could use different font for this instead.
- 1188 • Check unbreakable space in front of articles. Remove excessive article usage
1189 with proper nouns.
- 1190 • Currently using margins for single-sided printing (bigger on the left side).
- 1191 • Check that present tense is used
- 1192 • Active vs passive voice usage
- 1193 • American English quotation marks (") instead of British English (').
- 1194 • Some of the overfull hbox warnings might change if duplex printing is used
1195 (they generate black rectangles on the edge of the page), leaving them be
1196 for now
- 1197 • Check nobreakdash usage (is it always necessary)
- 1198 • Check capitalized references (e.g., Figure, Section, Equation)
- 1199 • Check $\backslash(...\backslash)$ math mode instead of $\$...$$. (actually unlike $\backslash[...\backslash]$ math mode,
1200 there is apparently no real benefit to this clumsy syntax)
- 1201 • Use siunitx package to ensure correct formatting, physics package for deriva-
1202 tives.
- 1203 • Check other stuff that's written in the MFF UK template. Apparently it
1204 has since been updated and there are some differences (check for them).
- 1205 • Check correct subscripts in equation (italics vs no italics)
- 1206 • Consistent bold marking of points/vectors
- 1207 • Correct footnotes (capital letters, etc.).
- 1208 • Might have to mention GeoGebra as per the non-commercial license agree-
1209 ment (Made with GeoGebra®) – maybe put it into acknowledgments next
1210 to the MetaCentrum credit? And list all of the figures where GeoGebra was
1211 used?
- 1212 • Maybe make some section outside of References specifically for literature?
1213 (such as the old CERN TPC review, ATOMKI review is currently not
1214 mentioned, not sure if some Wikipedia articles should get a mention or how
1215 do these things work)
- 1216 • Consistent use of `bm` vs `mathbf`

- Consistent use of $\bar{\mathcal{M}}$ instead of \mathcal{M} when talking about the map of the means (so most of the time)
 - Proper equation numbering when deriving a relation
 - Hugo should be mentioned somewhere in the title pages probably?
 - Consistent itemize/enumerate style (namely spacing) that looks good (ideally set by some macro? maybe the new MFF UK template will solve this?)
 - Consistent gas mixture notation (e.g., 90:10 Ar:CO₂). Maybe mention at the beginning that it is a molar ratio.
 - Labels of figures and tables – maybe in bold? Abbreviated?
 - Check graph labels, make them bigger if needed.
 - "The map" can be viewed as a mapping between spaces or just as a coordinate transform.
 - Maybe switch to cleverref.
 - siunitx qty not SI
 - Correct em dash?
 - In the future, it might be useful to save pictures as tex files whenever possible and using siunitx for the labels
- 1234 Random notes:
- Terminology consistency – ionization/primary/secondary electrons
 - Consistent TPC vs OFTPC acronym usage in the text or individual chapters.
 - Only electrons that start and end in the sector closer than 0.5 cm are used for reconstruction (newest version).
 - Attachment, Penning transfer and secondary ionization not considered in the microscopic simulation.
 - Suspicious artifacts of trilinear interpolation in Fig. 1.14. **Fixed – integers instead of doubles in the implementation, influenced reconstruction SIGNIFICANTLY (but not simulation).**
 - Profiling of the reconstruction!!!! Find out what's taking the most time (probably Runge-Kutta integration which the fit calls a lot). Could gradually decrease the step size to refine the fit instead of making it small right away (arbitrarily small – the effect of this was never tested). This could take some time to do properly (find a profiler or make profiling macros).
 - Slow drift velocity good for z reconstruction, too low leads to recombination
 - Could add link to the GitHub repository, mention CMake? Details about simulating on MetaCentrum?
 - The first used track had 8 MeV momentum $p = \gamma mv$ (not kinetic energy $E_{\text{kin}} = (\gamma - 1)mc^2 = \sqrt{p^2c^2 + m^2c^4} - mc^2 \approx 7.5$ MeV)

- Maybe cite Garfield++ user manual instead?
- Using TRandom3 for random number generation.
- Does the RK fit error correlate with the actual error?
- Some Garfield settings in micro track generation probably not mentioned
- one-to-one only means injection (not bijection)? Make sure correct terminology is used.

1261 Future

1262 Things planned for the future:

- Testing the reconstruction algorithm by measuring real particles with a known energy distribution (at first just laser, muons?).
- The **Fast Simulation with Ionization Electron Map** is planned for the future. It will use the HEED program [44] to simulate the primary particle and the Ionization Electron Map (see Section 3.2) to simulate the drift of secondary electrons. It should be significantly faster than the Microscopic Simulation but offer comparable precision since it will rely on an already simulated drift map. (Primary track simulated in HEED. Readout parameters by interpolating the map. Diffusion from the map for randomization.) Currently more or less implemented, but it turns out that the initial energy of ionization electrons cannot be discarded.
- Account for GEM, delta electrons, ...
- Likelihood approach instead of least squares (if it improves the reconstruction significantly), we should at least use a better method than taking the center of the TPC bin.
- More detailed electric field simulation (if needed, GEM will have more complex field, some irregularities in the field should be considered)
- Account for the triggering in MWPC/TPX3 (particle travels from TPX3 to MWPC basically immediately – fraction of a nanosecond so there should be no significant difference)

1283

1284 Likelihood - inverse map

1285 If we wanted to further improve this procedure, taking into account the whole
 1286 map \mathcal{M} , we could make an "inverse map" from \mathcal{R} to distributions on \mathcal{D} . We could
 1287 achieve this by taking the normalized probability density of an electron with initial
 1288 coordinates (x, y, z) having readout coordinates (x', y', t) . If we fix (x', y', t) , we
 1289 get an unnormalized probability density $f(x, y, z) = \mathcal{M}_{(x,y,z)}(x', y', t)$ (assuming
 1290 that all initial coordinates are a priori equally likely). This could potentially
 1291 improve the discrete reconstruction if we take the mean value of this probability

1292 density across the pad and time bin

$$f_{\text{pad, bin}}(x, y, z) = \frac{1}{A_{\text{pad}} \Delta t_{\text{bin}}} \int_{\text{pad, bin}} \mathcal{M}_{(x,y,z)}(x', y', t) dx' dy' dt \quad (4.33)$$

1293 and using it for a likelihood fit instead of using least squares. This still assumes
1294 that all initial coordinates are equally likely which is clearly not the case for
1295 a primary particle track. In the future, we could even use the fast track simulation
1296 with the map (should be possible to make around 1000 tracks per minute per core
1297 with current settings), create a big set of tracks with reasonable parameters and
1298 use these to get an approximation of the probability distribution of the detector
1299 response. Some approximations would be necessary when interpreting the data to
1300 decrease the degrees of freedom of this distribution (we would have to pick a set of
1301 parameters and assume that some of them are independent). This could give us
1302 an idea about the best achievable resolution (how significantly will the detector
1303 response differ for a given change in energy). If the difference is significant, we
1304 could try to further improve the likelihood fit.

Bibliography

1. *Garfield++* [<https://garfieldpp.web.cern.ch/garfieldpp/>]. [N.d.]. Accessed: 2023-05-18.
2. BRUN, Rene; RADEMAKERS, Fons. Root — An Object Oriented Data Analysis Framework. *Nucl. Instrum. Methods Phys. Res. Sect. A: Accel. Spectrom. Detect. Assoc. Equip.* 1997, vol. 389, no. 1–2, pp. 81–86. Available from DOI: 10.1016/s0168-9002(97)00048-x. Proceedings AIHENP'96 Workshop, Lausanne, Sep. 1996, See also <https://root.cern/>, Paper published in the Linux Journal, Issue 51, July 1998.
3. *About MetaCentrum* [<https://metavo.metacentrum.cz/en/about/index.html>]. 2023. Accessed: 2024-11-27.
4. ROSE, M. E. Internal Pair Formation. *Phys. Rev.* 1949, vol. 76, pp. 678–681. Available from DOI: 10.1103/PhysRev.76.678.
5. ESSIG, R. et al. *Dark Sectors and New, Light, Weakly-Coupled Particles*. 2013. Available from arXiv: 1311.0029 [hep-ph].
6. DE BOER, F.W.N. et al. A deviation in internal pair conversion. *Phys. Lett. B*. 1996, vol. 388, no. 2, pp. 235–240. ISSN 0370-2693. Available from DOI: [https://doi.org/10.1016/S0370-2693\(96\)01311-1](https://doi.org/10.1016/S0370-2693(96)01311-1).
7. BOER, F W N de et al. Excess in nuclear pairs near 9 MeV/ invariant mass. *J. Phys. G: Nucl. Part. Phys.* 1997, vol. 23, no. 11, p. L85. Available from DOI: 10.1088/0954-3899/23/11/001.
8. BOER, F W N de et al. Further search for a neutral boson with a mass around 9 MeV/c². *J. Phys. G: Nucl. Part. Phys.* 2001, vol. 27, no. 4, p. L29. Available from DOI: 10.1088/0954-3899/27/4/102.
9. VITÉZ, Attila et al. Anomalous Internal Pair Creation in ⁸Be as a Signature of the Decay of a New Particle. *Acta Phys. Pol. B - ACTA PHYS POL B*. 2008, vol. 39, p. 483.
10. KRASZNAHORKAY, A. et al. Searching for a light neutral axial-vector boson in isoscalar nuclear transitions. *Frascati Phys. Ser.* 2012, vol. 56, p. 86.
11. KRASZNAHORKAY, A. J. et al. Observation of Anomalous Internal Pair Creation in ⁸Be: A Possible Indication of a Light, Neutral Boson. *Phys. Rev. Lett.* 2016, vol. 116, no. 4. ISSN 1079-7114. Available from DOI: 10.1103/physrevlett.116.042501.
12. TILLEY, D.R. et al. Energy levels of light nuclei A=8,9,10. *Nucl. Phys. A*. 2004, vol. 745, no. 3, pp. 155–362. ISSN 0375-9474. Available from DOI: <https://doi.org/10.1016/j.nuclphysa.2004.09.059>.
13. SAS, N. J. et al. *Observation of the X17 anomaly in the ⁷Li(p,e⁺e⁻)⁸Be direct proton-capture reaction*. 2022. Available from arXiv: 2205.07744 [nucl-ex].
14. KRASZNAHORKAY, A. J. et al. New anomaly observed in ⁴He supports the existence of the hypothetical X17 particle. *Phys. Rev. C*. 2021, vol. 104, no. 4. ISSN 2469-9993. Available from DOI: 10.1103/physrevc.104.044003.

- 1347 15. TILLEY, D.R. et al. Energy levels of light nuclei A = 4. *Nucl. Phys. A*.
 1348 1992, vol. 541, no. 1, pp. 1–104. ISSN 0375-9474. Available from DOI: [https://doi.org/10.1016/0375-9474\(92\)90635-W](https://doi.org/10.1016/0375-9474(92)90635-W).
- 1350 16. KRASZNAHORKAY, A. J. et al. New anomaly observed in ^{12}C supports the
 1351 existence and the vector character of the hypothetical X17 boson. *Phys. Rev.*
 1352 *C*. 2022, vol. 106, p. L061601. Available from DOI: 10.1103/PhysRevC.106.
 1353 L061601.
- 1354 17. AJZENBERG-SELOVE, F. Energy levels of light nuclei A = 11,12. *Nucl. Phys.*
 1355 *A*. 1990, vol. 506, no. 1, pp. 1–158. ISSN 0375-9474. Available from DOI:
 1356 [https://doi.org/10.1016/0375-9474\(90\)90271-M](https://doi.org/10.1016/0375-9474(90)90271-M).
- 1357 18. KÁLMÁN, Péter; KESZTHELYI, Tamás. Anomalous internal pair creation.
 1358 *The Eur. Phys. J. A*. 2020, vol. 56. Available from DOI: 10.1140/epja/
 1359 s10050-020-00202-z.
- 1360 19. ALEKSEJEVS, A. et al. *A Standard Model Explanation for the "ATOMKI*
 1361 *Anomaly*". 2021. Available from arXiv: 2102.01127 [hep-ph].
- 1362 20. FENG, Jonathan L. et al. Protophobic Fifth-Force Interpretation of the Ob-
 1363 served Anomaly in ^8Be Nuclear Transitions. *Phys. Rev. Lett.* 2016, vol. 117,
 1364 p. 071803. Available from DOI: 10.1103/PhysRevLett.117.071803.
- 1365 21. ANH, Tran The et al. Checking the 8Be Anomaly with a Two-Arm Electron
 1366 Positron Pair Spectrometer. *Universe*. 2024, vol. 10, no. 4, p. 168. ISSN 2218-
 1367 1997. Available from DOI: 10.3390/universe10040168.
- 1368 22. ABRAAMYAN, Kh. U. et al. *Observation of structures at ~ 17 and $\sim 38 \text{ MeV}/c^2$*
 1369 *in the $\gamma\gamma$ invariant mass spectra in pC , dC , and dCu collisions at p_{lab} of a*
 1370 *few GeV/c per nucleon*. 2023. Available from arXiv: 2311.18632 [hep-ex].
- 1371 23. THE MEG II COLLABORATION et al. *Search for the X17 particle in $^7\text{Li}(p, e^+e^-)^8\text{Be}$*
 1372 *processes with the MEG II detector*. 2024. Available from arXiv: 2411.07994
 1373 [nucl-ex].
- 1374 24. HILKE, H J. Time Projection Chambers. *Rep. Prog. Phys.* 2010, vol. 73, no.
 1375 11, p. 116201. Available from DOI: {10.1088/0034-4885/73/11/116201}.
- 1376 25. NAVAS, S. et al. Review of particle physics. *Phys. Rev. D*. 2024, vol. 110,
 1377 no. 3, p. 030001. Available from DOI: 10.1103/PhysRevD.110.030001.
- 1378 26. ABED ABUD, Adam et al. A Gaseous Argon-Based Near Detector to En-
 1379 hance the Physics Capabilities of DUNE. 2022. Available from DOI: 10.
 1380 48550/arXiv.2203.06281.
- 1381 27. AIHARA, H. et al. Spatial Resolution of the PEP-4 Time Projection Cham-
 1382 ber. *IEEE Trans. on Nucl. Sci.* 1983, vol. 30, no. 1, pp. 76–81. Available
 1383 from DOI: 10.1109/TNS.1983.4332223.
- 1384 28. LOKEN, Stewart C. et al. Performance of the Signal Processing System for
 1385 the Time Projection Chamber. *IEEE Trans. on Nucl. Sci.* 1983, vol. 30, no.
 1386 1, pp. 162–166. Available from DOI: 10.1109/TNS.1983.4332243.
- 1387 29. COWAN, G. D. *Inclusive π^\pm , K^\pm , and p , \bar{p} production in e^+e^- annihilation*
 1388 *at $\sqrt{s} = 29 \text{ GeV}$* . 1988. Available from DOI: 10.2172/5188194. Lawrence
 1389 Berkeley National Lab. (LBNL), Berkeley, CA (United States).

- 1390 30. ALME, J. et al. The ALICE TPC, a large 3-dimensional tracking device
1391 with fast readout for ultra-high multiplicity events. *Nucl. Instrum. Methods*
1392 *Phys. Res. Sect. A: Accel. Spectrom. Detect. Assoc. Equip.* 2010, vol. 622,
1393 no. 1, pp. 316–367. ISSN 0168-9002. Available from DOI: <https://doi.org/10.1016/j.nima.2010.04.042>.
- 1394
- 1395 31. HAUER, Philip. The upgraded ALICE TPC. *Nucl. Instrum. Methods Phys.*
1396 *Res. Sect. A: Accel. Spectrom. Detect. Assoc. Equip.* 2022, vol. 1039, p. 167023. ISSN
1397 0168-9002. Available from DOI: <https://doi.org/10.1016/j.nima.2022.167023>.
- 1398
- 1399 32. DI MAURO, A. Particle identification methods other than RICH. *Nucl. Instrum.*
1400 *Methods Phys. Res. Sect. A: Accel. Spectrom. Detect. Assoc. Equip.* 2020, vol. 952, p. 162124. ISSN 0168-9002. Available from DOI: <https://doi.org/10.1016/j.nima.2019.04.078>. 10th International Workshop on
1401 Ring Imaging Cherenkov Detectors (RICH 2018).
- 1402
- 1403
- 1404 33. ADAMOVÁ, D. et al. The CERES/NA45 radial drift Time Projection Chamber.
1405 *Nucl. Instrum. Methods Phys. Res. Sect. A: Accel. Spectrom. Detect.*
1406 *Assoc. Equip.* 2008, vol. 593, no. 3, pp. 203–231. ISSN 0168-9002. Available
1407 from DOI: [10.1016/j.nima.2008.04.056](https://doi.org/10.1016/j.nima.2008.04.056).
- 1408
- 1409 34. BIAGI, S.F. Monte Carlo simulation of electron drift and diffusion in count-
1410 ing gases under the influence of electric and magnetic fields. *Nucl. Instrum.*
1411 *Methods Phys. Res. Sect. A: Accel. Spectrom. Detect. Assoc. Equip.* 1999,
1412 vol. 421, no. 1, pp. 234–240. ISSN 0168-9002. Available from DOI: [https://doi.org/10.1016/S0168-9002\(98\)01233-9](https://doi.org/10.1016/S0168-9002(98)01233-9).
- 1413
- 1414 35. ALBAYRAK, I. et al. Design, construction, and performance of the GEM
1415 based radial time projection chamber for the BONuS12 experiment with
1416 CLAS12. *Nucl. Instrum. Methods Phys. Res. Sect. A: Accel. Spectrom. De-*
1417 *tect. Assoc. Equip.* 2024, vol. 1062, p. 169190. ISSN 0168-9002. Available from
DOI: <https://doi.org/10.1016/j.nima.2024.169190>.
- 1418
- 1419 36. ANDERSON, E. et al. Observation of the effect of gravity on the motion of
1420 antimatter. *Nature*. 2023, vol. 621, pp. 716–722. Available from DOI: [10.1038/s41586-023-06527-1](https://doi.org/10.1038/s41586-023-06527-1).
- 1421
- 1422 37. Design of a Radial TPC for Antihydrogen Gravity Measurement with ALPHA-
1423 g. In: *Proceedings of the 12th International Conference on Low Energy An-*
1424 *tiproton Physics (LEAP2016)*. [N.d.]. Available from DOI: [10.7566/JPSCP.18.011015](https://doi.org/10.7566/JPSCP.18.011015).
- 1425
- 1426 38. CAPRA, A. Antihydrogen annihilation detection: the ALPHA-g radial TPC.
1427 *PoS*. 2025, vol. EXA-LEAP2024, p. 063. Available from DOI: [10.22323/1.480.0063](https://doi.org/10.22323/1.480.0063).
- 1428
- 1429 39. WIECHULA, Jens; CHRISTIANSEN, Peter. *The ALICE Time Projection Cham-*
1430 *ber* [https://www.hep.lu.se/staff/christiansen/teaching/spring_2013/the_alice_tpc.pdf]. 2013. Slides credited to J. Wiechula; hosted on
1431 Lund University website.

- 1432 40. HILDÉN, T. et al. Optical quality assurance of GEM foils. *Nucl. Instrum.*
1433 *Methods Phys. Res. Sect. A: Accel. Spectrom. Detect. Assoc. Equip.* 2015,
1434 vol. 770, pp. 113–122. ISSN 0168-9002. Available from DOI: 10.1016/j.nima.2014.10.015.
- 1435
- 1436 41. AHMED, Misbah Uddin. *Simulation of the electron and ion movement through a 4-GEM stack*. 2021. Institut für Kernphysik.
- 1437
- 1438 42. MARMELAD. *3D interpolation2.svg*. 2025. Available also from: https://commons.wikimedia.org/wiki/File:3D_interpolation2.svg. Licensed
1439 under CC BY-SA 3.0 (<https://creativecommons.org/licenses/by-sa/3.0/legalcode>). Accessed: 9-April-2025.
- 1440
- 1441
- 1442 43. CMGLEE. *Trilinear interpolation visualisation*. 2025. Available also from:
1443 https://commons.wikimedia.org/wiki/File:Trilinear_interpolation_visualisation.svg. Licensed under CC BY-SA 3.0 (<https://creativecommons.org/licenses/by-sa/3.0/legalcode>). Accessed: 26-March-2025.
- 1444
- 1445
- 1446 44. SMIRNOV, I.B. Modeling of ionization produced by fast charged particles in
1447 gases. *Nucl. Instrum. Methods Phys. Res. Sect. A: Accel. Spectrom. Detect.*
1448 *Assoc. Equip.* 2005, vol. 554, no. 1, pp. 474–493. ISSN 0168-9002. Available
1449 from DOI: <https://doi.org/10.1016/j.nima.2005.08.064>.
- 1450
- 1451 45. SCOTT, DAVID W. On optimal and data-based histograms. *Biometrika*.
1452 1979, vol. 66, no. 3, pp. 605–610. ISSN 0006-3444. Available from DOI: 10.1093/biomet/66.3.605.
- 1453

1454 **Acknowledgments:** Computational resources were provided by the e-INFRA
1455 CZ project (ID:90254), supported by the Ministry of Education, Youth and Sports
of the Czech Republic. **Figures that were drawn with GeoGebra. Maybe grant?**

List of Figures

1457	0.1	The ATOMKI anomalous IPC measured for different nuclei.	5
1458	0.2	Results from the Hanoi spectrometer – angular e^+e^- pair correlations measured in the ${}^7\text{Li}(p, e^+e^-){}^8\text{Be}$ reaction at $E_p = 1225$ keV [21].	6
1459	0.3	Results from the MEG II experiments – angular correlation of e^+e^- pairs with $E_{\text{sum}} \in [16, 20]$ MeV measured in the ${}^7\text{Li}(p, e^+e^-){}^8\text{Be}$ reaction with proton beam energies 500 and 1080 keV. The 500 keV dataset is fitted with Monte Carlo of both the IPC deexcitation and the EPC produced by gammas [23].	7
1460	0.4	Schematics of the detector at the Van der Graaff facility at IEAP CTU (ref).	7
1461	1.1	Particle identification in the PEP-4 TPC at SLAC based on the energy loss per distance $\frac{dE}{dx}$ in the 80:20 Ar:CH ₄ filling at 8.5 atm pressure [26]. The reference doesn't point to the original PEP-4 article because this adapted version of the original picture that they used in the DUNE article looks better.	9
1462	1.2	Schematic view of the PEP-4 TPC [28]. A charged particle produced in a collision in the beam pipe creates a spiral ionization track in the magnetic field. The central cathode then accelerates ionization electrons towards the endcap anode wires where they are multiplied and read out. A TPC sector with a detailed view of one of the pad rows is shown on the right [29].	12
1463	1.3	Schematic view of the ALICE TPC [31]. The readout at each endcap is divided into 18 sectors, each subdivided into an Inner Readout Chamber (IROC) with one GEM stack and Outer Readout Chamber (OROC) with three GEM stacks. A visualization of a GEM stack is on the right [32].	13
1464	1.4	Experimental setup of the CERES/NA45 experiment with two Ring Imaging Cherenkov Counters (RICHs) on the left and a rTPC on the right. The magnetic field (red) is generated by two solenoidal coils (blue) with opposite polarity. Produced ionization electrons drift outward radially towards the readout chamber (yellow) [33].	14
1465	1.5	Cross section of a CERES/NA45 readout MWPC. The wires are stretched in the azimuthal direction above the pad plane. The gating grid controls the passage of electrons and ions. [33].	14
1466	1.6	Schematic view of the BONuS12 rTPC [35].	15
1467	1.7	Schematic view of the ALPHA-g detector [37].	16
1468	1.8	Schematic view of the ALICE MWPC readout (working principle) [39].	17
1469	1.9	Gas Electron Multiplier (GEM).	18
1470	1.10	Garfield simulation of an avalanche in a GEM hole [41]. An incoming electron (orange) is accelerated in the strong electric field of the GEM and causes further ionization multiplying the number of free electrons (orange). Most of the produced cations (red) are captured by the GEM cathode.	18
1471	1.11	MICRO-MEsh GAseous Structure (Micromegas) [25].	19

1501	1.12 Schematics of the first sector OFTPC with detector space coordinates.	21
1502		
1503	1.13 Pad layout of the OFTPC and its parameters. Pads 102, 124 and 127 are irregular, the rest has the same dimensions.	22
1504		
1505	1.14 Magnetic field simulation results. The OFTPC volume and the vacuum tube are marked with black lines, the magnets are marked with red lines. The coordinates of the magnets from the CAD drawing seem to be 9/10 of the ones from the magnetic simulation (fixed, the magnetic simulation parameters are off).	23
1506		
1507		
1508		
1509		
1510	1.15 Visualization of trilinear interpolation as a composition of linear interpolations (inspired by [42]). We want to interpolate the value in the red point C . First we interpolate between the four pairs of blue points sharing the last two indices along the x -axis (Eq. 1.15), then between the two pairs of the resulting green points along the y -axis (Eq. 1.16) and finally between the two resulting orange points along the z -axis to get the final red value (Eq. 1.17).	24
1511		
1512		
1513		
1514		
1515		
1516		
1517	1.16 Geometric interpretation of trilinear interpolation as expressed in Equation 1.19. The colored dots represent the values in given points and the colored boxes represent the volume in the opposite corner by which the corresponding values are multiplied. The black dot represents the interpolated value which is multiplied by the entire volume [43].	25
1518		
1519		
1520		
1521		
1522		
1523	2.1 Comparison of drift lines for two different gas mixtures 90:10 and 70:30 Ar:CO ₂ . The electron track is marked in black, the drift lines of the ionization electrons are marked in orange. In this example, we assume a larger OFTPC volume with readout at $z = 8$ cm.	28
1524		
1525		
1526		
1527	2.2 A visualization of a set of tracks from the grid-like testing sample with the same kinetic energy.	29
1528		
1529	2.3 A comparison of the HEED track from the microscopic simulation in Section 2.1.1 with a Runge-Kutta track with the same initial parameters and $\tau_{\text{step}} = 0.1$ ps (reducing the step further doesn't make a visible difference). In the view of the tracks on the left, the distance of the HEED ionization electrons from the RK4 track is exaggerated 1000 \times . On the right, the dependence of the HEED electrons residuals (i.e., their shortest distance to the RK4 track) on their z -coordinate is shown. The images look the same even for 100,000x smaller step, so the residuals are a result of something that HEED does (maybe a different interpolation technique for the magnetic field? the pattern looks similar for two different tracks so it can't be scattering).	31
1530		
1531		
1532		
1533		
1534		
1535		
1536		
1537		
1538		
1539		
1540		
1541	3.1 Linear fit of the drift time t dependence on the distance to the readout $d_r = 8$ cm – z for the ionization electrons in 90:10 (left) and 70:30 (right) Ar:CO ₂ gas composition. Only electrons inside the TPC (red) are fitted. The parameters are $v_d = 3.39$ cm/ μ s, $d_0 = -0.41$ cm for 90:10, and $v_d = 0.939$ cm/ μ s, $d_0 = -0.11$ cm for 70:30 Ar:CO ₂	33
1542		
1543		
1544		
1545		
1546		

1547	3.2 Reconstruction (black) of the starting position of ionization elec-	
1548	trons (red) using parameters obtained from the fit (Fig. 3.1). Two	
1549	gas compositions 90:10 (left) and 70:30 Ar:CO ₂ (right) are compared.	34
1550	3.3 Comparison of residuals (i.e., the distance from the reconstructed	
1551	point to the simulated ionization electron starting point) dependence	
1552	on x for two gas mixtures 90:10 (red) and 70:30 Ar:CO ₂	
1553	(blue).	34
1554	3.4 A 3D visualization of the mapping of means $\bar{\mathcal{M}}$ for the 90:10	
1555	Ar:CO ₂ gas. A regular grid \mathbb{G} with $l = 1$ cm in the detector space	
1556	is mapped to an irregular grid $\mathbb{G}^{-1} \equiv \bar{\mathcal{M}}(\mathbb{G})$ in the readout space.	35
1557	3.5 A test of the 90:10 Ar:CO ₂ map simulation with spacing $l = 1.5$ cm.	
1558	The resulting drift lines of evenly spaced electrons are displayed in	
1559	orange.	36
1560	3.6 Dependence of the drift times of the simulated map $\bar{\mathcal{M}}$ on the	
1561	z -coordinate. Two gas mixtures 90:10 (left) and 70:30 Ar:CO ₂	
1562	(right) are compared. The spread is caused by varying Lorentz	
1563	angles.	37
1564	3.7 The $x't$ projection of the $\mathcal{M}(\mathbb{G}_{y=0})$ mapping of a part of the regu-	
1565	lar grid \mathbb{G} . The means $\bar{\mathcal{M}}(\mathbb{G}_{y=0})$ are marked with red crosses, and	
1566	the diffusion error is denoted by black 95% confidence error ellipses	
1567	computed from the diagonalized covariance matrices $\mathcal{M}_{\Sigma}(\mathbb{G}_{y=0})$.	
1568	Two gas mixtures 90:10 (left) and 70:30 Ar:CO ₂ (right) are com-	
1569	pared. The first mixture shows differences of t for electrons with	
1570	same initial z but different initial x . For the second mixture, these	
1571	differences are negligible in comparison with the diffusion.	38
1572	3.8 The regular grid \mathbb{G} projected by the mapping $\bar{\mathcal{M}}$ from the detector	
1573	space onto the $x'y'$ plane (t is not plotted). Layers with lower	
1574	z -coordinate (i.e., further away from the readout) are displayed	
1575	with darker colors. The OFTPC volume is marked with black	
1576	lines. Two gas mixtures 90:10 (left) and 70:30 Ar:CO ₂ (right) are	
1577	compared.	38
1578	3.9 The $\mathcal{M}(\mathbb{G}_{-8})$ mapping of the bottom ($z = -8$ cm) layer \mathbb{G}_{-8} of the	
1579	regular grid $\mathbb{G} \subset \mathcal{D}$. It includes both the mapping of means $\bar{\mathcal{M}}$ and	
1580	of covariances \mathcal{M}_{Σ} . Individual electrons from the map simulation	
1581	are marked with red dots. Two gas mixtures 90:10 (left) and 70:30	
1582	Ar:CO ₂ (right) are compared.	39
1583	3.10 The readout coordinate x' for points on the grid $\mathbb{G}_{y=0}$ plotted	
1584	against their initial coordinate z . The means are marked with red	
1585	crosses, the diffusion in x' is denoted by standard error bars. Two	
1586	gas mixtures 90:10 (left) and 70:30 Ar:CO ₂ (right) are compared.	39
1587	3.11 Selection of the points for interpolation. Create better images; use	
1588	the explanation interpolation vs. extrapolation strange property.	
1589	Solution 2 probably does not make much sense.	43
1590	3.12 Reconstruction (black) of the starting position of ionization elec-	
1591	trons (red) using the inversion of the ionization electron map. Two	
1592	gas compositions 90:10 (left) and 70:30 Ar:CO ₂ (right) are compared.	44

1593	3.13 Comparison of residuals from the RASD (black) and map inversion (red) reconstruction methods. Tracks in two different gas compositions 90:10 (left) and 70:30 Ar:CO ₂ (right) are compared.	44
1594		
1595		
1596	3.14 Map inversion reconstruction residuals (for the individual coordinates and total) of the testing track in 90:10 Ar:CO ₂ gas mixture.	45
1597		
1598	3.15 Map inversion reconstruction residuals (for the individual coordinates and total) of the testing track in 70:30 Ar:CO ₂ gas mixture.	45
1599		
1600	4.1 Example of a fitted reconstructed track. Swap for better image.	47
1601		
1602	4.2 First attempt at a track reconstruction using only the drift velocity. Spline energy reconstruction attempt. Swap for better image(s) – subfigure environment, correct coordinates.	49
1603		
1604	4.3 First attempt at a track reconstruction using only the drift velocity. Circle and Lines Fit in 2D. Swap for better image, correct coordinates. Bias should be described in the previous chapter, not here.	51
1605		
1606		
1607		
1608	4.4 Visualization of the 3D geometry of the Circle and Lines Fit and its parameters.	52
1609		
1610	4.5 Demonstration of the convexity of the distance function $d(\alpha)$ for a circular track (see Equation 4.29).	55
1611		
1612	4.6 An example track (red) with a polygonal chain approximation (green, representing a RK4 simulation). The distance of the point \mathbf{P} from the chain is found using a binary search among the distances to the vertices $d_{\mathbf{P}}(\tau_i)$ (blue) and subsequently calculating the distance to segments neighboring the found vertex (thus finding the minimum of the function $d''_{\mathbf{P}}(\tau)$, function $d_{\mathbf{P}}(\tau)$ for the actual track is showed for reference). This approach works if the condition 4.28 is satisfied, which is not the case for a point from the green area bordered by the normals at endpoints and the evolute of the track (orange).	56
1613		
1614		
1615		
1616		
1617		
1618		
1619		
1620		
1621		
1622	4.7 An exclusion area (green) of a track (red) bordered by its evolute and the normals at endpoints (orange), where the assumption 4.28 is violated. Unlike the track in Fig. 4.6, this track has a minimal curvature point in the middle, corresponding to the cusp on its evolute.	57
1623		
1624		
1625		
1626		

List of Tables

1627	3.1 Comparison of parameters of two map simulations.	36
------	--	----

¹⁶²⁹ List of Abbreviations

- ¹⁶³⁰ **ALPHA** Antihydrogen Laser Physics Apparatus
- ¹⁶³¹ **BONuS12** Barely Off-shell NeUtron Structure 12 GeV
- ¹⁶³² **GEM** Gas Electron Multiplier
- ¹⁶³³ **HEED** High Energy Electro-Dynamics
- ¹⁶³⁴ **IEAP CTU** Institute of Experimental and Applied Physics, Czech Technical
¹⁶³⁵ University in Prague
- ¹⁶³⁶ **IPC** Internal Pair Creation
- ¹⁶³⁷ **EPC** External Pair Creation
- ¹⁶³⁸ **LArTPC** Liquid Argon TPC
- ¹⁶³⁹ **Micromegas** MICRO-MEsh Gaseous Structure
- ¹⁶⁴⁰ **MPGD** Micro-Pattern Gaseous Detector
- ¹⁶⁴¹ **MWPC** Multi-Wire Proportional Chamber
- ¹⁶⁴² **OFTPC** Orthogonal Fields TPC
- ¹⁶⁴³ **PCB** Printed Circuit Board
- ¹⁶⁴⁴ **RASD** Reconstruction Assuming Steady Drift
- ¹⁶⁴⁵ **RICH** Ring Imaging Cherenkov Counter
- ¹⁶⁴⁶ **RK4** Runge-Kutta 4th order
- ¹⁶⁴⁷ **RPC** Resistive Plate Chamber
- ¹⁶⁴⁸ **RPWELL** Resistive Plate WELL
- ¹⁶⁴⁹ **rTPC** radial-drift TPC
- ¹⁶⁵⁰ **THGEM** THick GEM
- ¹⁶⁵¹ **ToA** time-of-arrival
- ¹⁶⁵² **ToT** time-over-threshold
- ¹⁶⁵³ **TPC** Time Projection Chamber
- ¹⁶⁵⁴ **TPX3** Timepix3
- ¹⁶⁵⁵ **μ -PIC** Micro-Pixel Gas Chamber
- ¹⁶⁵⁶ **μ -RWELL** Micro-RWELL